昭和52年度サンシャイン計画委託研究成果報告書

「太陽光発電システムの研究開発
（粒子非加速成長形シリコン薄膜結晶の研究開発）」

昭和53年3月

株式會社 日立製作所

昭和52年度サンシャイン計画委託研究成果報告書

「太陽光発電システムの研究開発(粒子非加速成長形シリコン薄膜結晶の研究開発)」

昭和53年3月

株式会社　日　立　製　作　所

「太陽光発電システムの研究開発（粒子非加速成長形シリコン薄膜結晶の研究開発」

株式会社日立製作所中央研究所

昭和５３年３月　７３　頁

現在の技術で太陽光発電システムを構成した場合に比し，価格が実質で百分の一以下となる太陽光発電システムの製造を可能とする技術を開発する目途をつけることを目標にして，粒子非加速成長形シリコン薄膜結晶の製造技術の確立を図り，あわせてそれを用いた太陽光発電システムを研究開発することを目的とした。

委　託　研　究　成　果　報　告　書

昭和５３年５月３０日

工業技術院長

窪　田　雅　男　殿

東京都千代田区丸の内一丁目５番１号

株式会社　日　立　製　作　所

取締役社長　　吉　山　博　吉

昭和５２年４月１８日付け研究開発委託契約

研究項目「太陽光発電システムの研究開発（粒子非加速成長形シリコン薄膜結晶の研究開発）」

上記委託研究の成果について，研究開発委託契約条項第２３条第１項の規定により，下記のとおり提出します。

記

委託研究成果説明書

目　　次

I 概　　要

1. 研究実施責任者氏名

株式会社　日立製作所　中央研究所　第三部主管研究員　徳　山　　巍

2. 研究項目と実施状況，研究担当者氏名

項目＼年月	52／4 4/18	5	6	7	8	9	10	11	12	53／1	2	3	研究担当者
薄膜結晶の研究													徳山　巍 斎藤　忠 蕨迫光紀
セル構成法の研究													徳山　巍 斎藤　忠 蕨迫光紀

3. 研究内容と成果の概要

3.1 研究内容

3.1.1 薄膜結晶の研究

前年度までの研究開発で得られたアルミナ板，グラファイト板及び低価格シリコン多結晶板などの基板上への薄膜結晶形成技術を比較検討した結果，特に低価格の金属級シリコン(Metallurgical — Grade Silicon) を原料として作製した多結晶シリコン板が基板として最も優れているとの結論に達した。

本年度の研究開発においては，チョクラルスキー法で金属級シリコン及び精製した金属級シリコン原料から製作した多結晶インゴット中の不純物及び結晶欠陥の量と種類，その電気的性質についてまず検討した。次に，この基板上にジクロルシランをソースとする気相成長法によりシリコン薄膜を形成し，形成した薄膜中の結晶欠陥及び少数キャリヤのライフタイムを調べ薄膜結晶の評価を行った。

3.1.2 セル構成法の研究

セル構成法については，前年度までは直列抵抗の小さい電極形成技術を進め，半田電極の有用性を指摘した。本年度は半田ディップ法の効果を基礎的に検討した。また，光電変換効率の低い原因を基礎的に検討するため，前年度開発したコンピュータシミュレーション法を用い，太陽電池特性に影響するパラメータを計算した。更に，光電流の不均一性をレーザ走査顕微鏡などで調べ，光電流値に対する基板結晶中の二次的不純物と結晶欠陥の影響を検討した。

3.2　成果の概要

3.2.1　薄膜結晶の研究

(1)　シリコン基板の作製と評価

金属級シリコン及び精製処理をした金属級シリコンを原料として，チョクラルスキー法により多結晶インゴットを作製し，結晶成長条件の検討と質量分析法によるインゴット中の不純物分析を行った。いずれの場合にも原料に比しインゴット中の不純物を減少させうることがわかり，かつ原料による差，成長条件による差を確認した。インゴットの結晶性を化学エッチ法で調べ，各種欠陥の確認，欠陥部分に不純物の偏在すること，その結晶成長条件による変化を確認した。

作製された結晶の電気的特性は比抵抗p形0.05～0.09Ω・cm，正孔移動度50～100cm^2/V・s，正孔濃度0.7～1.6×10^{18} cm^{-3}の値を示し，原料による若干の差が認められた。一方，チョクラルスキー法により引上げた（結晶した）多結晶を溶解して再度引上げた結晶は，ほとんど単結晶に近い構造を示し，不純物の偏在も存在しないことがわかった。

(2)　p形活性層の評価

ジクロールシラン（SiH_2Cl_2）により，上記多結晶基板上に形成したp形活性層（厚さ30～40μm）の結晶性を化学エッチ法で調べ，また，この層の少数キャリヤのライフタイムを測定した。ライフタイムは原料の純度に関係し，0.35（低純度）～0.52（高純度）μs（平均値）を示し，また同一基板でも結晶粒界上に形成されている活性層部分では0.15μs 程度と極端に小さく，粒界部分での不純物の偏析の起っている可能性を示している。

3.2.2　セル構成法の研究

(1)　セル構成技術の改善

直列抵抗の低下を半田電極により方法を開発し，大面積セルの効率低下を防ぐことができた。計算による推定値と実測値のずれは約2倍で，多結晶セルでの表面の凹凸の存在が効果を示すこともわかった。

(2)　セル特性の評価

今年度は，変換効率向上の目的で，p形活性層中での不純濃度を基板側で多く，表面側で少くして傾斜をもたせる方法を開発した。その結果，不純物濃度を一定とした従来構造に比し，変換効率は数％向上した。

また，基板による差も明確に得られ，変換効率は用いた基板により下記の値をうることができた。

(a)　金属級シリコンを直接結晶化した基板を用いた場合
：5.4％

(b)　上記結晶を用い，再度溶融結晶化した基板を用いた場合
：7.8％

(c)　精製した金属級シリコンを直接結晶化した基板を用いた場合
：7.0％

(d)　上記結晶を用い，再度溶融結晶化した基板を用いた場合
：8.6％

試作したセルの短絡電流値は上記(b)と(c)の間では大差なくp形活性層中に含まれる有害不純物の量はあまり変っていない。(b)と(c)の差は曲線因子の向上にあり，(b)の基板は単結晶に近い構造であることから結晶性の差に基づくものと思われる。(d)の基板は，前3者に比べ不純物と欠陥の点で最も優れており，効

率もこれまでの最高値が得られた。効率の変動幅は，試作個数２２個で，7.5～8.6％で，平均値は8.0％であった。

しかしながら，同一基板を用いｐ形活性層を作らずに直接基板内に拡散法で接合を形成したセルでは，短絡電流値が低く，曲線因子も小さい。上記(a)の基板では変換効率１％以下，上記(d)の基板でも最高４％であった。

(3) 光電変換特性の解析

計算機シミュレーション法により直列抵抗，並列抵抗，ダイオードの飽和電流値，順方向電流の傾斜係数等の等価回路パラメータを各種のセルについて求め比較した。単結晶セルに比し多結晶セルの特性上の大きな差は飽和電流の二成分（傾斜係数が１の成分と２の成分）間の大きさの関係が逆になっていることがわかり，このため多結晶セルでの開放電圧が低い値を示している。また，多結晶セルでは，並列抵抗は単結晶セルの約$\frac{1}{10}$と低いが，光電流そのものはほぼ同じ大きさであることもわかった。

(4) 光起電力分布の測定

レーザ光走査法でセルの粒界部分での光起電力分布を調べると，前年度に測定した高純度多結晶を基板とした場合に比し，欠陥部分での光電流の低下幅が大きく，１，２項に述べた小数キャリヤのライフタイムがこの部分で低下することと合致する。このことは多結晶基板の粒界に多くの有害不純物が偏在し，これがｐ形活性層形成時に活性層中に含まれることを示している。

(5) 得られた変換効率値の要約

薄膜太陽電池のプロセス条件を最適化した結果，次表に示す変換効率を得た。

金属級シリコンから作製した結晶を基板としたときの薄膜太陽電池の特性

シリコン基板	p形層のキャリヤ濃度 (cm^{-3})	変換効率* (%)	セル面積 (cm^2)
金属級シリコンから直接結晶化	2×10^{16}	5.03	5.29
	$10^{18}\rightarrow10^{16}$**	5.42	10.2
上記結晶を用い，再度溶融結晶化	3×10^{17}	7.61	10.0
	$10^{18}\rightarrow10^{16}$ **	7.77	19.7
精製した金属級シリコンから直接結晶化	3×10^{16}	6.11	11.4
	$10^{18}\rightarrow10^{16}$ **	6.97	12.6
上記結晶を用い，再度溶融結晶化	$10^{18}\rightarrow10^{16}$ **	8.59	20.8

* AM1（100 mW/cm^2）の擬似太陽光下で測定。反射防止膜付。

** p形活性層中に基板側から濃度勾配を形成。

変換効率はp形活性層の正孔濃度のグレーディングにより向上し，特に精製した金属級シリコンから結晶作製を再度行った場合，単結晶に近いものが得られ，その効率は8%以上となった。上記表に示したように再度結晶を作製した場合，本年度の目標であった面積10～20 cm^2，変換効率7～8%の目標を達成した。平均効率8%のセルを用い，次図のごときソーラモジュールを試作した。このテストモジュールは面積約20 cm^2のセル8個から成り，太陽光下で約1Wの直流出力が得られることを確認した。

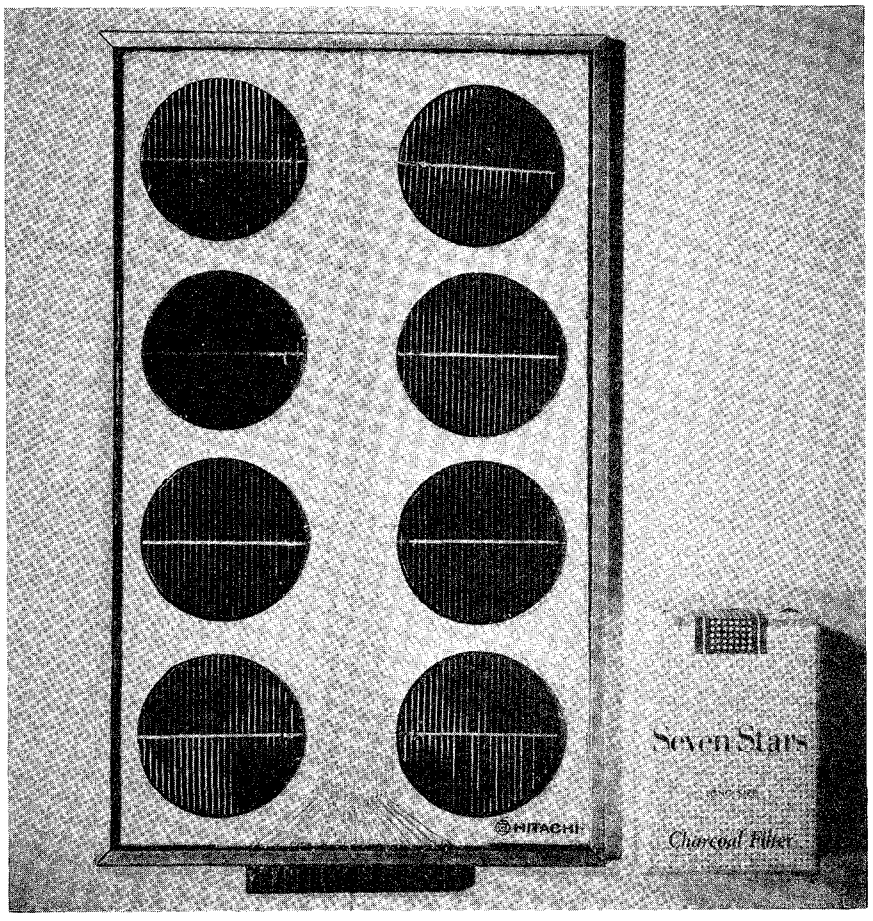

試作した１Ｗテストモジュールの外観

4. 研究発表，講演，文献，特許等の状況

4.1 研究発表状況

研究発表状況は下記のとおりである。

番号	題名	発表先	発表時期	発表者
1	Growth and Structure of Polycrystalline Indium Phosphide Layers on Molybdenum Sheets	The Electrochemical Society	昭和51年3月	中央研究所第三部 斎藤　忠 松原　直 皆川重量
2	Dendritic Growth of Silicon Thin Films on Alumina Ceramic and Their Application to Solar Cells	The Japan Society of Applied Physics	昭和52年3月	中央研究所第三部 斎藤　忠 蕨迫光紀 伊藤晴夫 中村信夫 田村　博 皆川重量 徳山巍
3	Polycrystalline Indium Phosphide Solar Cells on Molybdenum Substrates	The Japan Society of Applied Physics	昭和52年5月	中央研究所第三部 斎藤　忠 松原　直 皆川重量
4	Fabrication and Characterization of Thin Film Silicon Solar Cells on Alumina Ceramic	The Institute of Electrical and Electronics Engineers, Inc.	昭和52年4月	中央研究所第三部 蕨迫光紀 斎藤　忠
5	Fabrication and Characterization of Solar Cells Using Dendritic Silicon Films Grown on Alumina Ceramic	The Institute of Electrical and Electronics Engineers, Inc.	昭和52年3月	中央研究所第三部 皆川重量 斎藤　忠 蕨迫光紀 中村信夫 伊藤晴夫 徳山巍
6	Problems in Photoresponse Distribution Measurement	The Institute of Electronics Engineers, Inc.	昭和52年3月	中央研究所第三部 皆川重量 蕨迫光紀
7	Electrical Properties of n-type Polycrystalline Indium Phosphide Films	The Electrochemical Society, Inc.	昭和52年7月	中央研究所第三部 斎藤　忠 松原　直
8	Initial Growth Behavior of Indium Phosphide on Molybdenum Substrates	Elsevier Sequoia S.A. (Thin Solid Films)	昭和53年3月	中央研究所第三部 斎藤　忠 松原　直 皆川重量
9	Polycrystalline Solar Cells on Metallurgical Silicon Substrates	The Japan Society of Applied Physics	昭和53年3月	中央研究所第三部 蕨迫光紀 斎藤　忠 伊藤晴夫 中村信夫 徳山巍

4.2 講演状況

講演状況は下記のとおりである。

番号	題名	講演先	講演時期	講演者
1	グラファイト基板上に作成した多結晶Si薄膜太陽電池	昭和52年度電子通信学会半導体部門全国大会	昭和52年8月	中央研究所第三部 伊藤晴夫 斎藤忠 蕨迫光紀 中村信夫 徳山巍
2	Polycrystalline Solar Cells on Metallurgical Grade Silicon Substrates	第9回固体素子コンファレンス	昭和52年8月	中央研究所第三部 蕨迫光紀 斎藤忠 伊藤晴夫 中村信夫 徳山巍
3	Polycrystalline Solar Cells Fabricated on Metallurgical Silicon Substrates	1977 Photovoltaic Solar Energy Conference	昭和52年9月	中央研究所第三部 蕨迫光紀 斎藤忠 中村信夫 伊藤晴夫 徳山巍
4	多結晶Si薄膜太陽電池(X) EBIC像の観察	第38回応用物理学会学術講演会	昭和52年10月	中央研究所第三部 蕨迫光紀 斎藤忠 伊藤晴夫 中村信夫 徳山巍
5	多結晶Si薄膜太陽電池(XI) 多結晶セルの光電流分布	同上	同上	中央研究所第三部 斎藤忠 蕨迫光紀 伊藤晴夫 中村信夫 徳山巍
6	多結晶Si薄膜太陽電池(XII) 金属Siからの結晶引上げとその評価	第25回応用物理学関係連合講演会	昭和53年3月	中央研究所第三部 斎藤忠 黒田慧慶 松原直 伊藤晴夫 徳山巍
7	多結晶Si薄膜太陽電池(XIII) 金属Si基板多結晶薄膜太陽電池	同上	同上	中央研究所第三部 中村信夫 蕨迫光紀 斎藤忠 松原直 伊藤晴夫 徳山巍

4.3　文献状況

なし

4.4　特許出願状況

特許出願状況は下記のとおりである。

番号	発明の名称	出願日	出願番号	発明者所属 氏名
1	太陽電池の構造	昭和52年7月 15日	特願昭52- 84077	中央研究所 第三部 蕨迫光紀 斎藤忠 伊藤晴夫 中村信夫
2	半導体装置の電極	昭和52年7月 15日	特願昭52- 84078	中央研究所 第三部 斎藤忠 中村信夫 千葉幸子 伊藤晴夫 蕨迫光紀 徳山巍

4.5　その他

なし

5.　他の研究機関における類似研究及び協力関係状況

なし

6.　その他

なし

Ⅱ　研　究　内　容

1.　薄膜結晶の研究

1.1　概　要

前年度までの研究開発においては，アルミナ及びグラファイト板上に気相化学反法によって多結晶シリコン膜を被着し，その形成膜を更に帯域溶融を行った基板，低純度シリコンを原料として，ＣＺ法（チョクラルスキー法）で引上げ結晶化した多結晶基板等の上に薄膜シリコンをエピタキシャル成長し，セルを作製して検討を加えた。その結果，これら基板の影響並びにエピタキシャル層の構造の光電変換特性に対する結晶粒界や不純物の影響等についての知見をうることができた。

昭和５２年度は，この結果を基に，太陽電池の製造価格低下の観点から，低価格の金属級シリコンを原料として選び，ＣＺ法で棒状結晶を引上げ，切断加工したものを基板とし，その上に薄膜シリコンを気相化学成長させてセル構造とする研究を主体に研究開発を行った。

1.2　シリコン基板の作製と評価

1.2.1　ＣＺ法と結晶中の不純物

市販の金属級シリコン及び精製した金属級シリコンを原料として，単結晶引上げ装置を用い，結晶成長を行った。セル構成用の基板は，これを 0.5 ㎜の厚さにスライシングして製作した。金属シリコンを原料とする場合，市販の数㎝径の塊状の材料をそのまま使用して棒状インゴットに形成したもの（ＭＥ）のほか，同様にして得た結晶を原料とし，これに硼素を添加して再度溶解し結晶化したもの（ＭＦ）の２種類について検討した。

また，精製金属シリコンを原料とした場合も同様に，ＣＺ法で一度結晶化したもの（ＭＳＣ）と，これを原料にして再度溶解し結晶化したもの（ＭＳＤ)の２種類を検討した。その結果，原料の種類によらず粗原料から直接溶解結晶化した結晶（ＭＥ，ＭＳＣ）は多結晶構造をなしており，再度引上げた結晶（ＭＦ，ＭＳＤ）はほぼ単結晶化することがわかった。粗原料から直接製作した結晶が単結晶化しない理由は，粗原料中に含まれる多量の不純物がシリコン融液上にスラグとして浮遊し，結晶表面に付着すること，及びカーボン等のシリコン融液に融けない不純物の混入による結晶核の発生によるものと思われる。

表1.1　金属級シリコンから作製した結晶の質量分析計による不純物分析

（ppma）

不純物種	原　料	引上げ速度（㎜／㎜）			
		ＭＥ*		ＭＦ**	
		0.40	2.0	0.5	2.0
B	18	8	8	800	800
Aℓ	3,800	20	300	20	600
P	24	−	6	7	20
As	−	0.02	0.07	0.1	0.2
Cu	34	3	90	0.3	300
Ni	130	−	50	−	2,000
Fe	3,200	0.3	3,000	3	10,000
Mn	42	0.02	200	0.05	200
Cr	92	0.02	20	0.05	20
Mg	−	0.02	10	0.01	100
Ti	110	−	200	0.02	300
V	1	0.02	600	−	70
Zr	0.1	−	3	−	10

＊　金属級シリコンから直接作製した結晶。

＊＊　ＭＥ結晶をソースとして再度引上げ結晶化したもの。Ｂドープ。

表1.2　精製金属級シリコンから作製した結晶の
質量分析計による不純物分析　　（ppma）

不純物種	原　料	引上げ結晶	
		MSC*	MSD**
B	26	8	8
Aℓ	100	2	0.06
P	27	6	6
As	0.3	0.07	0.02
Cu	13	0.3	0.3
Ni	−	−	−
Fe	500	0.3	0.3
Mn	30	−	−
Cr	4	0.02	−
Mg	0.8	0.01	−
Ti	40	−	0.02
V	110	0.02	−
Zr	0.2	−	−

＊　精製金属級シリコンから作製した結晶。引上げ速度：1㎜／㎜。

＊＊　MSC結晶をソースとして再度溶融結晶化したもの。

原料及び作製した結晶中の不純物量を固体質量分析計で測定した結果を表1.1，表1.2に示す。原料として用いた金属級シリコンと，精製した金属シリコン中には共にAℓとFeが特に多く，そのほかCu，Cr，Mn，V，Ti，C等を数＋ppm～数百ppm含んでいるが，これを溶融してCZ法で結晶を作製することにより，それぞれの不純物は偏析効果のため数分の一から数千分の一に減少している。しかし，不純物分析結果より求めた実効偏析係数の値は，B，Aℓを除いては，報告されている平衡偏析係数の値よりも2桁程度大きな値であり，偏析効果が十分とは言えない。特に

引上げ速度が速い場合には，部分的な不純物の異状偏析も見られ（後述），スラグ浮遊等の問題も含めて，今後引上げ条件の検討が必要である。

1.2.2　結晶欠陥

金属級シリコンから直接形成した結晶は通常多結晶となり，引上げ速度を変えると多結晶の結晶粒径や結晶中の偏析（夾雑物）の形状などが異なり，従来の高純度単結晶インゴットには見られない様々な結晶欠陥を含んでいる。

図1.1は引上げ速度を比較的遅くしたとき得られた多結晶(ME)中の欠陥を，化学エッチ法で調べた結果である。図中の不規則な

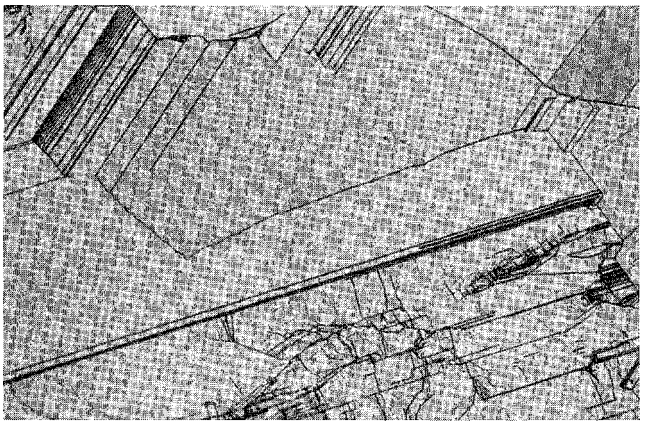

(a)

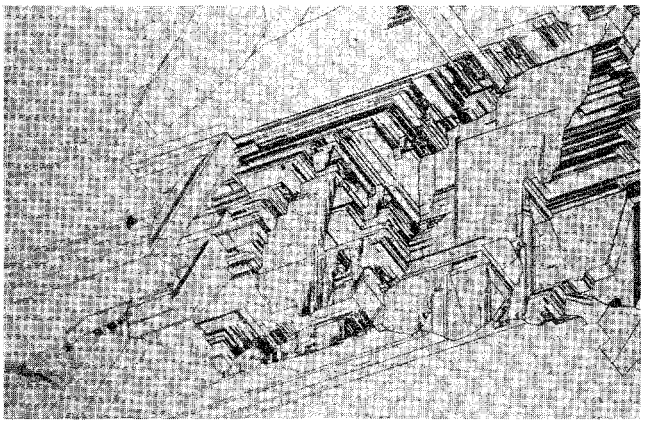

(b)

200μm

図1.1　金属級シリコンから作製した結晶表面の化学エッチ像

線は結晶粒界で，ほぼ結晶粒界の端から端まで伸びている直線は，小傾角境界又は双晶境界であると推測される。図 1.1 (a)の下部には多数のエッチピットが存在しており，エッチピットは大別してピット列を形成しているものと独立しているものの２種類に分類される。

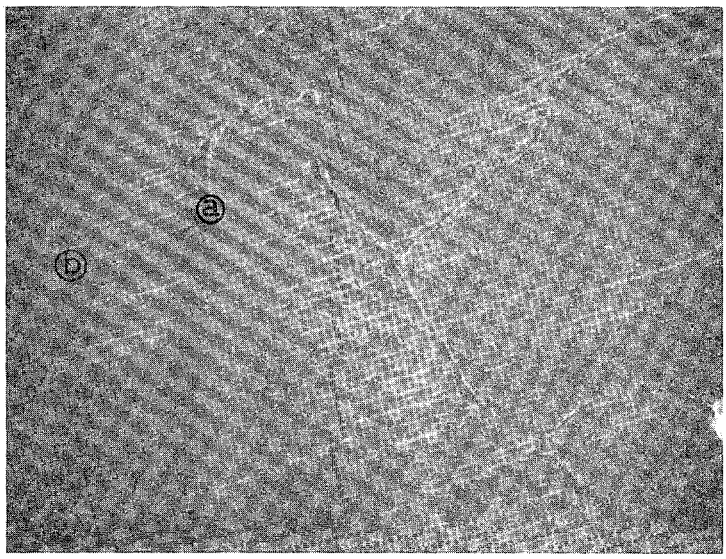

(a)

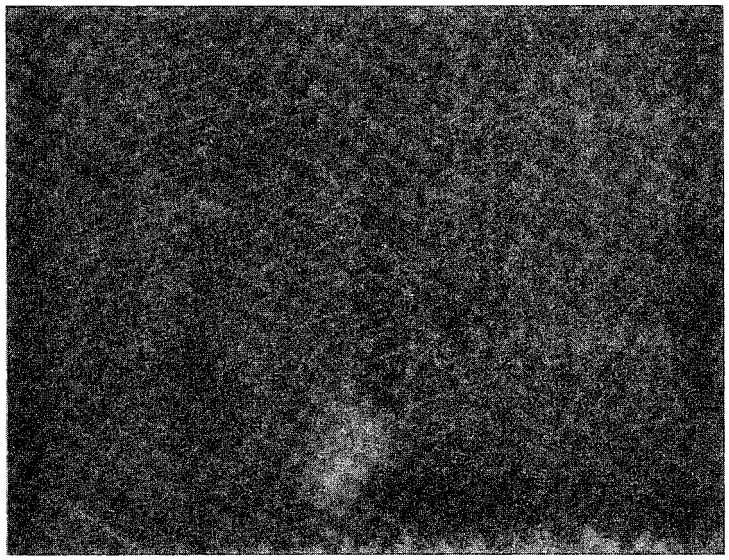

(b)　　0.2 mm

図 1.2　早い引上げ速度で作製した結晶中の異常偏析
引上げ速度：1.2 mm／min（ME）
(a)　走査電子顕微鏡像
(b)　Aℓ　Kα 線像

引上げ速度を早くしたり，多量の不純物を含むＳｉ融液から結晶を引上げた場合（ＭＥ），結晶中に数百μm程度までの大きさの熊手状の偏析が見られた。図1.2(Z)はシントロン研摩機で鏡面研摩したＳｉ試料表面の走査電子顕微鏡像である。この偏析不純物の同定を行うため，Ｘ線マイクロアナライザを用いてその構成元素を調べた。図1.2(b)は$A\ell$ Kα線の面内分布であるが，(a)の偏析パターンと完全に一致しており，偏析物の主元素は$A\ell$であることがわかる。この偏析物について，更に詳細に検討するため非分散Ｘ線エネルギー分析を行って，元素の相対存在量を調べた。図1.3はその分析結果で，図1.2のⓐとⓑの場所について調べた。ⓐ部は少量のＳｉを含む$A\ell$が主であるが，そのほかに比較的多量のＣｒ及びＦｅを含んでいることがわかる。またⓑ部では，Ｓｉの含有が多い$A\ell$合金で，ＣｒとＦｅも非常に少くなっている。この$A\ell$-Ｓｉ合金の偏析は，結晶成長中の組成過冷却で生じたと考えられ，引上げ速度を遅くするに従って減少してゆき，0.1mm/minの引上げ速度では全く見られなかった。

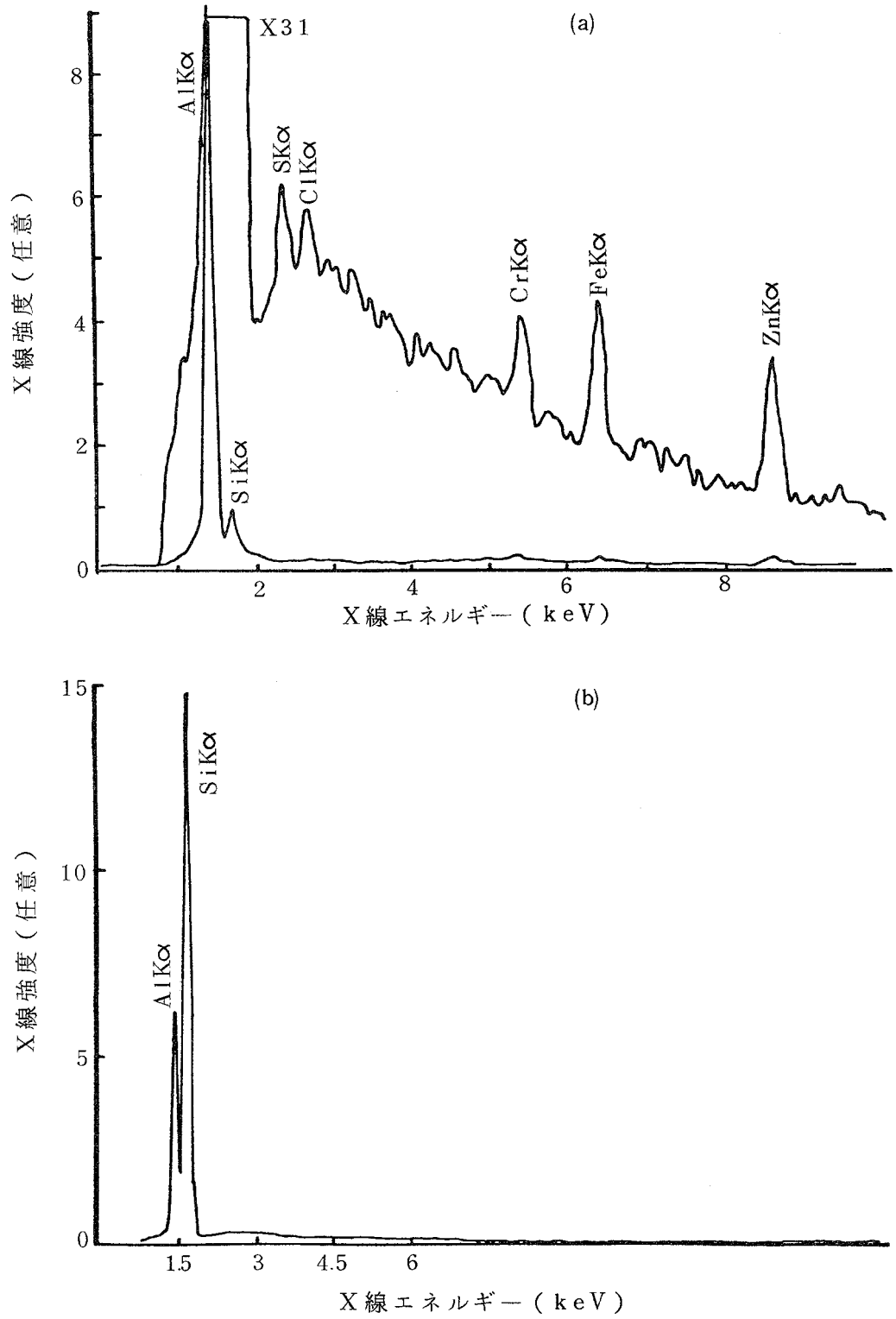

図 1.3　速い引上げ速度での異状偏析物の非分散エネルギー分析（ＭＥ，引上げ速度 1.2 ㎜／min ）

(a)　図 1.2 の(a)図中のⓐの部分

(b)　図 1.2 の(a)図中のⓑの部分

図 1.4 は，再度CZ法により結晶化を行い，単結晶化した結晶(MF)の表面を鏡面研摩した後に化学エッチングを行ったもので，同心円状の欠陥が現われている。四探針法による抵抗分布と対比させると，白く見える部分の抵抗は黒い部分より２０～３０％高い値を示す。これは，結晶成長時の温度の不均一性により不純物が偏析したためと推測される。

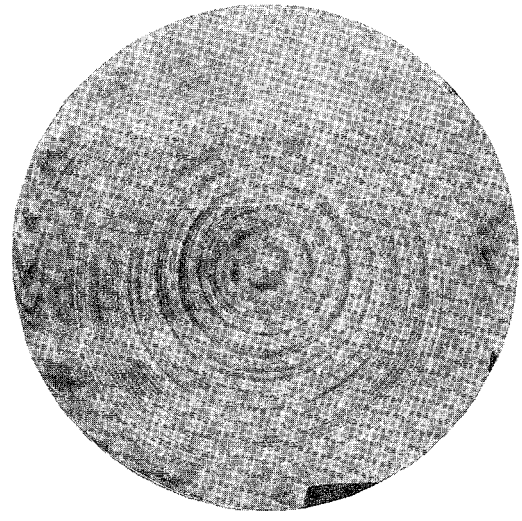

図 1.4　化学エッチングした結晶表面（ＭＦ）

1.2.3　結晶の電気的性質

Van der Pauw 法により，それぞれの試料の電気的性質を測定した結果を表 1.3 に示す。作製した結晶はすべてｐ形を示し，ほう素を添加した結晶以外のキャリヤ濃度は $1\times10^{18}\,cm^{-3}$ で，Ｂと Aℓがアクセプタを形成していることがわかる。各結晶のキャリヤ濃度に対応する比抵抗値をＩｒｖｉｎ の表より求め，実測値と比較すると，いずれも実測値の方が 50～100％高い値を示しており，粒界抵抗や深い準位をもつ不純物の影響であろうと考えられる。このため，移動度の値も高純度単結晶に比べて小さくなっている。

表 1.3　CZ 法で作製した結晶の電気的性質

結晶の種類	ME	MF *	MSC	MSD
引上げ速度（mm／min）	0.1～1.2	0.1～1.0	1.0	0.5～1.0
比　抵　抗（Ω・cm）	0.079～0.083	0.001	0.037～0.038	0.023～0.028
移　動　度（cm^2／V・s）	56～97	31～35	93～98	55～70
正孔濃度（cm^{-3}）	0.8～1.4×10^{18}	1.2～2.0×10^{20}	1.5～1.8×10^{18}	3.9～4.8×10^{18}

＊ほう素をドープした結晶。

引上げ速度の影響は，引上げ速度が遅くなるほど正孔濃度が減少する傾向を示す。これは Aℓ の偏析係数が小さいため，Aℓの含有量が減少するためで，不純物分析結果と一致している。また，実測した比抵抗値は，場所によるばらつきがあるが，正孔濃度の変化に必らずしも対応せず，深い準位を形成した不純物の影響が大きいためと推察される。

図 1.5 は金属級シリコン原料から作製した結晶表面（ME）の四探針法による比抵抗分布を調べたもので，0.106～0.275Ω／口，平均値は 0.169Ω／口，標準偏差は 13.4％ である。比抵抗値は結晶中心部が低く，周辺部が高い傾向が見られ，結晶粒ごとの変動は少い。一般に CZ 法による結晶成長では固液界面が上方に凸の形状をしているため，同一平面内で見ると周辺部は中心部より時間的に先に成長したことになり，不純物は成長と共に融液内に濃縮されるので，時間的に先に成長した結晶のキャリヤ濃度は小さく，したがって結晶周辺の比抵抗が中心部より高くなると考えられている。

しかし，図 1.5 に示す金属級シリコンから引上げた結晶中には，異状に抵抗の高い部分が周辺部にドット状に分布している。この

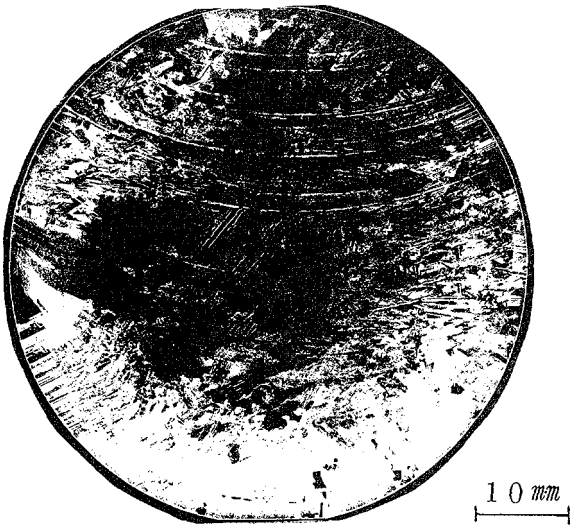

(a)　鏡面エッチ面

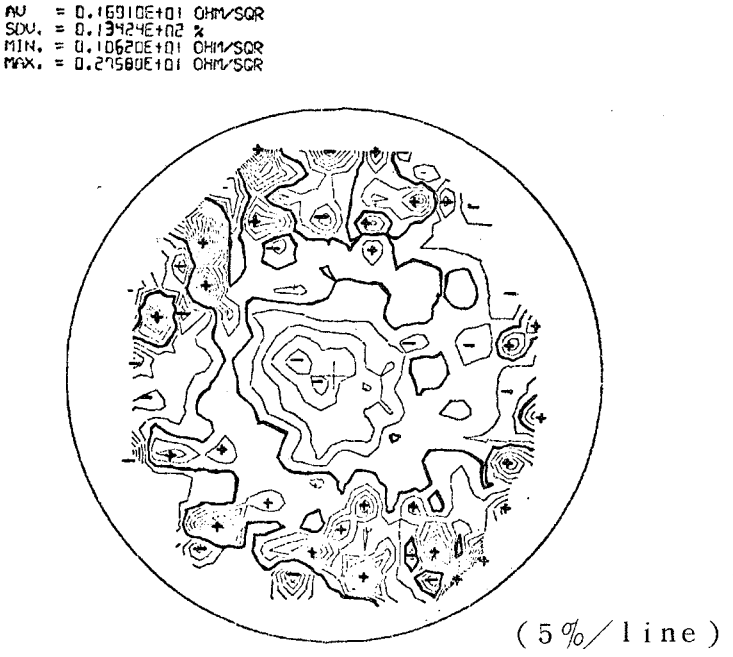

(b)　シート抵抗分布

図 1.5　四探針法測定による結晶（ME）の比抵抗分布

(a)　(b)に対応する表面写真

(b)　比抵抗分布

抵抗の高い部分を赤外顕微鏡で観察すると，結晶中心部に比べて赤外透過率が悪く，結晶が歪んで見え，結晶性が悪いことがわかった。このために深い準位を形成する不純物をより含み易く，キャリヤをトラップするために抵抗が高くなっているものと考えられる。

1.3　エピタキシャル成長層の評価

金属級シリコンと精製した金属級シリコンを原料として，CZ法で引上げた結晶を0.5㎜の厚さにスライスしたのち，化学エッチングしてセル作製の基板とした。この基板上にジクロルシラン（$SiH_2C\ell_2$）を用い，1100℃の温度で30～40μmのp形Si層，1000℃の温度で約0.5μmのn形Si層をエピタキシャル成長させた。この成長層の評価を行った。

図1.6は，基板（ME）に存在する結晶欠陥が成長層にどの様な影響を与えるかを見るために，試料断面の化学エッチングを行ったものである。基板には非常に多くの結晶欠陥の存在が見られる。

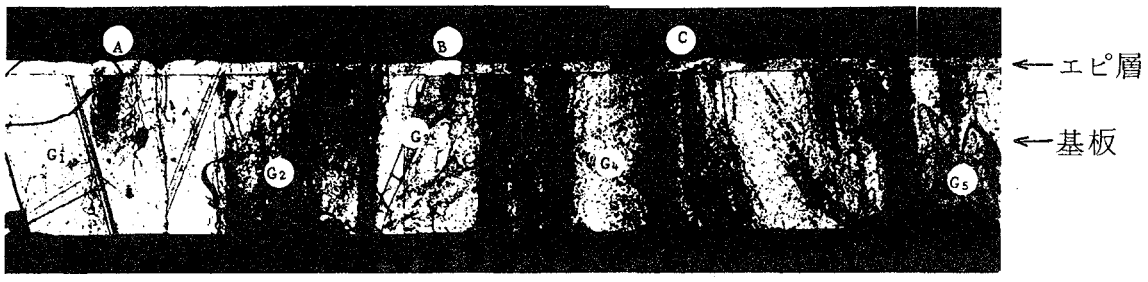

図1.6　結晶基板（ME）上の成長層の断面（化学エッチ）
引上げ速度：1.2㎜／min
エピ層作成条件：1100℃，ジクロルシランソース
厚さ：37μm

図中G_1～G_5で示したのは結晶粒内に局所的にエッチピットが存在している。また，図中の結晶粒G_1，G_2及びG_4の一部に黒い穴が存在しているが，研磨後は見られずエッチ後に見られることから$A\ell$-Si合金層が存在していたと思われる。G_5の結晶粒は結晶内部で成長が止まったか始まったかのいずれかであるが，特にその先

端に異常な析出が存在している様子は見られない。

図中，Ⓐで示した領域は基板内部の不規則なエッチピット列が1部成長層まで続いている例で，Ⓑは結晶粒G_3の近傍でピットの少い領域，Ⓒは基板内部の欠陥が成長層中にほとんど伝播されない例である。

Ⓐ，Ⓑ，Ⓒの拡大写真を各々図1.7(a)，(b)，(c)に示す。図1.7(a)の中心部と右側では基板内部のエッチピット列が成長層まで続いている。ピット列のピットは浅く灰色のコントラストを有している。成長層にはこの浅いピットのほかに，四角形の深いピットが特に左半分に多量に存在している。このように成長層には二種類のエッチピットが存在しており，(b)及び(c)でも二種類のピットの存在が見られる。(b)は比較的ピット密度の少い領域で，結晶粒とキャリヤ濃度により全体のコントラストが異なる点とピットの形状と密度が異なることが明瞭に示されている。特に，右側の基板中のピットの形状は正三角形に近く，結晶面が{１１１}面に近いことを予測させるが，成長層のピットは三角形ではない。図(c)の左は(b)の延長で基板中のピットの形状は三角形であるが成長層のピットは四角形に近い。(c)の中心部から，三角形のピットの方向が逆転し，右下端部でまた逆転しもとに戻っている。この基板から成長層へ伸びる２本の線の方向は三角形ピットの底辺なので，＜１１０＞方向であるとすると，この２本の線は結晶のスリップラインを意味していると考えられる。

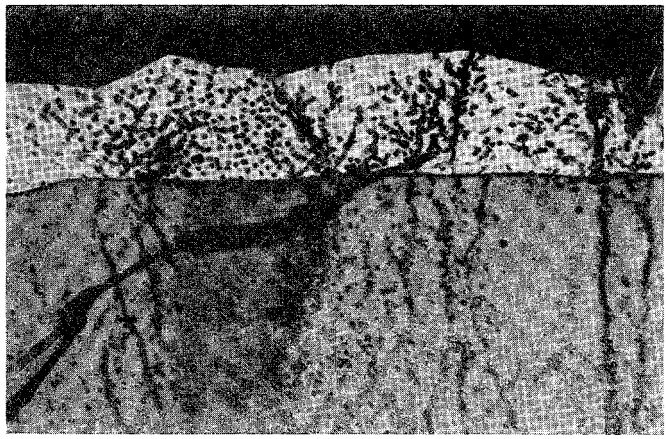

(a)

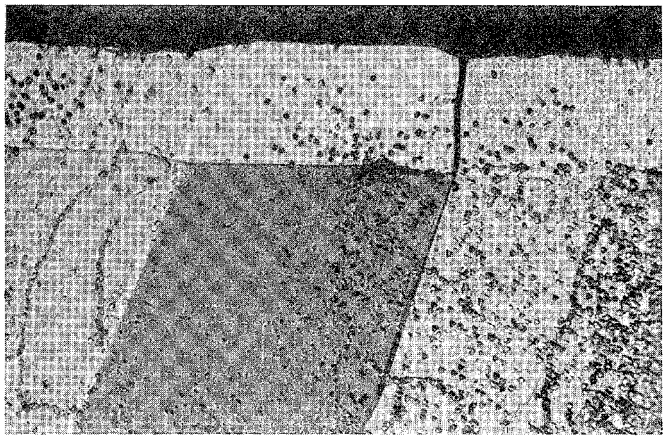

(b)

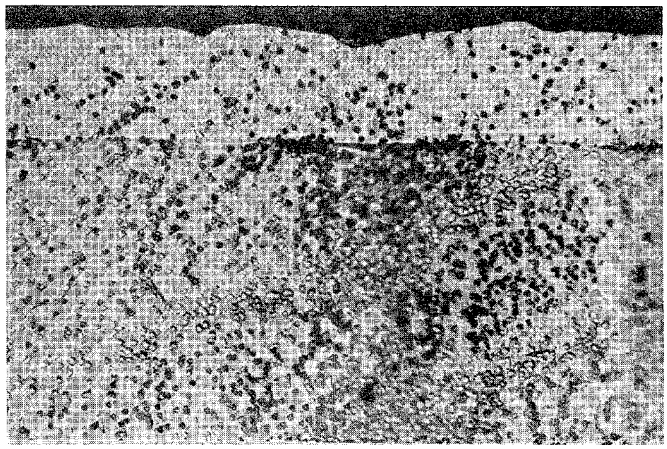

(c)

50 μm

図 1.7　エピタキシャル層断面の化学エッチ像

次に，成長層表面の種々の欠陥を化学エッチングを行って調べた。図1.8は，MEの基板上に成長したSi表面のエッチ像である。図1.8,(a)では黒い点に見える三角形のエッチピットと長さ約5μmの線状欠陥（灰色のコントラスト）の存在が見られる。(b)では三角形のエッチピットが列状に並んでいる。ピット列の多くは，図中Ⓢで示した三角形の底辺に対し垂直であることから，＜２１１＞方向に並んでいると言える。この方向に並ぶ線状欠陥（lineages）は熱歪により生じた小傾角境界と考えられており，この場合も基板自体の熱歪又は基板と成長層との歪などが関与していると考えられる。Ⓢで示した三角形又は線状欠陥はエピ層に典型的に見られる積層欠陥であり，図(c)では積層欠陥が粒界で止まり他の結晶粒には伸びていない様子がわかる。

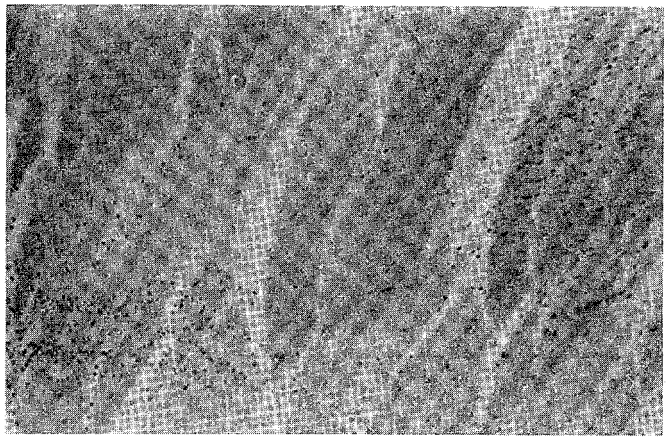

(a)

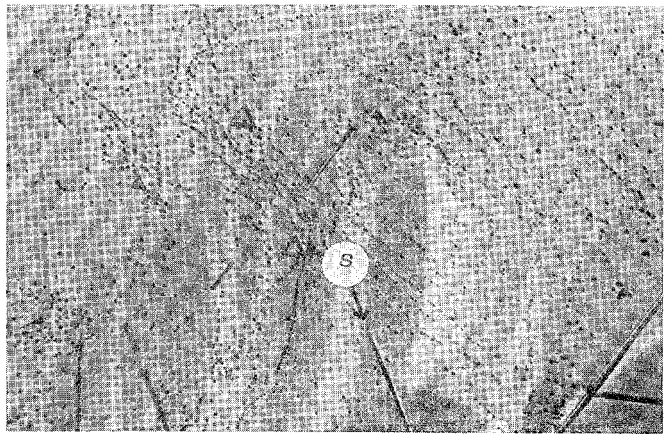

(b)

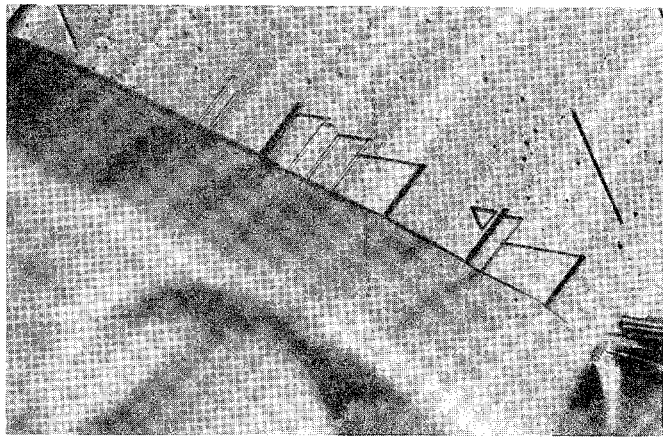

(c)

50 μm

図 1.8　エピタキシャル層表面の化学エッチ像

1.4　問題点

金属級シリコンを原料としてＣＺ法で結晶インゴットを形成し，これを基板として，その上に薄膜シリコンを気相成長してセルを作製する場合，問題点は原料中に含まれる不純物の種類と量に関するものである。インゴットを形成する際には，特に原料の純度が低いために，通常の高純度単結晶インゴット形成の場合と異なる問題点として次のものがある。

(1)　Ｓｉ融液表面にスラグが浮遊し，引上げ中の結晶表面に付着して結晶性を悪化させる

(2)　スラグと石英るつぼが反応し，るつぼの寿命を低下させる

(3)　融解中に多量のガスが発生し，装置を汚染する

などである。

次に，この結晶を基板として，この上に薄膜シリコンを気相成長する場合の問題としては，成長温度が高温であるために，基板から成長層への不純物の固相拡散や気相からのオートドーピングが考えられる。Ｃｕ,Ｎｉ,Ｍｇ は $10^{16}cm^{-3}$ 以上，Ｆｅ,Ｃｒ,Ｍｎは $10^{15}cm^{-3}$ Ｔｉ,Ｖは $10^{16}cm^{-3}$ 以上が活性層中に含まれると，セルの効率が著しく低下することがわかっているが，表1.1，表1.2の不純物分析結果では，Ｆｅ,Ｃｒ,Ｖ(ＭＥ,ＭＦ,ＭＳＣの各結晶)Ｍｎ,Ｔｉ(ＭＥ,ＭＦの各結晶)が基板中に許容量以上含まれている。Ｆｅ 等が大きい拡散係数を持っていることを考えると，成長層中に基板からかなりの量の二次的不純物が拡散していると考えられ，今後金属シリコンの高純度化，結晶引上げ条件の検討，ゲッタリング処理による不純物を減少させる等，基板純度の向上を図る必要がある。

2. セル構成法の研究

2.1 概　　要

1.2で述べたシリコン結晶，すなわち，①市販の金属級シリコンから直接チョクラルスキー法によって作製した結晶，②2回繰返して溶融結晶化した結晶，③精製処理した金属級シリコンから直接作製した結晶，及び④それから2回繰返して溶融結晶化した結晶の4種類の結晶を基板として，ジクロルシランを用いた薄膜形成及び接合形成を行って太陽電池を製作した。本節では，この太陽電池の形成法及び製作した太陽電池の光電変換特性その他の電気的特性の測定及び解析の結果について述べる。

光電変換特性では上記①については変換効率5.7％，②では7.8％，③では7.0％，④では8.6％が得られ，シリコン薄膜形成による太陽電池で実用レベルに近い変換効率をうることができた。また，この結果から，原料の精製，結晶化の際の偏析による基板結晶中の二次的不純物の除去の効果は明らかであり，また薄膜太陽電池の効率向上には薄膜形成用の基板にある水準の純度が必要なことも明らかとなった。

電極構造に関する検討も行い，表面電極については予測値に近い実測値をうることができた。

2.2 セル構成技術

2.2.1 セル構造と製造プロセス

今年度の研究においては，基板として金属級シリコンから作製した円板状ウエーハを用いたので，セル構造は従来形セル構造に類似した形となっている。その構造は一般的には，図2.1に示す

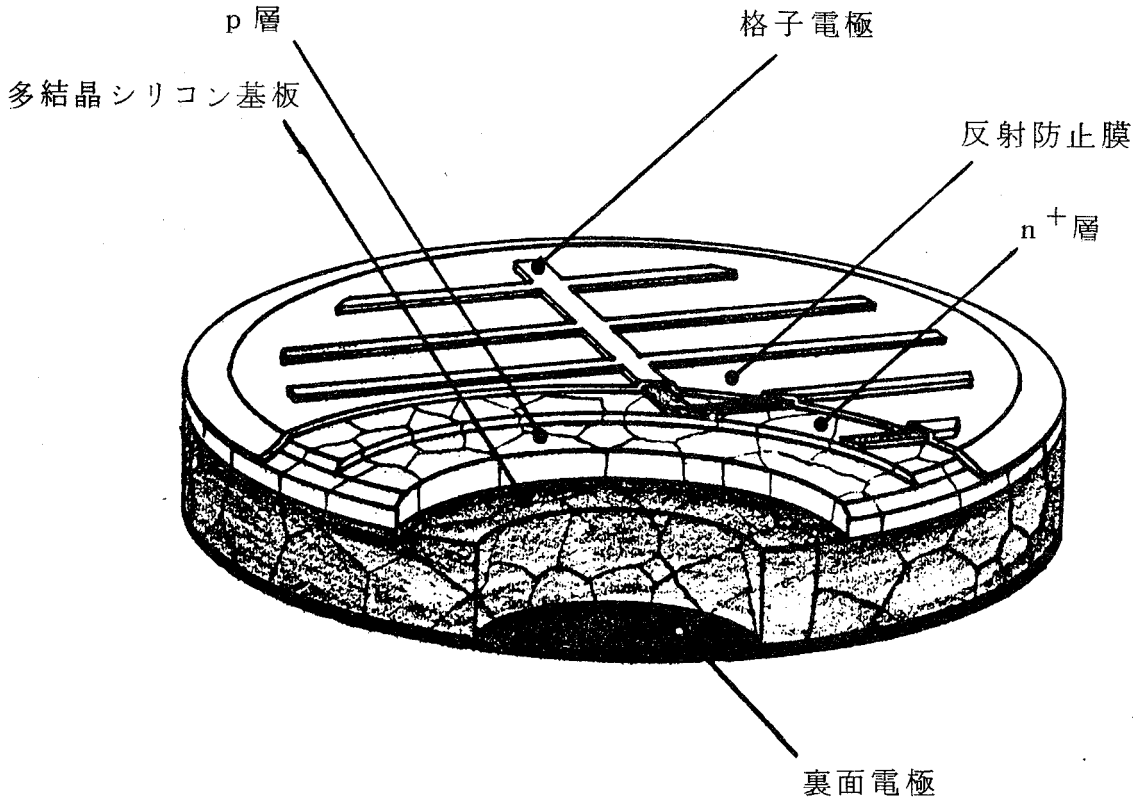

図2.1　多結晶シリコン板上に形成した薄膜太陽電池の構造

ように，厚さ0.4㎜程度の金属級シリコンから形成した基板上にp形の層を30～40μm設け，その上に0.3～0.5μmのn^+形層を設けたものである。基板の直径は作製された結晶の直径により，30～70㎜程度である。n^+形層の上にはチタン／銀（Ti／Ag）の二層金属による格子状コンタクトを設け，その形状は幅150μm，間隔2～4㎜のグリッドと幅1㎜のバスバー（共通端子）より構成される魚骨状である。更にその上からセル全面に反射防止膜を厚さ70～80nm被覆した。セルの裏面にはAℓ－Si合金化処理による全面電極を設けた。なお，電極の半田被覆を行った場合には，表裏おのおのの電極上に厚さ数＋μm

の半田層が付加される。実際に試作したセルの外観写真の一例を図 2.2 に示す。

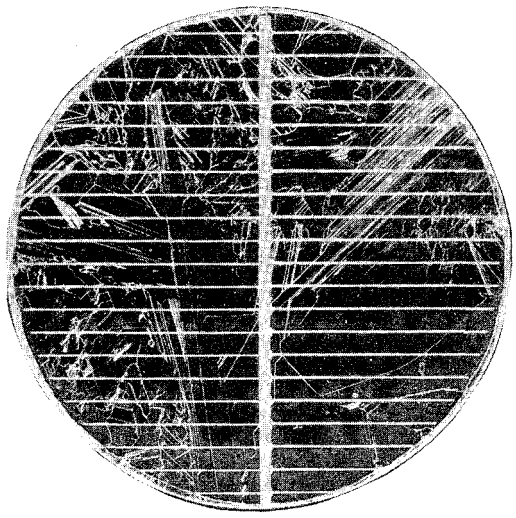

10㎜

図 2.2　シリコン薄膜太陽電池，金属級シリコンから作製した多結晶上に形成したもの

金属級シリコン基板は結晶から切出したのち，切断による加工歪を除去する目的で弗硝酸混液により表面層を数十μmエッチした。

p形層の形成は，高周波加熱の気相成長炉で行い，ソースガスとしてジクロルシラン（SiH_2Cl_2），キャリヤガスとして水素を用い，1000～1100 ℃で行った。代表的な成長速度は 2.5～2.7 μm／㎞である。p形不純物のドーピングは稀釈したジボラン（B_2H_6）を用い，通常成長層中の濃度が10^{16}～$10^{17}cm^{-3}$となる範囲で行ったが，一部については成長層中に内部電界を形成する目的で，基板から表面側に向け10^{18}～$10^{16}cm^{-3}$の濃度勾配を設けた。

n^+ 層の形成はエピタキシャル成長若しくは拡散によった。エピタキシャル成長の場合にはドーピングガスとしてフォスフィン（PH_3）を用い，2～3×$10^{19}cm^{-3}$，シート抵抗値として数十Ω

／口程度となるようにp形層と同様にジクロルシランガスを用い，フォスフィン（PH_3）をドーピング不純物として形成した。また，拡散による場合には拡散ソースとして塩化ホスホリル（$POC\ell_3$）を用い，850～900 °Cとエピタキシャル成長よりは若干低い温度で処理してp層の表面にn形層を形成した。なお，一部のセルについては，基板結晶の評価を含め，直接拡散によるセル形成の可能性を調べるため，p形のエピタキシャル層の形成を行わずに上記の拡散条件により基板の表面に直接接合の形成を行った。

電極の形成はAℓ 蒸着，合金化処理，Ti／Ag 蒸着の順に行い，Ti／Ag については主に電子ビーム蒸着法により金属マスクを通して蒸着し，Aℓ については抵抗加熱法によった。Tiを100nm程度，この上Agを2～3 μm 連続して蒸着した。Aℓ の場合には，1～1.5 μm の厚さとした。なお，Ti／Ag蒸着の場合には250 °Cの加熱を行い，Aℓ 蒸着の場合には常温で行った。Aℓ の合金化処理は蒸着後に650 °C以上の温度で不活性ガス雰囲気中にて10 min 以上の加熱を行った。

電極形成ののち，基板表面の周辺部をエッチングにより除去し，メサ形構造とした。この段階で初めて太陽電池としての動作が観測されるようになる。一部のセルについては半田ディップ法により電極上への半田層形成を行った。使用した半田は Sn-Pb 比60:40に Agを 6 wt %加えたもので，半田浴温度は250 °Cである。

反射防止膜の形成は，一部については SiO膜の真空蒸着，ほかには，TiO_2を含むオルガノシリケート（商品名チタニウムシリカフィルム）を回転塗布法により塗布して400 °C 以下でベーキングすることにより行い，それぞれ最適厚さ70～80nm形成した。

2.2.2　電極形成技術

前年度までの研究で，セル面積の拡大，変換効率の増大に伴う光照射時の電流増大に対応するため，直列抵抗の小さい電極形成技術の開発の必要性が指摘された。この問題は，Ti-Ag 二層金属電極とSi 表面との接触抵抗の低下及び半田ディップ法による電極抵抗の低下によって解決することとし，本年度は半田ディップ法の効果を基礎的に検討して技術的改善を行った。

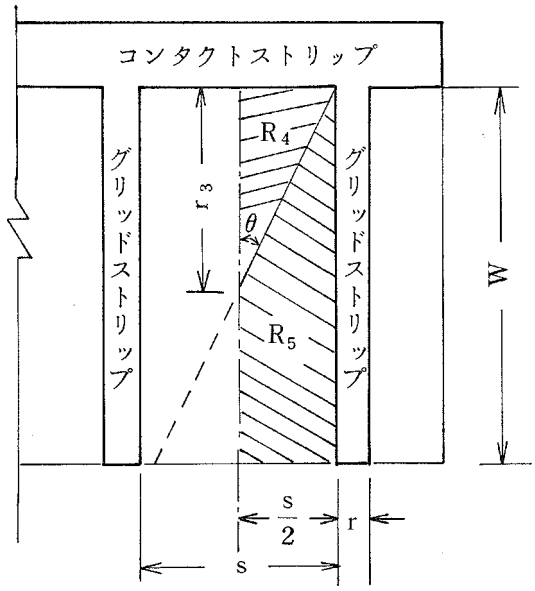

図 2.3　太陽電池の受光面要素

本年度採用した魚骨形電極のような場合，図2.3に示すような受光面要素についてはHandy(R. J. Handy, Solid-State Electronics, Vol.10, 765(1967)の解析が適用でき，太陽電池の直列抵抗（Rs）は次式で表わされる。

$$R_s = \frac{R_c}{1 + R_c / R_p} + R_1 + R_6 + R_7 + R_8 \qquad (2-1)$$

$$R_c = f(R_1, R_2, R_3, R_4, R_5) \qquad (2-2)$$

$$R_p = \frac{2R_c(R_c + R_1)}{(n-1)(2R_c + R_1)} \qquad (2-3)$$

ここで各パラメータは図2.4に示すように，

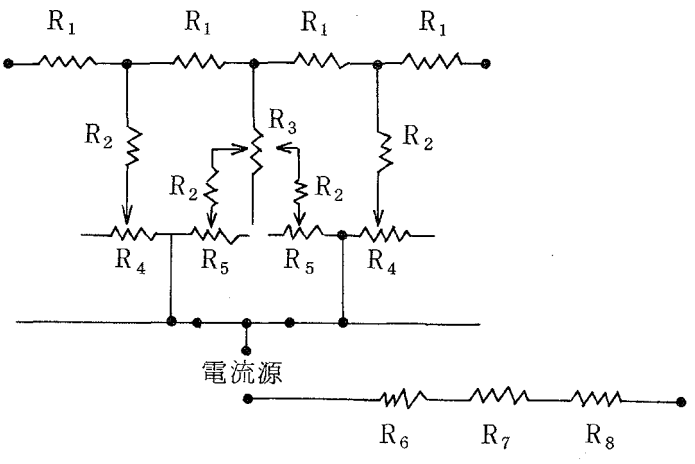

図 2.4　太陽電池の等価抵抗回路

R_1：コンタクトストリップの抵抗

R_2：表面層と電極間の接触抵抗

R_3：グリッドストリップの抵抗

R_4：コンタクトストリップへ流れるキャリヤの表面層の抵抗

R_5：グリッドストリップ へ流れるキャリヤの表面属の抵抗

R_6：p層の抵抗

R_7：p＋層と電極間の接触抵抗

R_8：電極抵抗

n　：2㎝長さに存在するグリッド本数

$$R_4 = \frac{\rho \times r_3 \times \cos\theta}{s \times t} \qquad (2-4)$$

ρ　：n^+層の比抵抗

r_3：R_4 と R_5 のポテンシャルが等しい長さ

s　：グリッド間の長さ

t　：n^+層の厚さ

である。

本報告で述べた太陽電池の構造では，$R_1 \approx R_2 \approx R_6 \approx R_7 \approx R_8 \approx 0$ であるから

$$R_s = \frac{R_c}{1 + R_c / R_p} \qquad (2-5)$$

$$R_p = \frac{R_c}{n-1} \qquad (2-6)$$

となり，式（２－５）と（２－６）から

$$R_s = R_c / n \qquad (2-7)$$

と簡略化される。また，R_c は

$$R_c = \frac{R_4 (2R_3 + R_5)}{4R_3 + 2(R_4 + R_5)} \qquad (2-8)$$

となる。W＝２cm，s＝４mmとしてr_3を求めると，r_3=0.45cm となる。n^+層の比抵抗ρ＝４×$10^{-3}\Omega \cdot cm$（キャリヤ濃度３×10^{19} cm^{-3}）についてR_4 と R_5 を求めると

$$R_4 = \frac{45}{t_{n^+}} \qquad (2-9)$$

$$R_5 = \frac{2.1}{t_{n^+}} \qquad (2-10)$$

t_{n^+}：n^+層の厚さ（μm）

となり，t_{n^+}=0.5μm では R_4=90Ω，R_5=4.2Ω となり，$R_4 \gg R_5$ である。一方，電極が Ａｇから成るとすると，R_3は次式で記述できる。

$$R_3 = \frac{1.1}{t_g} \qquad (2-11)$$

t_g：電極の厚さ（μm）

したがって，R_s は

$$R_s = \frac{1}{n}\left\{\frac{45}{t_{n^+}} \left(\frac{2.2}{t_g} + \frac{2.1}{t_{n^+}}\right) \Big/ \left(\frac{4.4}{t_g} + \frac{94}{t_{n^+}}\right)\right\} \qquad (2-12)$$

となる。

$t_{n+}=0.5\mu m$, $t_g \geqq 5\ \mu m$の場合についてR_sを計算すると

$$R_s=0.44\Omega$$

となり，電極抵抗は無視できる。セル面積を4 cm^2とすれば，$R_s=1.8\Omega\cdot cm$ となる。また，t_gが2μmのときのR_sを算出すると，$R_s=0.50\Omega$となり，電極抵抗をn^+層の抵抗の約$\frac{1}{10}$に低下することができる。

以上のR_sに関する検討により，現状のR_sはn^+層の抵抗に依存していることが明らかとなった。n^+層の比抵抗を下げることはエピタキシャル法でn^+層を形成する方法によるときは限界があり，グリッド電極の本数を増やす方が簡単である。しかしながら，現状では電極間隔の曲線因子に対する影響がそれほど顕著でない。いずれにしても，直列抵抗中の電極抵抗の影響を無視するためには，電極を数μm以上と厚くする必要がある。開発した半田ディップ法は数十μm厚の電極を形成することは容易であるので，電極抵抗を無視でき，セルの直列抵抗としてはn^+層の抵抗のみ考慮すれば良いことになる。グリッド本数10本でセル面積15 cm^2の場合，セルの直列抵抗の計算は1.0 $\Omega\cdot cm^2$となる。この計算値は実測値2.12 $\Omega\cdot cm^2$の約$\frac{1}{2}$でかなり良い一致を示した。多結晶薄膜太陽電池では，表面に凹凸があるため，n^+層や電極の厚さの薄い箇所が存在する可能性があり，このことが計算値と実測値の相違の原因であると考えられる。

2.3　薄膜セル特性の評価

2.3.1　セル特性の評価法

光電変換特性の測定は小型のAMOソーラシミュレータを使用し，短波長域をカットしたAM1擬似スペクトルをもつ100mW/cm²の光照射のもとで測定を行った。照射光エネルギーの較正はNBS標準に準拠したエプレー社製のサーモパイル及びテーブルマウンテンにおいて気球較正の標準と比較較正したスペクトロラブ社製標準太陽電池を用いたが，測定値に10%程度の差を生じたため，最終的には感度の高い太陽電池の方を基準として採用した。すなわち，これにより得られる変換効率の値はサーモパイルを用いて光源強度設定を行った場合よりも若干低目となる。また測定される電流値の絶対誤差は±数%以内であると推定される。

太陽電池の電流－電圧特性の測定は通常直列に挿入した可変抵抗を操作して端子間の電流及び電圧を測定したが，単位太陽電池の容量が増大して内部抵抗が減少し，短絡条件が実現しにくくなったため，図2.5に示すような方式の電子負荷装置を開発した。

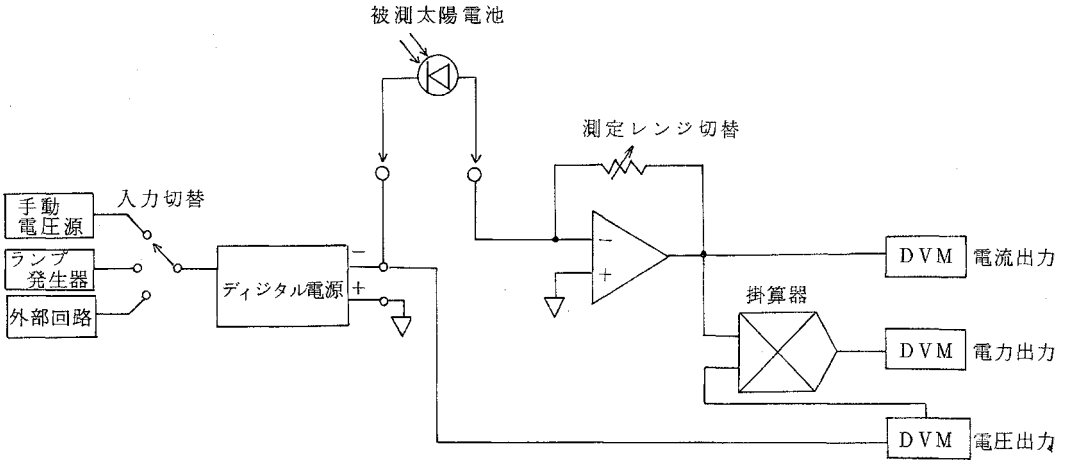

図2.5　太陽電池特性測定装置

測定中の太陽電池温度は測定時に試料台として用いる温度制御された金属ブロックの温度をとったが，照射中の開放電圧の変化は１mV以下であり，太陽電池の開放電圧の温度係数から推定する限り，セル表面温度との差は１度以内にあると思われる。

分光感度特性は通常一定エネルギー（１5.2μW/cm^2，帯域～７nm）モードで測定した。深い不純物を多量に含む場合，一般に分光感度特性には光源強度依存性があり，低エネルギー密度の光で測定した場合には若干問題は残るが，装置の都合上特に白色バイアス光照射等は行っていない。また照射面積は太陽電池の受光面積より小さく，格子状電極による部分的遮蔽及び太陽電池の不均一性に基づく誤差等が含まれるため，分光感度の測定値に関しては若干の誤差を考慮する必要がある。

太陽電池のダイオードパラメータの算出には，2.4で詳述するように昨年度に開発したコンピュータシミュレーション法を用いた。

また，光電変換特性の不均一性の評価には昨年度開発したレーザ走査法を用いた。

2.3.2　金属級シリコンから作製した基板上の薄膜セル

(1)　CZ法により一回結晶化した場合

金属級シリコンから作製した多結晶インゴット（ME）をスライスして得たウェーハを基板として用い，気相エピタキシャル法でp層及びn^+層を形成して成長接合とし，表面にグリッド電極を形成し，周辺をメサエッチしてセルを構成した。光学活性層であるp形成長層の厚さは37μm，キャリヤ濃度は$7.5\times10^{16}\ cm^{-3}$，$n^+$形成長層の厚さは0.55$\mu m$，キャリヤ濃度は$3\times10^{19}\ cm^{-3}$である。作製した太陽電池の光電変換特性を表2.1

に示す。

表2.1　金属級シリコンから作製した結晶上にエピタキシャル法で作製した薄膜太陽電池の光電変換特性
（引上げ速度 1.2㎜／min）

No.	セル面積[1] (cm^2)	短絡電流[2] (mA／cm^2)	開放電圧 (V)	曲線因子	変換効率 (%)
ME12	15.2	12.5	0.514	0.560	3.60
ME17	15.2	12.2	0.511	0.659	4.11
ME13	15.2	12.2	0.498	0.627	3.80
ME18	15.0	11.5	0.502	0.638	3.69
DME12[3]	9.0	16.4	0.581	0.757	7.21

1）電極面積を含む。反射防止膜なし。

2）光照射条件：AM1，100mW／cm^2。

3）比較のための単結晶を基板に用いたエピタキシャルセル。

短絡電流値は約12mA／cm^2（反射防止膜なし）とほぼ一定で，この値は比較のために同一処理で作製した単結晶エピタキシャルセル（DME12，DME25）の値の約75％に相当し，多結晶の場合に顕著な結晶粒界での光電流の損失を考慮すれば，かなり大きな値であるといえる。しかし，このダミーの単結晶セル自身については，拡散法で形成した従来構造のセルと比べると開放電圧(Voc)及び曲線因子（FF）はほぼ同等であるが，短絡電流(Isc)のみ20～30％低い。この原因の一つは光吸収層であるp層の厚さが37μmと薄いため長波長側の光を損失していることによる。この厚さによる損失分は約10％と見積られるので，残りの10～20％については光学活性層のライフタイ

ムが減少したと考えざるを得ない。ステップリカバリー法で求められたライフタイムは1～2μsで，この値は単結晶セルの値（0.5～20μs）では低い方に属し，低純度の基板と同一雰囲気でエピタキシャル成長をさせる場合，低純度基板から放出される有害な不純物のオートドーピング効果は無視し得ないと思われる。

金属級シリコン基板上にエピタキシャル成長させて形成したセルでは，変換効率は平均4％，（反射防止膜を被着すれば5％以上になる）で，特に注目すべき点は，セル間の効率の変動が少い点である。これは，後述のように多結晶接合の漏洩電流が予想以上に少く，曲線因子の変動が少いことに起因している。

次に基板中に含まれる不純物濃度の影響を調べるため，同一インゴット中の引上げ速度の異なる領域から得たウェーハを基板としてエピタキシャル法でセルを形成した。その結果を表2.2に示す。

表2.2　金属級シリコンから作製した結晶上にピタキシャル法で作製した薄膜太陽電池の光電変換特性
（引上げ速度　0.14 mm／min）

No.*	セル面積[1] (cm^2)	短絡電流[2] (mA／cm^2)	開放電圧 (V)	曲線因子	変換効率 (%)
ME 231	5.28	11.6	0.503	0.657	3.82
ME 232	6.78	10.8	0.497	0.697	3.74
ME 241	4.86	13.2	0.475	0.573	3.58
ME 242	6.09	11.9	0.484	0.652	3.76
ME 251	5.58	11.6	0.490	0.674	3.83
ME 252	4.15	11.8	0.496	0.656	3.70
ME 261	5.29	11.3	0.499	0.689	3.87
DME25[3]	7.17	14.5	0.578	0.698	5.85

1） 電極面積を含む。反射防止膜なし。

2） 光照射条件：AM1，100mW／cm^2 。

3） 比較のための単結晶を基板に用いたエピタキシャルセル。

＊ p層の厚さ：ME231～ME242（24μm）

ME251～DME25（50μm）

同じMEの結晶でもME1のシリーズに比較してME2シリーズが若干純度が改善されているが，光電変換特性ではこの差は出ていない。また，基板の上に成長させたp形層の厚さに対しても短絡電流値に有意差は見られず，成長させたp形層中のキャリヤの拡散距離が短かいことを示唆している。

次に，多結晶接合の評価のため，金属シリコン基板上にp形層をエピタキシャル成長後，エピタキシャル法と拡散法で接合を作り，それらのセル特性を測定し比較した。表2.3はその結果で，短絡電流はほぼ等しいが，開放電圧と曲線因子は成長接合法の方が大きく，変換効率もやや高くなっている。この原因は，拡散では粒界拡散が大きく，接合面に不均一性が多いが，これに比べて成長接合では，接合は平滑で漏洩電流が減少するためであると考えられる。

表2.3 薄膜太陽電池の光電変換特性に対する成長接合と拡散接合の比較

No.		セル面積（cm^2）	短絡電流（mA／cm^2）	開放電圧（V）	曲線因子	変換効率（%）
拡	ME 321	4.75	11.0	0.445	0.644	3.15
散	ME 322	14.0	11.3	0.479	0.606	3.28
成	ME 331	8.48	11.9	0.488	0.685	3.98
長	ME 332	13.45	12.0	0.483	0.670	3.87

光学活性層内に不純物濃度勾配を設け，接合面と垂直に内部電界を形成することにより，光学活性層内のキャリヤの拡散距離を実効的に伸すことが可能である。特にエピタキシャル成長の場合，この不純物濃度勾配を制御して形成できるのが特長である。ME 2の基板を用いて，厚さ50μmのp形層中のほう素濃度を基板から接合に向けて10^{18}～$10^{16}\ cm^{-3}$に制御して形成したセルの特性を表2.4に示す。

表2.4　金属級シリコンから作製した結晶上に10^{18}～$10^{16}cm^{-3}$の濃度勾配を設けてエピタキシャル成長させた薄膜太陽電池の光電変換特性

No.	セル面積 (cm^2)	短絡電流 (mA/cm^2)	開放電圧 (V)	曲線因子	変換効率 (%)
ME272	10.2	12.4	0.503	0.672	4.17

n^+層が0.55μmと若干厚いためにIscはやや低くなっているが，p層中の不純物濃度が一定の場合に比べ増加傾向がみられ，この方式により，金属級シリコンから一度結晶化しただけの多結晶を用いても変換効率が4.2％（反射防止膜を付けた場合では5.42％）のセルが得られることがわかった。

結晶成長条件によっては，金属級シリコンから直接溶融結晶化を行う場合でも単結晶が得られる場合がある。再現性は悪く，途中から多結晶化するなど主要プロセスとはなり得ないが，参考のため，この様なp形単結晶インゴットを用いて直接拡散して接合を作ったセル及び，上記と同様にエピタキシャル成長により活性層を形成して作ったセルの光電変換特性を表2.5に示す。なお基板結晶は0.08 Ω·cm，(111)面であり，エピタキ

表 2.5　金属級シリコンから1回の結晶化で得られた単結晶上に拡散あるいはエピタキシャル成長により形成した太陽電池の光電変換特性

No.	接合形成法	n^+ 層		光電変換特性[1]				
		シート抵抗 (Ω/口)	接合深さ (μm)	セル面積 (cm^2)	短絡電流 (mA/cm^2)	開放電圧 (V)	曲線因子	変換効率 (%)
MC 40	拡散	6	1.0	4.52	3.74	0.293	0.488	0.49
MC 49		6	1.0	4.52	3.54	0.413	0.657	0.96
MC 45		32	0.60	4.15	7.01	0.393	0.387	1.07
MC 46		32	0.60	4.15	7.28	0.510	0.600	2.23
MC 47		54	0.26	3.81	6.61	0.387	0.411	1.05
MC 43	エピタキシャル	65	0.48	3.46	12.4	0.538	0.445	2.97
MC 44		65	0.48	3.63	13.9	0.559	0.702	5.45

1)　AM1（100mW/cm^2）での値。反射防止膜なし。

シャル成長は，p形層が厚さ33μm，キャリヤ濃度$8\times10^{16}cm^{-3}$で，n^+層は$2.5\times10^{19}cm^{-3}$である。

拡散で接合形成した場合にも最高2.2％（反射防止膜付きで2.9％以上）が得られているが，短絡電流値が小さく，これは表1.1に示したように深い準位を形成する不純物が結晶中にppmオーダと比較的多量に含まれていることに起因している。一方エピタキシャル成長で光学活性層を形成したものでは最高5.5％で，反射防止膜を付けた場合には7.1％となり，薄膜を形成する方が変換効率の上ではるかに有利と言える。

また，一回の結晶化で得られる多結晶と，たまたま単結晶になった場合との比較では，単結晶化した方の基板を用いた場合により高い変換効率が得られているが，これはこの場合のように不純物濃度が高い場合には結晶粒界に析出する不純物が多く，

それが光学活性層を成長させる際に活性層中に取込まれるために，このような結果になっているためと思われる。多結晶であるための粒界による光電変換特性の低下は無視できないが，粒径が㎜級の場合にはそれ程問題にならないことについては昨年度の報告のとおりである。

(2) CZ法により二回繰り返して溶融結晶化した場合

金属級シリコンから直接結晶化を行って得られる多結晶インゴットでは，結晶粒中に多量の不純物を含んでおり，結晶内部あるいは粒界での不純物析出がエピタキシャル成長中の雰囲気ガスを汚染し，あるいは直接拡散源となって光学活性層中に取り込まれるため，太陽電池の変換効率を向上させることがむずかしい。そこで，一度金属級シリコンから引上げて得られた多結晶インゴットをソースとし，これを融解して再びチョクラルスキー法で結晶引上げを試みた（MF結晶）。このようにして得られたインゴットはかなりの部分が単結晶に近い状態となった。これをスライスして得たウェーハを基板とし，同様な方法により太陽電池を形成した。その結果を表2.6に示す。ここでMF1のシリーズは結晶の引上げ速度が0.11㎜/minで，MF2のシリーズは同0.5㎜/min の部分からそれぞれスライスしたウェーハを基板としている。また，n^+層はいずれもエピタキシャル法で形成した。

一回の結晶化で得られた多結晶インゴットを基板としたMEシリーズに比較し，短絡電流，開放電圧，曲線因子共に改善され，反射防止膜なしの状態で5～6％の変換効率が得られた。短絡電流が13.5～14.5mA/㎠で同時に形成したダミーの高純度単結晶ウェーハ上のセル（DMFシリーズ）と同程度のレベルに達している。

表 2.6　金属級シリコンから2回結晶化した結晶を基板としてエピタキシャル法により形成した薄膜太陽電池の光電変換特性

No.	p 層		n^+ 層		光電変換特性[1]				
	厚さ (μm)	キャリヤ濃度 (cm^{-3})	厚さ (μm)	キャリヤ濃度 (cm^{-3})	セル面積 (cm^2)	短絡電流 (mA/cm^2)	開放電圧 (V)	曲線因子	変換効率 (%)
MF1−16	32	1.7×10^{17}	0.50	2.5×10^{19}	18.1	13.5	0.585	0.706	5.59
MF1−18	32	1.7×10^{17}	0.45	2.1×10^{19}	18.1	13.3	0.585	0.654	5.06
MF1−20[2]	36	2×10^{18} ～2×10^{16}	0.50	2.5×10^{19}	19.7	14.5	0.586	0.704	5.98
MF1−22[2]	36	2×10^{18} ～2×10^{16}	0.45	2.1×10^{19}	18.1	14.3	0.590	0.701	5.92
MF2−4	25	2.5×10^{17}	0.50	1×10^{19}	19.6	13.2	0.570	0.678	5.07
MF2−6	25	2.5×10^{17}	0.50	1×10^{19}	9.8	13.1	0.564	0.612	4.54
MF2−8	50	2.5×10^{17}	0.50	1×10^{19}	16.1	13.3	0.578	0.745	5.75
MF2−10	50	2.5×10^{17}	0.50	1×10^{19}	10.0	13.1	0.573	0.775	5.83
DMF1−20[2,3]	36	2×10^{18} ～2×10^{16}	0.45	2.1×10^{19}	12.6	15.8	0.587	0.750	6.97
DMF2−8[3]	50	2.5×10^{17}	0.50	1×10^{19}	4.7	13.5	0.583	0.731	5.76

1)　AM1（100mW/cm^2），反射防止膜なし。28°C。

2)　p層中に基板から接合に向けて不純物濃度勾配を設けた。

3)　比較のために低比抵抗高純度単結晶上に形成したセル。

これはエピタキシャル成長層中のキャリヤの拡散距離が長くなったためで，p形層の厚さが増加すると短絡電流も増加することからも裏づけられる。更に開放電圧，曲線因子の増加は，エピタキシャル層中で深い準位を形成する不純物が減少し，そのために飽和電流が減少したこと，及び粒界部分の減少と共に並列抵抗が増大してきたことなどが相乗的に働いた結果と思われる。

このシリーズの太陽電池に反射防止膜を被覆した場合の代表的な電流－電圧特性を図2.6に示す。p形層が一様なドーピングレベルの場合には，短絡電流は16～17mA/cm²，開放電圧0.58～0.59V，曲線因子0.64～0.77で変換効率は6.3～7.6

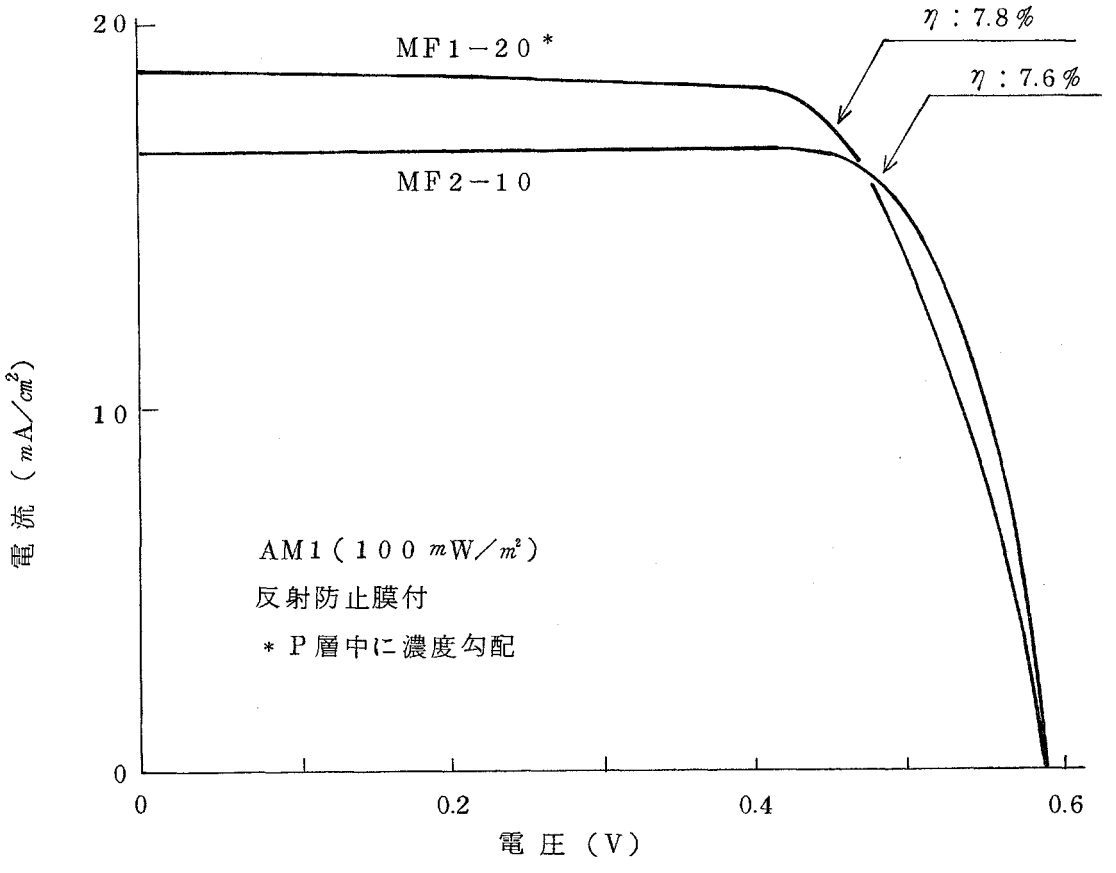

図2.6　金属級シリコンから2回溶融結晶化した結晶上にエピタキシャル法で形成した薄膜太陽電池の電流－電圧特性

%が得られた。一方，p形層中のドーピング不純物に濃度勾配を付けた場合には短絡電流が19mA／cm^2までのものが得られ，このシリーズ最高の変換効率7.8％が得られた。

2.3.3　精製した金属級シリコンから作製した基板上の薄膜セル

(1)　一回の結晶化の場合

Ⅱ.1で述べた精製した金属シリコンをソースとし，ここからチョクラルスキー法で作製した多結晶インゴット（MSA，MSC結晶）をスライスして得たウェーハを基板に用いて，前述と同様な方法で光学活性層をエピタキシャル法で形成し，太陽電池を形成した。その光電変換特性を表2.7に示す。

精製していない通常の金属級シリコンから引上げた多結晶インゴットを基板に用いた場合（表2.1，表2.2参照）に比較し，短絡電流が2～3 mA／cm^2向上して14～15mA／cm^2のレベルに達し，また開放電圧も30～40mV向上して0.52～0.55Vに改善された。この結果，変換効率は前者の4％から，原料の精製により～5％の水準に向上した。これは反射防止膜付きの場合には～6％に相当する。

(2)　2回繰り返して結晶化した場合

精製した金属級シリコンから一度チョクラルスキー法で作製した多結晶インゴットを再びソースとして，更にチョクラルスキー法によって結晶成長を行うと，大部分が単結晶のインゴットが得られる（MSD結晶）。その中央部分をスライスして得たウェーハを基板として，厚さ約40μmのp形層をドーピング濃度10^{18}～$10^{16}\,cm^{-3}$の濃度勾配を設けて形成し，850℃で表面からりんの拡散を行って厚さ0.31μmのn^+層を形成して太陽電池を製作した。同じ形成条件で製造したセルの光電変

表 2.7　精製した金属級シリコンから作製した多結晶上にエピタキシャル法で形成した薄膜太陽電池の光電変換特性

No.	p 層		n^+ 層		光電変換特性[1]				
	厚さ (μm)	キャリヤ濃度 (cm^{-3})	厚さ (μm)	キャリヤ濃度 (cm^{-3})	セル面積 (cm^2)	短絡電流 (mA/cm^2)	開放電圧 (V)	曲線因子	変換効率 (%)
MSA2−8	23	2×10^{17}	0.40	2×10^{19}	14.4	16.9	0.559	0.689	6.52
MSA2−11	23	2×10^{17}	0.40	2×10^{19}	14.7	13.9	0.541	0.682	5.14
MSA2−1	39	2×10^{18}〜2×10^{16}	0.40	2×10^{19}	12.6	15.0	0.537	0.667	5.38
MSA2−2	39	2×10^{18}〜2×10^{16}	0.40	2×10^{19}	12.4	15.2	0.543	0.693	5.72
MSA3−2	38	2×10^{18}〜2×10^{16}	0.36	2×10^{19}	16.6	14.4	0.527	0.639	4.84
MSA3−8	38	2×10^{18}〜2×10^{16}	0.36	2×10^{19}	4.91	13.5	0.523	0.593	4.19
MSA3−4	38	3×10^{17}〜2×10^{16}	0.38	2×10^{19}	19.6	13.4	0.523	0.641	4.45
MSC 1	39	3×10^{16}	0.40	3×10^{19}	12.9	13.3	0.517	0.623	4.29
MSC 2	39	3×10^{16}	0.40	3×10^{19}	11.4	13.2	0.517	0.687	4.70
MSC 8	33	2×10^{18}〜2×10^{16}	0.32	3×10^{19}	12.6	14.3	0.535	0.672	5.13
MSC 9	33	2×10^{18}〜2×10^{16}	0.32	3×10^{19}	12.6	14.4	0.535	0.648	5.00
DMSA2[3]	39	2×10^{18}〜2×10^{16}	0.40	2×10^{19}	17.7	16.6	0.572	0.690	6.51

1) 測定はAM1（100mW/cm^2），反射防止膜なし。

2) p層中にドーピング不純物の濃度勾配を付けたもの。

3) 比較のための高純度単結晶ウェーハを基板としたダミーセル。

換特性を表2.8にまとめて示す。

反射防止膜を形成しない場合では，平均21cm^2のセルにおいて，短絡電流15mA/cm^2，開放電圧0.59V，曲線因子0.70が得られ，変換効率は6.2％であった。これに反射防止膜を付加した場合の測定では，短絡電流20mA/cm^2，開放電圧は0.6Vを越え，曲線因子は0.67と若干下るが，変換効率では平均で8.0％，最高8.59％が得られた。

製作したセル群のうち，特性の低い2個のセルを除いたほかのセルの電流－電圧特性を図2.8に示す。

表2.8　精製した金属シリコンから2回結晶化した結晶上にエピタキシャル法で形成した薄膜太陽電池の光電変換特性[1)]

		セル面積 (cm^2)	短絡電流 (mA/cm^2)	開放電圧 (V)	曲線因子	変換効率 (％)
反射防止膜なし[2)]	範囲	19.5－22.4	14.5－15.6	0.586－0.594	0.658－0.726	5.59－6.69
	平均	21.2	15.1	0.589	0.702	6.24
	標準偏差〔％〕	－	0.29〔1.9〕	0.0023〔0.40〕	0.0220〔3.1〕	0.297〔4.8〕
反射防止膜形成後[3)]	範囲	19.4－22.4	19.1－20.5	0.598－0.612	0.633－0.711	7.41－8.59
	平均	20.9	19.8	0.606	0.667	8.01
	標準偏差〔％〕	－	0.37〔1.9〕	0.0036〔0.59〕	0.0192〔2.9〕	0.320〔4.0〕

1）測定はAM1（100mW/cm^2）28°C。

2）試作セル数：16個。

3）試作セル数：19個。

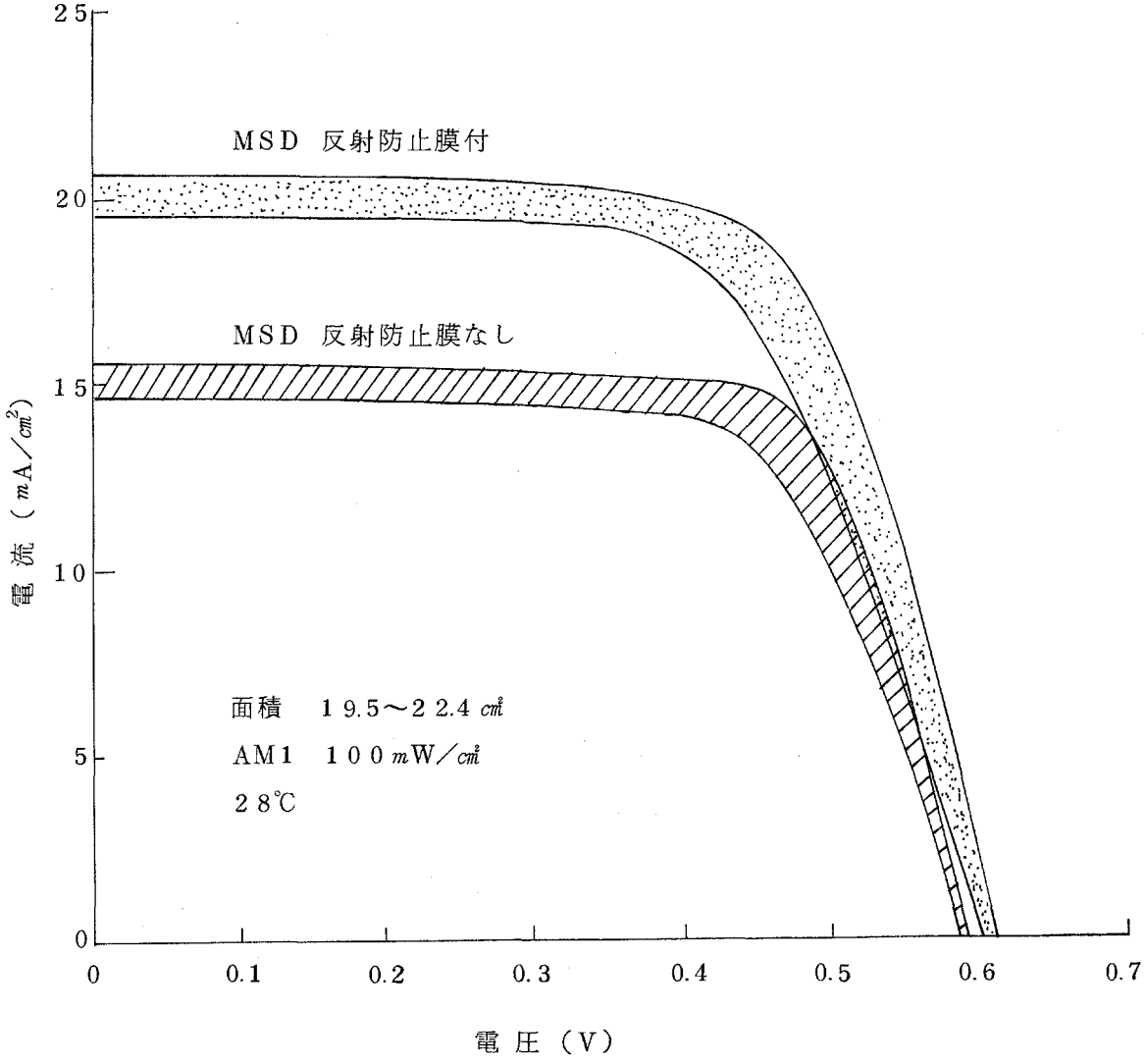

図 2.8　精製した金属級シリコンを2回溶融結晶化した結晶上にエピタキシャル法で形成した薄膜太陽電池の電流－電圧特性。同条件で形成した16セルのうち14セルの特性範囲。

2.3.4　基板の種類と光電変換特性

(1)　光電変換特性

これまで通常の金属級シリコンから直接作製した結晶（MC，ME），更にMEをソースとして作製した結晶（MF），及び，精製した金属級シリコンをソースとして作製した結晶（MSA，MSC），更にMSCをソースにして作製した結晶（MSD）の四種類の基板について，その上にエピタキシャル法で形成した太

陽電池を中心とした実験結果を述べてきたが，基板結晶の品質向上に伴い，基板結晶に直接拡散により接合を形成し，太陽電池を形成することも可能であり，ここではその実験結果について述べる。

用いた基板は引上げによって得られたインゴットをスライスした厚さ0.4㎜程度のウェーハであり，弗硝酸系のエッチ液でその表面を50μm位エッチングして除去したものを用いた。拡散接合形成の条件は，エピタキシャル法によって形成したp形層に対する拡散接合形成と同様であるが，結晶性あるいは基板の純度等により，得られる接合深さは異なる。MCについての実験結果は表2.5について述べたが，比較のために再録し，まとめて次の表2.9に示す。

表2.9　金属級シリコンから作製した結晶に直接拡散により接合を形成して製作した太陽電池の光電変換特性

セル		接合深さ (μm)	光電変換特性 1)				
結晶	No.		セル面積 (cm^2)	短絡電流 (mA/cm^2)	開放電圧 (V)	曲線因子	変換効率 (%)
金属級シリコンから直接結晶化した多結晶	ME 2	0.5	19.5	5.23	0.212	0.30	0.33
金属級シリコンから直接結晶化した単結晶	MC46	0.6	4.15	7.28	0.510	0.600	2.23
精製した金属級シリコンから直接結晶化した多結晶	MSA2-13	0.24	13.7	9.20	0.530	0.578	2.94
	MSC6	0.26	13.3	7.95	0.509	0.517	2.09
精製した金属級シリコンから2度結晶化した結晶	MSD46	0.42	12.6	10.5	0.538	0.602	3.37

1) 測定はAM1（100mW/cm^2），反射防止膜なし。

金属級シリコンから直接結晶化した多結晶でも比抵抗が0.07Ω·cmのレベルにあり，特性は良くないが一応の整流性を示し，反射防止膜なしの状態でも5.2mA/cm²の短絡電流が得られる。しかし開放電圧，曲線因子が低いため，得られる効率は0.33%程度である。同じソースから成長した単結晶の場合には，結晶粒界への不純物析出の分だけ多結晶に比べて有利であり，開放電圧，曲線因子共大幅に改善され，変換効率も2.2%までのものが得られる。なお金属級シリコンから2回結晶化したMFの結晶では故意に高濃度のほう素ドーピングを行っているため，直接拡散によってはダイオード特性は得られずここには示していない。

一方，精製した金属級シリコンでは一回の結晶化で得られる結晶では，短絡電流が8～9mA/cm² と通常の金属シリコンの場合に比べて増加しており，接合が浅いための効果を考えても精製の効果は明らかである。二回結晶化した場合にも短絡電流は10mA/cm²を越え，変換効率も3.4%近くまでのものが得られた。

(2) 分光感度特性

金属級シリコンから引上げたMEのセルでは暗電流が大きく低レベルの照度での光応答が低いため，信頼できる分光感度特性は得られていない。精製した金属シリコンの場合について，一回結晶化した結晶(MSC)及び二回結晶化した結晶(MSD)につき，それぞれ直接拡散によって接合を形成した場合と，エピタキシャル法によって薄膜を形成した場合とにつき測定した分光感度特性を図2.9に示す。

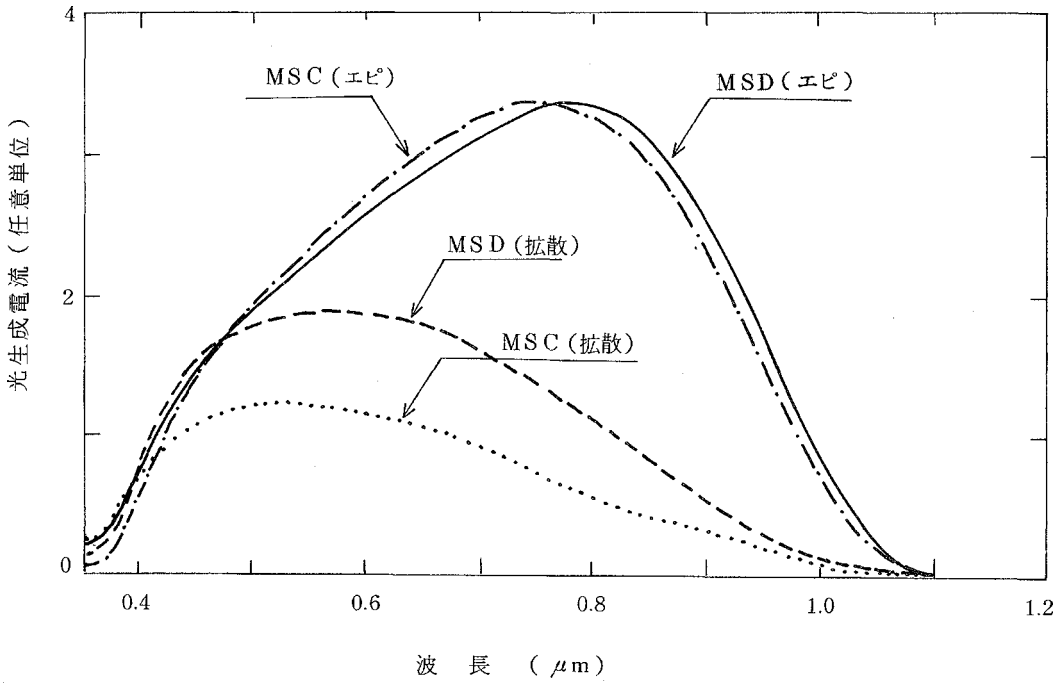

図 2.9　精製した金属級シリコンから１回結晶化した結晶（ＭＳＣ）及び２回結晶化した結晶（ＭＳＤ）を用いて拡散及びエピタキシャル成長によって形成した太陽電池の分光感度特性

直接拡散による場合には，一回結晶化した場合と二回結晶化した場合ではピーク感度がそれぞれ 0.5μm と 0.6μm にあり，引上げの繰り返しにより長波長感度及び全体の感度が向上している。一方，エピタキシャル成長させたセルの場合には，いずれも 0.8μm 近傍にピーク感度があり，従来構造の単結晶セルと類似した分光感度特性をもつ。エピタキシャル層の厚さにより長波長感度は若干の差が出るが，それ以上にキャリヤの拡散距離が改善された結果を示している。

分光感度特性から光学活性層中のキャリヤの拡散距離を求める方法については昭和５１年度の成果報告で詳述したが，その方法により図 2.9 に示したセルについて求めた結果を図 2.１０に示す。これから，精製した金属級シリコンについても一回結晶化

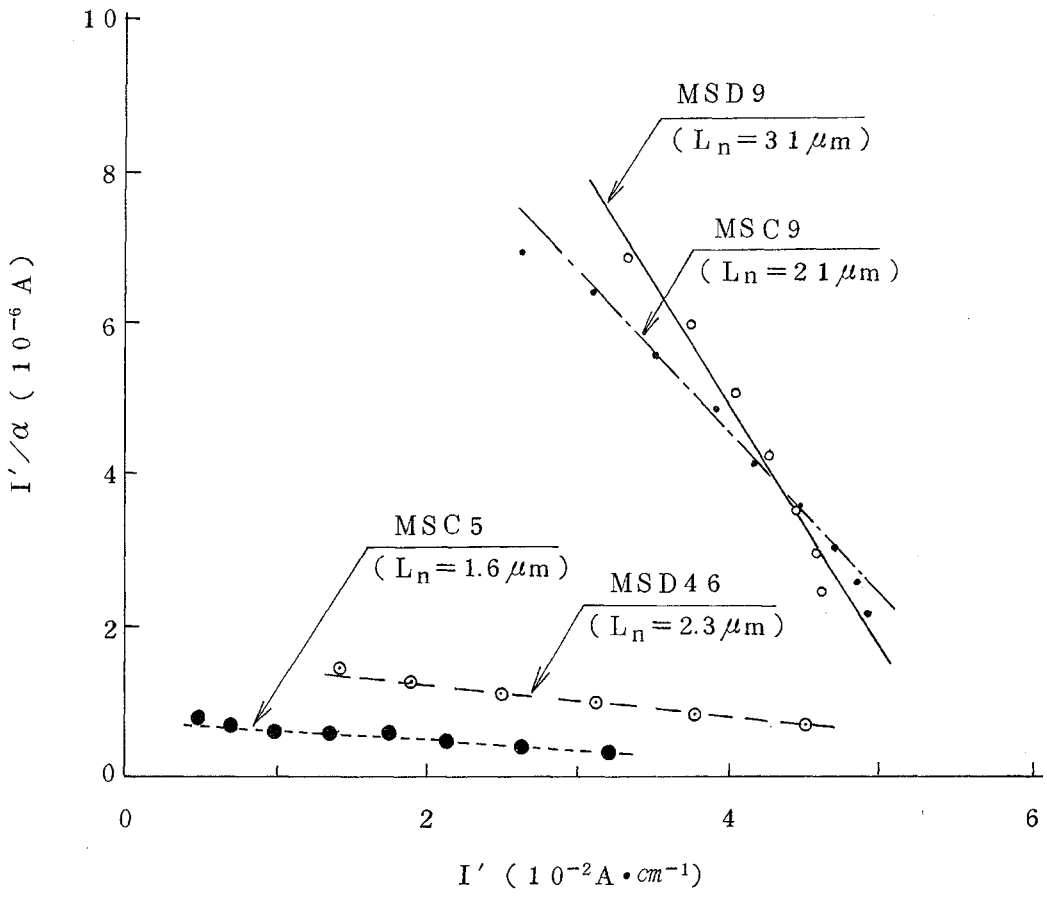

図 2. 1 0　分光感度特性から光学活性層内でのキャリヤ拡散距離を求めるためのプロット。

して得られる結晶についてはキャリヤの拡散距離は 1.6μm 程度で，再度結晶化してもこれが 2.3μm に改善される程度であることがわかる。一方これらの結晶の上にエピタキシャル成長させた薄膜では，それぞれについて 2 1μm，3 1μm と大きく改善されるが，基板結晶の純度が成長層の特性に大きく影響することが示されている。これについては後節で更に述べる。

(3)　光電変換特性のまとめ

これまでに述べた各種の太陽電池，すなわち，

①　金属級シリコンから直接結晶化してこれに拡散で接合を形成したセル

② この結晶上にエピタキシャル法で形成した薄膜セル

③ この結晶から更に溶融結晶化した結晶上にエピタキシャル成長で形成した薄膜セル

④ 精製した金属級シリコンから直接結晶化した結晶に拡散で接合を形成したセル

⑤ この結晶上にエピタキシャル法で形成した薄膜セル

⑥ この結晶から更に溶融結晶化してこれに拡散で接合を形成したセル

⑦ その結晶上にエピタキシャル法で形成した薄膜セル

について反射防止膜を形式したときの電流電圧特性をまとめて図2.11に示す。また光電変換特性のパラメータを表2.10に示す。

表2.10 試作した各種の太陽電池の光電変換特性

基板結晶	セル		面積 (cm^2)	光電変換特性[1]			
	製法	No		短絡電流 (mA/cm^2)	開放電流 (V)	曲線因子	変換効率 (%)
金属級シリコンから一回結晶化して得た多結晶	p層基板 n層拡散	ME-2	19.5	6.76	0.212	0.30	0.43
	p層エピ[2] n層エピ	ME-272	10.2	16.1	0.525	0.672	5.68
金属級シリコンから二回結晶化して得た結晶	p層エピ[2] n層エピ	MF1-20	19.7	18.9	0.586	0.704	7.77
精製した金属級シリコンから一回結晶化して得た多結晶	p層基板 n層拡散	MSC-6	13.3	10.3	0.532	0.531	2.90
	p層エピ[2] n層エピ	MSC-8	12.6	18.6	0.555	0.677	6.97
精製した金属級シリコンから二回結晶化して得た結晶	p層基板 n層拡散	MSD-46	12.6	12.2	0.559	0.601	4.09
	p層基板[2] n層拡散	MSD-13	20.8	20.2	0.607	0.702	8.59

1) 測定はAM1（100mW/cm^2），反射防止膜付き。

2) p形エピタキジャル層は10^{18}～10^{16} cm^{-3}のドーピング不純物濃度勾配付き。

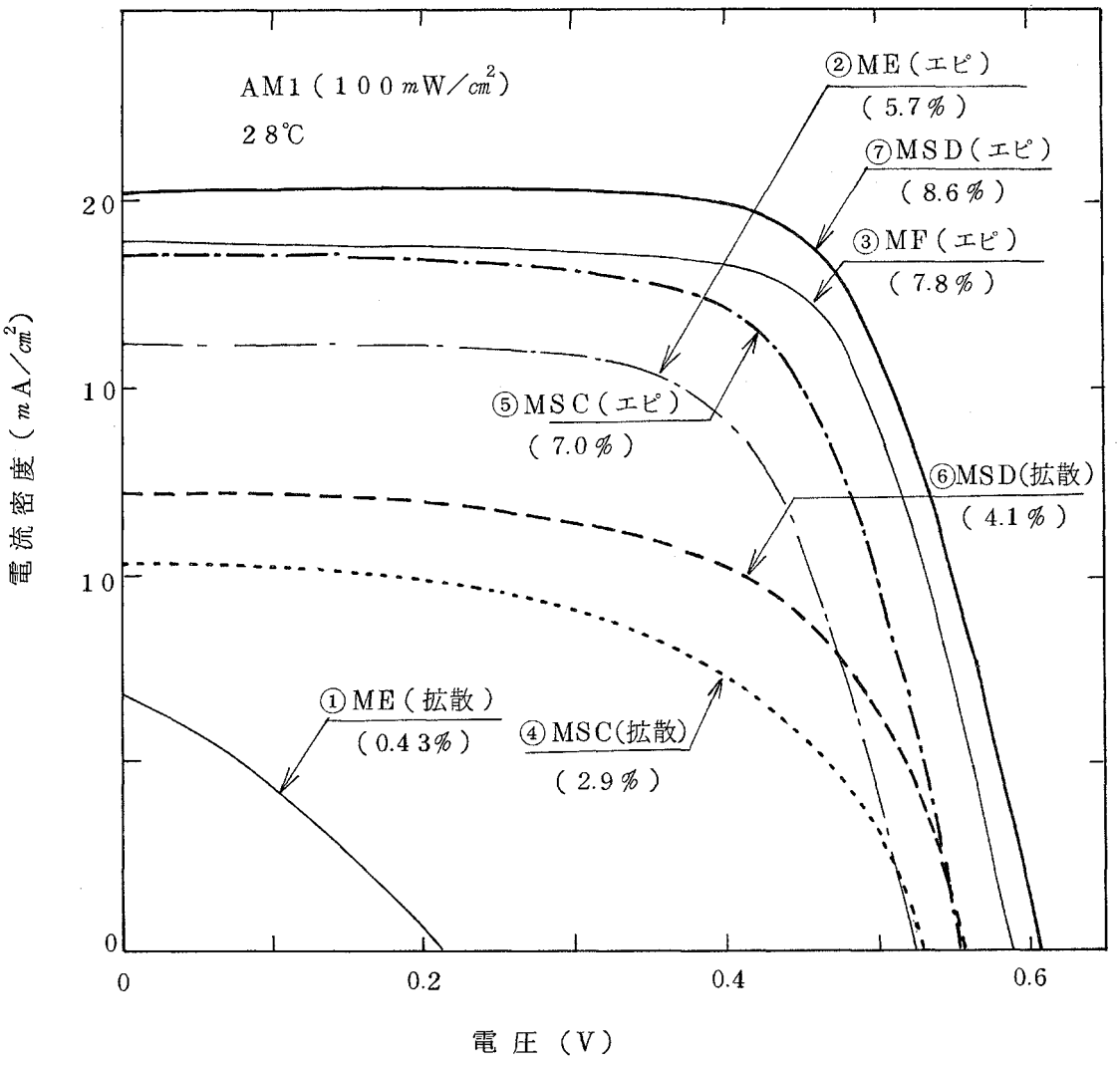

図2.11　試作した各種太陽電池の電流電圧特性

2.4　光電変換特性の解析

2.4.1　ダイオード・パラメータの計算

前節（2.3）で述べたように，現状のセルは単結晶セルに比べ短絡電流値が小さいだけでなく，開放電圧や曲線因子の値も下回っている。この原因を調べるため，前年度に研究開発したコンピュータシミュレーション法を適用し，次式で示した電流－電圧特性から各ダイオードパラメータを計算した。

$$J = -J_L + J_{01} \exp \frac{qV_d}{n_1 kT} + J_{02} \exp \frac{qV_d}{n_2 kT} + \frac{V_d}{R_{sh}} \qquad (2.13)$$

$$Vd = V - JR_S \qquad (2.14)$$

J_L：光電流　　J_{01}，J_{02}：飽和電流　　R_S：直列抵抗

R_{sh}：並列抵抗

$n_1 = 1$，$n_2 \geq 2$（二指数項表式）の場合と，$I_{02} = 0$（一指数項表式）の場合の解析結果を表2.11に示す。表2.12は解析したセルの光電変換特性である。MFシリーズとMSDシリーズは一指数項表式で$n_1 = 1$を示しており，拡散電流支配の理想的なダイオードとなっている。しかし，MEシリーズとMSCシリーズでは，空乏層内の再結合電流成分が大きいため，一指数項表式のn_1値は1.3～1.8となっている。次に，この計算を基に，変換効率を決める短絡電流，開放電圧及び曲線因子について詳細に検討した。

表2.11　多結晶太陽電池のダイオードパラメータ
（ただし，S10−41のみ高純度単結晶セル）

	Cell No.	n_1	J_{01} (A/cm²)	n_2	J_{02} (A/cm²)	R_S (Ω·cm²)	R_{sh} (Ω·cm²)	J_L (mA/cm²)
二指数項表式	ME17	1.0	1.01×10^{-11}	2.2	1.01×10^{-6}	2.12	1.56×10^{3}	12.3
	ME322	1.0	3.35×10^{-11}	2.2	1.60×10^{-6}	4.47	1.08×10^{3}	11.4
	MF1-20△	1.0	2.00×10^{-12}	2.0	1.99×10^{-9}	4.55	1.27×10^{3}	14.5
	MF2-10*	1.0	2.02×10^{-12}	2.0	2.75×10^{-9}	1.74	6.04×10^{3}	16.7
	MSC 2	1.0	1.47×10^{-11}	2.0	2.74×10^{-7}	2.51	3.67×10^{3}	13.3
	MSC 8 △	1.0	6.97×10^{-12}	2.0	2.29×10^{-7}	2.44	1.09×10^{3}	14.3
	MSC13 *△	1.0	1.12×10^{-12}	2.0	2.20×10^{-8}	3.80	5.96×10^{3}	20.3
	S10-41△	1.0	2.40×10^{-12}	2.0	1.49×10^{-9}	3.24	2.39×10^{5}	17.5
一指数項表式	ME 17	1.6	5.05×10^{-8}			2.37	8.30×10^{2}	12.3
	ME322	1.8	3.62×10^{-7}			3.75	6.30×10^{2}	11.4
	MF1-20△	1.0	2.02×10^{-12}			4.49	1.19×10^{3}	14.5
	MF2-10*	1.0	2.05×10^{-12}			1.60	6.67×10^{3}	16.7
	MSC 2	1.5	2.13×10^{-8}			2.35	2.75×10^{3}	13.3
	MSC 8	1.3	1.67×10^{-9}			2.77	6.63×10^{3}	14.4
	MSD13 △	1.0	1.80×10^{-12}			3.75	1.26×10^{3}	15.7
	MSD13 *△	1.0	1.28×10^{-12}			4.15	1.62×10^{3}	20.3
	S10-41△	1.0	2.40×10^{-12}			3.04	3.69×10^{3}	17.5

△；p層に不純物濃度勾配を付けたセル

＊；反射防止膜付きセル

表 2.12　コンピュータによる特性解析を行ったセルの出力特性

	J_{sc} (mA/cm²)	V_{oc} (V)	FF	η (%)
ME17	12.2	0.511	0.659	4.11
ME322	11.3	0.479	0.606	3.28
MF1−20 △	14.5	0.586	0.704	5.98
MF2−10＊	16.7	0.590	0.774	7.63
MSC2	13.2	0.517	0.687	4.70
MSC8 △	14.3	0.535	0.672	5.13
MSD13 △	15.6	0.591	0.726	6.69
MSD13 ＊△	20.2	0.607	0.702	8.59
S10−41 △	17.5	0.587	0.740	7.59

△：p 層に不純物濃度勾配を付けたセル

＊：反射防止膜付きセル

2.4.2　短絡電流（J_{sc}）

表 2.12 に示した光電流密度 J_L は短絡電流密度 J_{sc} にほとんど一致している。これは，結晶内部で生成した光電流が接合部で漏洩して R_{sh} を介して流れる量は，外部回路に流れる J_{sc} に比べ無視できるほど小さく，$J_{sc}=J_L$ として，J_{sc} の値そのもので活性層の評価を行ってよいことを意味する。

短絡電流値が小さい原因の一つは，図 2.16 の光電流分布像に示すように，結晶粒界での光生成少数キャリヤの再結合である。結晶粒界での光電流損失に関する定量的取扱いは，昭和 51 年度成果報告書 79 頁に述べた。MF・MSD シリーズは，2～数個の結晶粒からなるため，この損失は無視しうる。0.1～10㎜の結晶粒からなる ME・MSC シリーズにおいてもたかだか数％の損失しかない。したがって，基板からエピ層へ混入する不純物の影響についてのみ検討する。

活性層中の少数キャリヤのライフタイムは 0.2～0.5μs で，こ

の値は単結晶太陽電池の1～数μs の値より小さい。ライフタイムが小さい原因は，活性層中の二次不純物の存在によるためであると考えられる。二次不純物としては，深い準位を形成して少数キャリヤをトラップするものが問題となる。表1.1及び表1.2に示した基板中の不純物のうち，特に多いのはCuとFeでppmレベルで含まれている。これらの不純物は大きな固相拡散係数を有し，AℓやBに比べ拡散が極端に早い。

エピタキシャル層中の不純物は，基板からの固相拡散やオート・ドーピングによって取り込まれる。オート・ドーピングは，不純物が金属塩化物の形で金属Si基板から，一度気相へ放出され，更にエピタキシャル層へ輸送されることによって発生する。この金属塩化物は，成長前のHCℓによる基板の気相エッチングや，成長中の$SiH_2C\ell_2$による基板裏面のエッチングなどによって形成される。金属Si基盤と同時に成長層を形成したダミーの高純度単結晶Si基板セルのJ_{sc}が，別途形成の高純度単結晶Si基板セルのJ_{sc}より常に小さいことから，このオート・ドーピングの重大さは推測される。しかし，更に，金属Si基板セルのJ_{sc}は，ダミーセルのJ_{sc}より常に小さいことは，不純物の固相拡散もまた重大な問題であることを示している。

Groveは，シリコン基板上のエピタキシャル層に対する不純物固相拡散に関し，一般解を与えているが，ここではその結果を利用しFe, Cu, Ti などの場合について若干の計算を行った。このモデルでは，不純物は基板からエピタキシャル層へ固相拡散し，更に，エピタキシャル表面から気相へ拡散（out-diffuse）すると仮定し，このout-diffuseの程度をパラメータ$ht/\sqrt{Dt}$で表わしている。ここでDは固相拡散係数，tは成長時間，hは気相物

質移動係数である。成長温度を1100℃，成長速度2$\mu m/min$，厚さ20μmの場合について，エピタキシャル層中の二次不純物濃度（C_e）の基板中濃度（C_{sub}）に対する比を計算した。表2.13は計算に用いたパラメータを示す。図2.13はFeとTiの場合についての計算結果を基板・エピ層柄面からの距離(x)の関数として表したものである。

表2.13　不純物の固相拡散の計算に用いたパラメータ

- D：拡散定数（at　1100℃）
- t：成長時間（10分）
- V：成長速度（2 $\mu m/min$）

不純物種	D（cm^2／s）	$\sqrt{Dt}$（μm）	$Vt/\sqrt{Dt}$（μm）
Cu	4×10^{-6}	490	0.041
Fe	3×10^{-6}	424	0.047
Mn	4×10^{-7}	155	0.129
Ti	6×10^{-11}	1.90	10.5
Al	2×10^{-12}	0.35	57
B	2×10^{-13}	0.11	182

拡散係数の小さいTiでは，$ht/\sqrt{Dt}$に依存せず，$x=10\mu m$で$C_e/C_{sub}=10^{-4}$となっており，エピタキシャル層中の不純物濃度は基板から遠ざかるに従って急激に減少している。拡散係数の大きいFeは，エピタキシャル表面まで拡散しており$ht/\sqrt{Dt}$に依存し，$C_e/C_{sub}=0.1\sim10^{-3}$である。

また，表2.9に示したように金属Si基板に直接燐を拡散して作製した拡散型セルの特性がエピ型セルの特性に比べ，J_{sc}で0.5

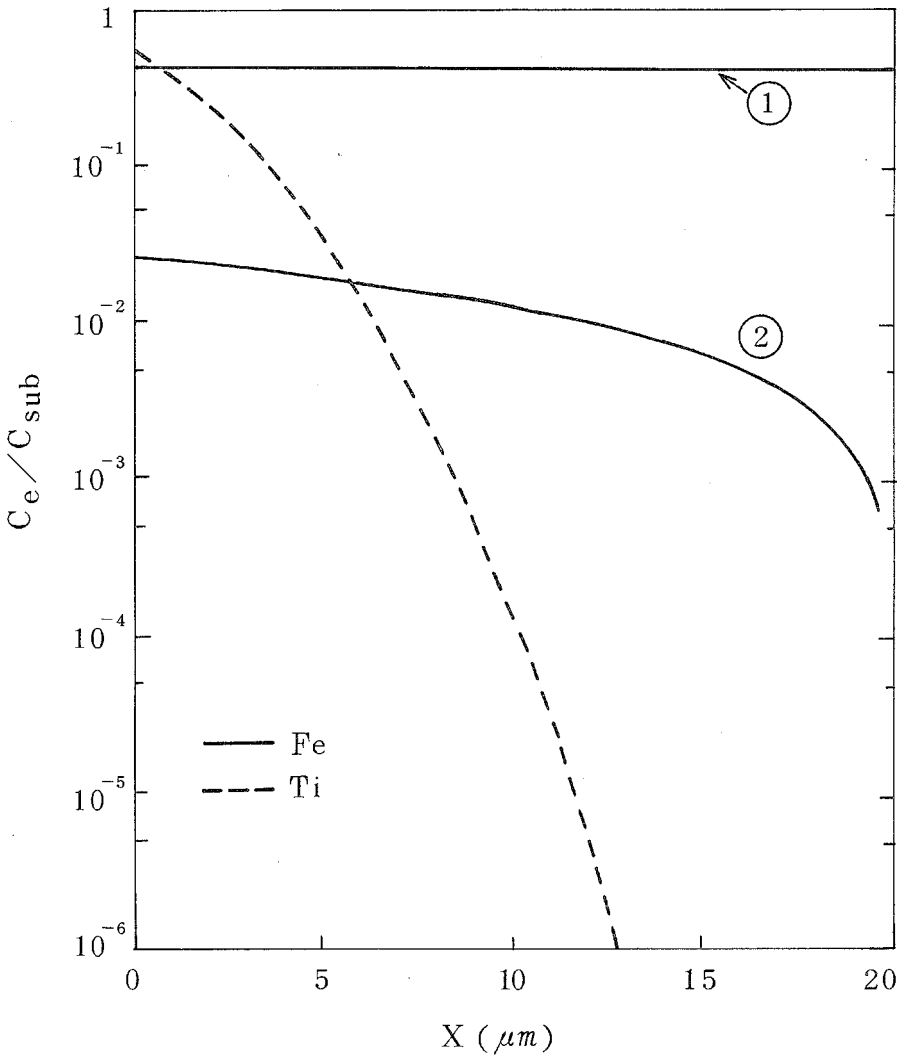

図 2.13　基板からの固体拡散で形成されたエピ層中の不純物濃度分布

x：エピ基板界面からの距離

① $\frac{ht}{\sqrt{Dt}} = 1$　　② $\frac{ht}{\sqrt{Dt}} = \infty$

h：気相質量輸送係数

～0.7程度しかないことは，エピ層の結晶性が基板より改善されていることのほかに，エピ層中の二次不純物濃度が基板よりも減っていることをも示している。拡散型セルのJ_{sc}は，(ME)＜(MSC)＜(MSD)の大小関係を有し，基板中の二次不純物濃度が少いほど大きい値となっている。エピ型セルのJ_{sc}あるいは，

分光感度特性から求めたp層中の少数キャリヤの拡散距離L_nから判断すれば，エピ層中の二次不純物濃度は，基板中濃度と同様に（ME）＞（MSC）＞（MF）＞（MSD）の順に減っていると考えられる。

次に各シリーズのエピ型セルに関し，分光感度から求めた拡散距離と短絡電流の関係を計算値と比較した。計算は，BSF（Back Surface Field）効果を考慮し，n^+層の厚さ$t_n^+ = 0.3\mu m$，$0.5\mu m$，n^+層中の少数キャリヤの拡散距離$L_p = 0.1\mu m$，n^+層とp層のキャリヤ濃度$N_D = 1 \times 10^{20} cm^{-3}$，$N_A = 1 \times 10^{17} cm^{-3}$の条件下で行った。計算結果によれば，短絡電流は$t_n^+ = 0.3\mu m$と$0.5\mu m$で1.5mA/$cm^2$程度の差が見られる。したがって，計算値と実験値の比較をする場合，図2.14のごとく，$t_n^+ = 0.3\mu m$と$t_n^+ = 0.5\mu m$の場合を分けた。黒点は表2.14に示した実測値をプロットしたものであり，実線が計算値である。

表2.14　拡散距離と短絡電流の実測値
（J_{sc}は有効面積で計算した値）

	t_n^+ (μm)	t_p (μm)	L_n (μm)	J_{sc} (mA/cm^2)
MSC9	0.3	30	21	16.0
MSD9		40	31	16.9
ME251	0.5	50	17	12.9
DME25 *			30	16.1
MC44		33	19	14.0
MF1−16			23	15.0

＊　ダミー高純度単結晶Si基板セル

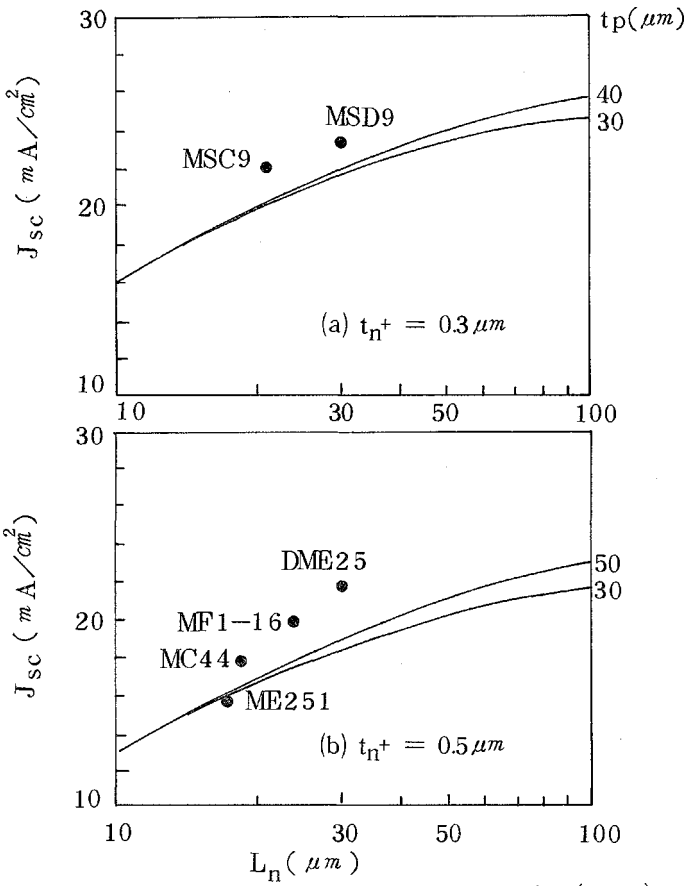

図 2.14　p 層の少数キャリヤの拡散距離（L_n）と短絡電流（J_{sc}）の関係

実線：計算値
- $N_D = 1 \times 10^{20}\ cm^{-3}$
- $L_p = 0.1\ \mu m$
- $N_A = 1 \times 10^{17}\ cm^{-3}$
- 光強度 AM1

黒点：表 2.14 に示した実測値

ME251 以外はいずれのセルにおいても，測定された拡散距離は J_{sc} の計算値から推測される拡散距離に比べ小さい。この原因の一つとして，分光感度特性測定光源の照射光強度（数 10μW/cm²）と J_{sc} 測定時の AM1 の強度（100mW/cm²）の差が考えられる。すなわち，100mW/cm² の光照射下では，二次不純物の形成する深いレベルが光生成キャリヤにより飽和し，少数キャリヤの拡散距離が実効的に長くなっていると推測される。ME251 は結

晶粒界でのJ_{sc}の損失が数％あるために，見かけ上計算値と実測値が一致している。結晶粒内のJ_{sc}はMC44と同程度であった。

2.4.3　開放電圧（V_{oc}）

開放電圧（V_{oc}）は次式で表わせる。

$$V_{oc} = \frac{nkT}{q} \ell n \left(\frac{J_L}{J_0} - \frac{V_{oc}}{J_0 R_{sh}} \right) \qquad (2.15)$$

表2.11の解析値より $I_L R_{sh} > 10\,\text{volt} \gg V_{oc}$ であるから，上式は更に簡単な式となる。

$$V_{oc} = \frac{nkT}{q} \ell n \frac{J_L}{J_0} \qquad (2.16)$$

MSDシリーズは，表2.12に示されているように同じセル構造を有するp^+型－高純度単結晶Si基板セル（S10－41）と同等の開放電圧を有する。したがって，各シリーズの開放電圧の差を考察する。各シリーズのセルの開放電圧の間には，（ME）＜（MSC）＜（MF）＜（MSD）なる大小関係がある。J_Lの各シリーズ間の差はたかだか40％であるが，J_0の差は数倍に及んでいるから，V_{oc}を決めているのはJ_0，（J_{01}，J_{02}）である。特に，ME・MSCシリーズがMF・MSDシリーズより低いV_{oc}を示しているのは，J_{02}の寄与が大きいためである。J_{01}とJ_{02}は，次式で表わされる。

$$J_{01} = q(n_i)^2 \frac{D_n}{L_n N_A} = q(n_i)^2 \frac{D_n}{\sqrt{\tau_n}} \cdot \frac{1}{N_A} \quad (n^+/p\text{構造セル}) \qquad (2.17)$$

$$J_{02} = \frac{qW}{2} \cdot \frac{n_i}{\tau_t} \qquad (2.18)$$

n_i ： 真性不純物濃度　　D_n ： 少数キャリヤ(電子)の拡散定数

N_A ： p層のキャリヤ濃度　L_n ： 少数キャリヤ(電子)の拡散距離

W：空乏層の幅　　τ_n：少数キャリヤ（電子）のライフタイム

τ_t：有効ライフタイム

したがって，J_{01}，J_{02} はｐ層のキャリヤ濃度が同じであるときライフタイムで決まる。すなわち，ME・MSC シリーズの開放電圧（0.48～0.53V）が，MF・MSDシリーズ（0.57～0.60V）に比べ小さいのは，ライフタイムが小さく，J_{02} の寄与が大きいためである。

MF・MSDシリーズの中での各セルのV_{oc}の差（数 mV）を考える場合には，J_Lの差も考慮しなければならない。なぜなら，式（2.16）からJ_L/J_0の２０％の差はV_{oc}に５mV の差を与える。ｐ層のキャリヤ濃度（N_A）が同じであれば，式（2.17）からJ_0はL_nに依存し，J_LもL_nに依存するからV_{oc}をL_n の関係として整理できる。現在は各セルでN_Aが異なり，濃度勾配をつけたりしているため，簡単な比較はできないが，ＭＦシリーズとMSDシリーズの数mV～１０mV の差は表2.14に示した拡散距離の差で説明がつくと考える。

2.4.4　曲線因子（ＦＦ）

曲線因子は等価直列抵抗（R_s），等価並列抵抗（R_{sh}）及びダイオード因子（n）に主として依存する。ダイオード因子の影響の差は，MF・MSDシリーズが，$n_1=1$ でＦＦ＞0.7，ME・MSCシリーズが，n_1 ＝ 1.3～1.8 でＦＦ＜0.7 を示していることに現われている。並列抵抗は１～$6\times10^3\,\Omega\cdot cm^2$ で単結晶セルの $10^4\,\Omega\cdot cm^2$ に比べて小さく，直列抵抗は 1.7～4.6$\Omega\cdot cm^2$ で，理想的なセルの１$\Omega\cdot cm^2$ 以下に比べて大きい。

図 2.15は曲線因子をR_sとR_{sh}の関数として等「曲線因子」線を描いたものである。同図(a)はMSC８，(b)はMSD１３（反射防止

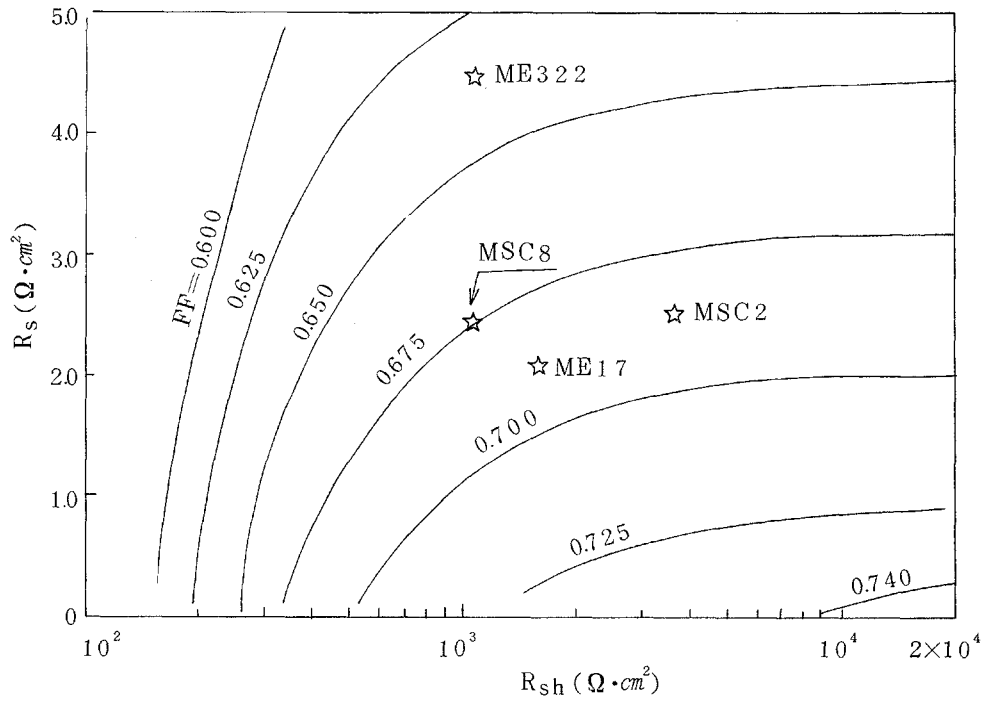

図 2.15 (a)　曲線因子と直列抵抗，並列抵抗の関係

$\left(\begin{array}{l} J_{01}=7.0\times10^{-12}\,A/cm^2\ ,\ J_{02}=2.3\times10^{-7}\,A/cm^2 \\ n_1=1\ ,\ n_2=2.0\ ,\ J_L=14.3\,mA/cm^2 \end{array}\right)$

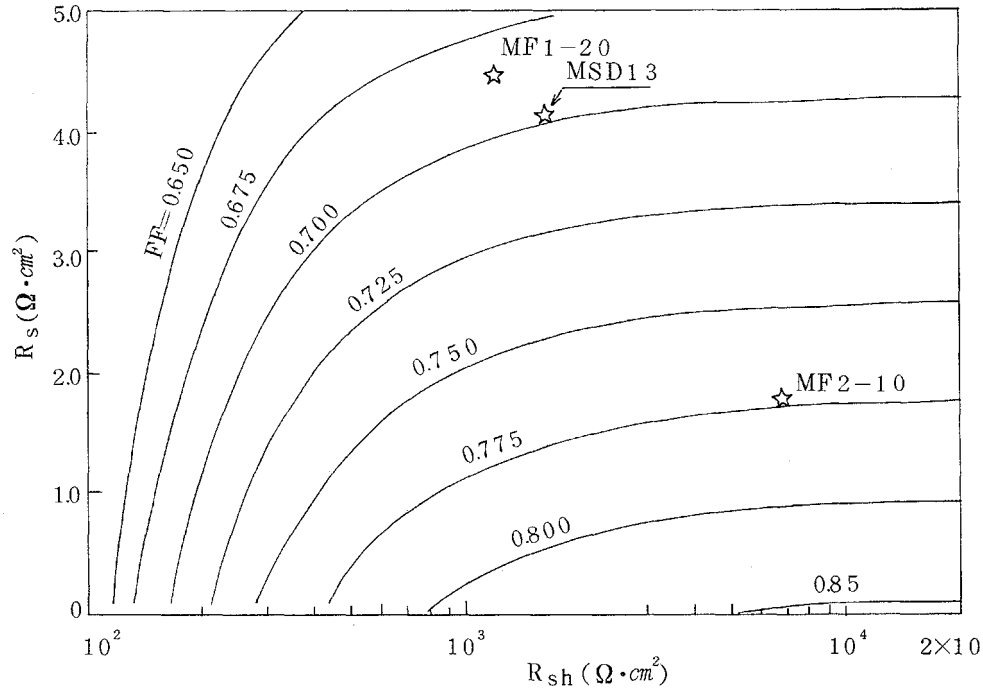

図 2.15 (b)　曲線因子と直列抵抗，並列抵抗の関係

$\left(\begin{array}{l} J_{01}=1.3\times10^{-12}\,A/cm^2,\ J_{02}=0 \\ n_1=1.0\ \ ,\ J_L=20.3\,mA/cm^2 \end{array}\right)$

膜付き）のダイオードパラメータ（J_{01}, J_{02}, n, J_L）を用いて計算した結果である。MSC8とMSD13はそれぞれME・MSCシリーズ，MF・MSDシリーズを代表していると見て，図中のほかのセルのR_S, R_{sh}値もプロットした。両図を比較すれば，ME・MSCシリーズがMF・MSDシリーズより小さな曲線因子を有することがわかる。ME・MSCシリーズでは，R_SとR_{sh}を改善しても0.75を越える曲線因子が得られない。

図2.15(b)からMSD13は，直列抵抗を1Ω・cm^2まで改善するだけで，曲線因子0.775以上（$\eta \geqq 29.5\%$）の達成が可能であり，更にその状態で並列抵抗を10^4 Ω・cm^2まで改善すれば，曲線因子は0.8（$\eta = 9.8\%$）となる。直列抵抗の改善は，電極形状等の検討によって行っていく予定である。

2.5 光起電力分布

2.5.1 多結晶セル

多結晶セル（MEシリーズ）の短絡電流値がダミーとして用いた単結晶セルの約75%に相当した原因を検討するため，前年度に開発したレーザ光走査法により光起電力の面内分布を調べた。

図2.16(a)は金属級シリコンから作製した基板（ME2）上に構成した薄膜セルの光電流分布像である。比較的明るいコントラストを有する領域は光電流が高く，暗い部分は光電流が低く，格子状電極も黒いコントラストを有している。不規則な暗い部分はほぼ結晶粒界に相当し，特に図の下部は微結晶の密集する領域，すなわち粒界密度の高い領域で全体に暗くなっている。図2.16(a)の矢印（A部とB部）で示す間の線走査による光電流分布を図2.16(b), (c)に示す。光電流出力レベルの変動は20%内外である。

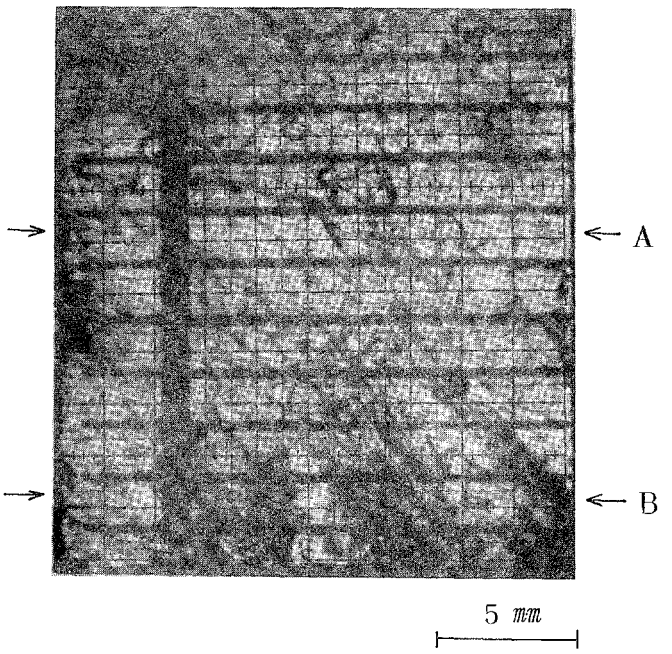

(a) 光電流分布像

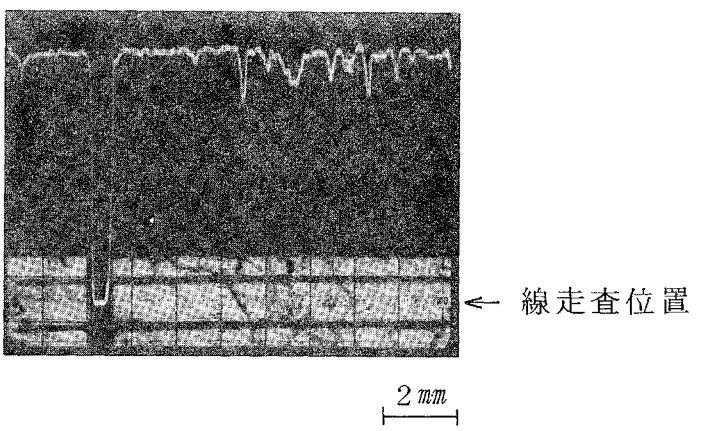

(b) A部の線走査出力

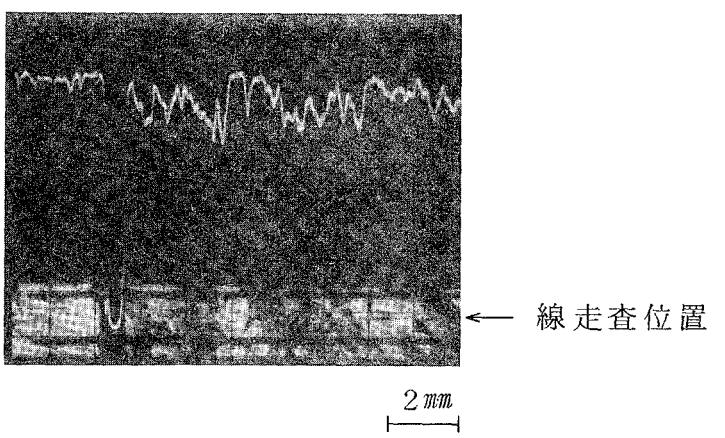

(c) B部の線走査出力

図 2. 1 6　セル表面の光電流分布像及び線走査出力

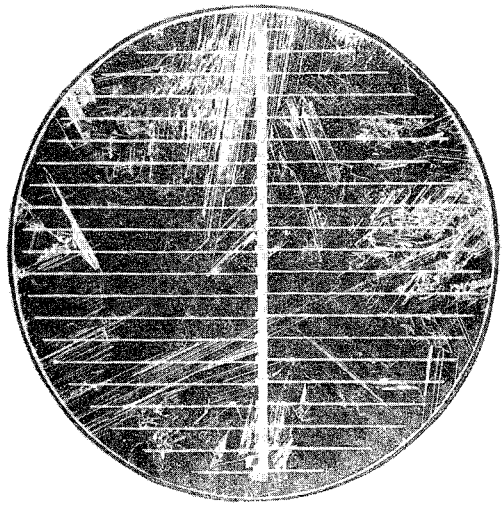

図 2.17(a)　セル表面暗視野像

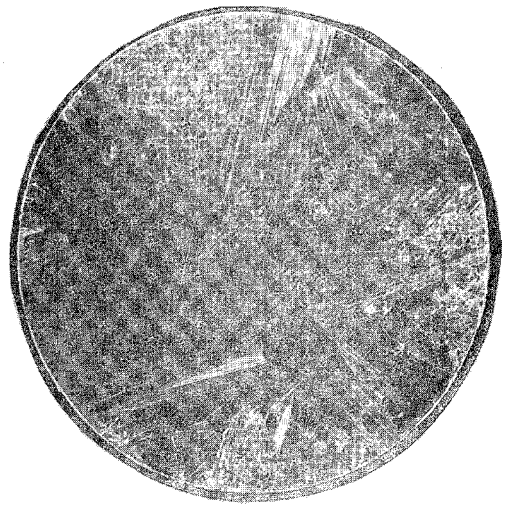

図 2.17(b)　化学エッチ像

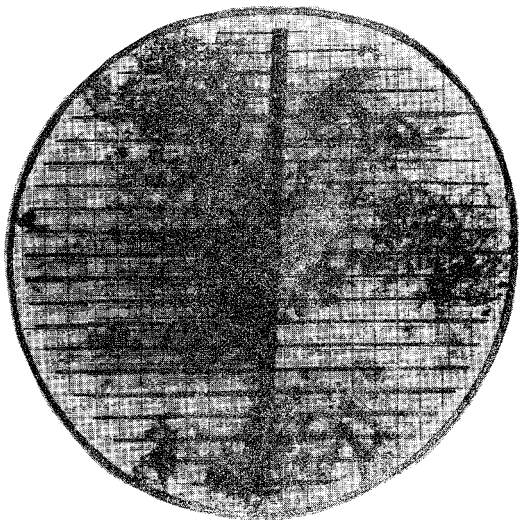

図 2.17(c)　光電流分布像

しかし，精製した金属級シリコンからの結晶成長若しくは再度結晶化した場合，光電流の低下は小さく，光電流値に対する結晶粒界の影響はほとんど無視できる。

また，太陽電池MSA2－9の光起電流分布像，表面写真及び化学エッチング像を図2.17に示す。光電流分布像は表面写真と必らずしも対応しておらず，セル中央部での光電流の落ち込みは，表面写真から予想できない。しかし，エッチング像と光電流分布像の対応は良く，光電流分布像における黒いパターン（光電流の落ち込み箇所）はエッチング像の白いパターン（欠陥箇所）によく対応している。このようにレーザ光走査法により活性層の欠陥を観察することができる。

2.5.2　単結晶セル

図2.18(a)は金属級シリコンから作製した単結晶シリコン(MC)にりん拡散した場合で，円形の光電流分布の存在が特徴的である。この円形パターンは同心円状でなく，渦巻状であり，光電流値の落ち込みは大きい所で約30％で，別の試料では約50％落ち込むものも存在した。レーザ光を線走査した場所の抵抗分布をスプレディング・レジスタンス法で調べた結果，その抵抗分布は図2.18(a)の光起電力分布と対応した。光電流の分布は結晶バルクの少数キャリヤ寿命の分布を示すものであるが，以上の実験結果から，渦巻状分布は多数キャリヤ分布に依存した寿命の分布ではなく深い準位を形成する不純物に起因した寿命分布を示すものと解釈される。不純物としては表4からCu,Fe,Cr,Ti 及びVなどがあるが，いずれも多数キャリヤを形成するAℓとBに比べ，桁違いに偏析係数の小さい元素である。したがって，結晶引上げ中の僅かな成長速度の相違が不純物の偏析に敏感に作用すると予想され，

渦巻状光起電力分布形成の原因となったと考える。

(b)は引上げ単結晶シリコン基板上にp形層とn^+形層を順次エピタキシャル成長させて太陽電池を構成した場合で，もはや(a)のごとき渦巻は観察されず，光電流値は平坦であった。

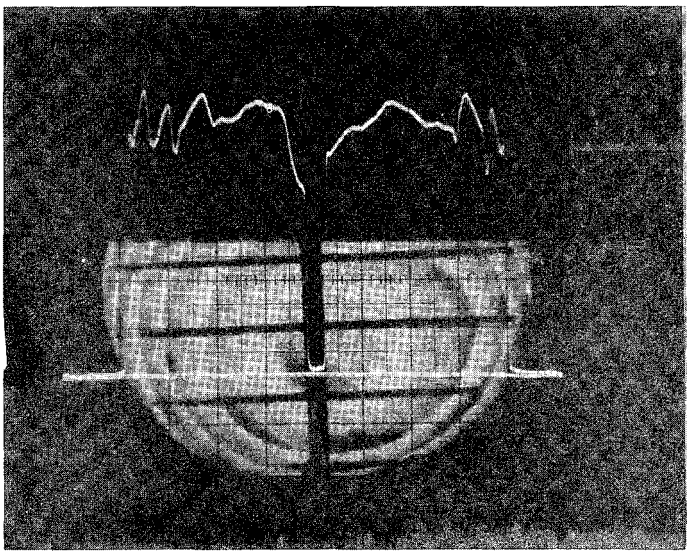

(a) 拡散型（MC46）　　5 mm

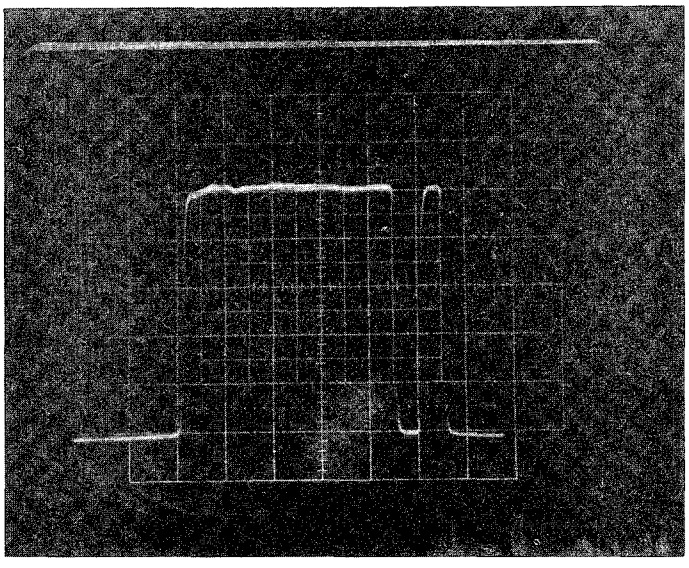

(b) エピ型（MC44）　　5 mm

図 2.18　低純度単結晶セルの光起電力分布

2.6 問題点

(1) セル構成法

基板に用いた金属級シリコンから作製した結晶はそれ自体に接合形式が可能ではあるが，更にシリコン薄膜を気相成長させることにより，基板結晶より優れた光学活性層をうることができる。しかし得られる光学活性層の性質は基板結晶の二次的不純物濃度に依存し，純度の良い基板を用いるほど，太陽電池とした場合の変換効率が高い。これは気相成長の際に基板の一部がエッチングされ，それが再び成長層中に取り込まれるいわゆるオート・ドーピングと，基板から固相拡散により成長層へ侵入する二つの不純物導入の機構があり，現状のプロセスではこれをなくすことはできない。ただし，固相拡散は計算によれば，成長層中の二次的不純物の濃度は，Feを除けばほぼ特性上は問題のない水準と思われ，またFeも濃度から予想されるほど悪影響は観測されない。

しかし，太陽電池の電気的特性を解析した結果では，ME，MSCのシリーズ，すなわち金属級（及び精製した金属級）シリコンから1回結晶化した基板上に形成した太陽電池ではダイオード因子nが1.3～1.8にあり，拡散電流以外の電流成分の寄与が大きいのに対し，2回結晶化した基板（MF，MSD）ではnが1に近く，ほぼ拡散電流成分のみであり，成長層中のキャリヤのライフタイムに大きな差があることがわかった。これは質量分析の分析感度限界に近い水準での二次的不純物濃度に依存しているものと思われる。更に開放電圧に関しても2回にわたる結晶化により，飽和電流値が減少し，再結合電流成分が減少させることができ，0.6Vを超える値をうることができた。

曲線因子については，一回結晶化のME，MSCシリーズでは，

再結合電流成分のため0.7より小さく，並列抵抗，直列抵抗を改善しても0.75より大きな値は得られないと予想されるが，二回結晶化したMF・MSDシリーズでは現在の直列抵抗3～4 Ωcm^2 を1 Ωcm^2 のレベルまで低下させることにより，曲線因子が0.775以上に改善される可能性のあることがわかった。この値は変換効率で9.5％以上に相当するが，今年度の電極形成に関する検討を更に進めて，電極構造等を総合的に検討することにより，薄膜シリコン太陽電池で10％に近い変換効率をうることも可能であるとの見通しは得られた。

(2) 薄膜シリコンセルと基板

シリコン薄膜方式の太陽電池では，特性の維持を図りつつ，安価な基板上に良好な性質の半導体薄膜を形成させることが，価格低減のポイントである。これまで種々の材料を基板としてセル構成の可能性について検討してきたが，その中で現在明らかになっていることは，

① 単純な気相成長で得られる薄膜は粒径の小さな多結晶からなり，そのために1％前後の変換効率しか得られない。変換効率を実用の水準とするためには粒径の大きなシリコン結晶にエピタキシャル条件で薄膜を成長させる必要がある。

② エピタキシャルには1000℃程度の高温が必要であり，したがって，基板として成長する薄膜と物理的・化学的整合性とが要求される。このため，成長する薄膜中に取り込まれ光電変換特性を劣化させるような不純物が多量に含まれることは望ましくない。

ことなどである。今年度は主として金属級シリコンを検討してきたが，純度の点を除けば上記の要件を満たしており，基板の材料

としては最も優れている。しかし，有害な不純物をどの様なプロセスでどの程度除去すれば薄膜太陽電池の基板として技術的，あるいは経済的に使用可能となるかの問題が残された。

シリコンの特徴は，結晶化の段階で偏析効果により有害不純物がかなり除去されるので，結晶化のプロセスを繰り返せば究極的には高純度シリコンが得られると思われる。しかし，1～2回の結晶化で市販の（すなわち硅石から還元しただけの）金属級シリコンからどの程度の材料が得られ，また薄膜太陽電池としてどの程度の変換効率をうることができるかが経済的にこのアプローチが可能かどうかを判断する重要な情報と言える。結果は前述のとおりで，単純に結晶化した基板上に薄膜形成を行った場合6％弱2回の結晶化を行った場合は8％弱の変換効率が得られた。更に市販の金属シリコンで溶融状態から固化する際に，シリコン結晶間に析出する不純物相を除去した精製金属シリコンを材料とした場合には，1回の結晶化で7％，2回の結晶化で9％弱の変換効率が得られることがわかった。

現在市販されている金属シリコンは鉄あるいはアルミニウムとの合金用途を目的としたものであり，太陽電池用基板材料としての配慮を加える余地がある。ただし，これは現行のプロセスに変更を加えるものであり，その技術的，経済的評価は別に検討されなければならないと考える。今年度得られた精製金属シリコンの2回結晶化による結晶と同程度あるいはそれよりも若干純度の良い（直接拡散によって5％の変換効率が得られる程度の）結晶シリコンが安価な精製プロセスで得られるならば，本方式による薄膜太陽電池も実用的なレベルに到達できると考えられる。

Ⅲ．今後の研究開発計画

前年度までの４年間の研究開発の結果，薄膜多結晶方式のシリコン太陽電池は，セル面積１０～２０cm^2において，変換効率７～８％の値を得技術的にほぼ実用可能と判断できる段階に達した。

５３年度は，前年度までの成果を総合して薄膜多結晶太陽電池の特性改良のため，下記の２点につき研究開発を進める。

(1)　セル面積拡大の基礎的研究

セル特性均一化の検討を行うと共に，セル面積拡大の基礎技術の予備開発を行う。

(2)　セル変換特性向上の研究

不純物効果についての知見を実際のセル製作技術の中に採り入れ効率向上を図ると共に，特性解析技術を改善し，不完全接合の特性解析を行って効率低下の原因を検討する。また，特性解析のルーチン化を図って製造プロセス技術への早期フィードバックを行い，最適化を図る。

上記研究に附随して，薄膜多結晶方式を含む多結晶方式についてのコストを把握し，技術面のみならずコスト面からも大量製造が可能な方式の検討を行う。

以上のセル技術の開発に伴って，今後セル面積の拡大，プロセスコストの低減，アレー化技術の開発，信頼性，フィールドデータの蓄積などの周辺技術開発が必要となってくる。この目的のため，５４年度にはセルの高効率化，プロセスコストの低減，アレー化技術の開発，５５年度にはある規模（数10W程度）でのセル，アレーの試作を行いつつフィールドデータの蓄積を図ると共に，セルの大型化と低コストプロセスの技術開発を行うことを予定している。

Ⅳ 参　　考

Reprinted from JOURNAL OF THE ELECTROCHEMICAL SOCIETY
Vol. 123, No. 3, March 1976
Printed in U.S.A.

Growth and Structure of Polycrystalline Indium Phosphide Layers on Molybdenum Sheets

Tadashi Saitoh, Sunao Matsubara, and Shigekazu Minagawa*

Central Research Laboratory, Hitachi, Limited, Kokubunji, Tokyo, Japan

ABSTRACT

Pinholeless polycrystalline indium phosphide layers were grown on molybdenum sheets at temperatures lower than 600°C using indium and phosphorus trichloride as the source materials. The low activation energy of the deposition rates and weak dependence of the rates on the partial pressure of indium monochloride suggest that surface processes play an important role in the growth of polycrystalline films. It was ascertained by an x-ray diffraction measurement that the {110} and {331} orientations become noticeable with increasing thickness at higher temperatures, whereas the <111> orientation is dominant at lower growth temperatures. The development of the <110> orientation produces films with a columnar structure, which could be explained by the dependence of the growth rate on the crystallographic orientation.

Indium phosphide is a promising material for solar cells because the indium phosphide cell has high theoretical conversion efficiency (1). In order to obtain low-cost solar cells for terrestrial use, it is necessary to fabricate thin-film solar cells of polycrystalline indium phosphide on low-cost substrate materials.

To date, few papers have been published on the preparation of polycrystalline indium phosphide, although research on the epitaxial growth had been carried out (2-4). In this paper, polycrystalline layers were de-

* Electrochemical Society Active Member.
Key words: deposition rates, grain size, orientation.

posited on thin molybdenum sheets by the reaction of indium with phosphorus trichloride in a hydrogen atmosphere. The indium transport reaction and the process for the deposition of pinhole-free indium phosphide were examined. The rate-determining step of the deposition is discussed. The grain size of the deposited film, which is generally required to be larger than the minority-carrier diffusion length, was measured as a function of deposition conditions since highly oriented polycrystalline films may be essential to realize efficient solar cells (5, 6). The orientation of the polycrystalline films was characterized by the x-ray method and reflection electron micrography.

Experimental

Film growth.—Polycrystalline indium phosphide was deposited on 50 μm thick molybdenum sheets by reaction of In and PCl_3 in hydrogen. The molybdenum sheets were selected because of the small thermal expansion coefficient mismatch between molybdenum and indium phosphide and because of its chemical stability in a growth atmosphere. Prior to growth, the sheets were ultrasonically cleaned in trichloroethylene and subsequently in methanol, and chemically etched in a 1 H_2SO_4-1 HNO_3-3 H_2O solution.

The deposition was carried out in a horizontal reactor with a conventional gas feed system (2, 3), typical for an epitaxial growth of III-V semiconducting materials. The temperature of the indium source was held at 750°C and the temperature of the molybdenum sheets was in the range of 450°-650°C. A typical flow rate of the hydrogen gas was 200 cm^3/min (at room temperature). The partial pressure of PCl_3 in the feed gas was 2-13 $\times$ 10^{-3} atm. The thickness of the deposited layers was determined by measuring the surface line profiles of step-etched samples.

Structure.—Measured x-ray intensities (CuK_α radiation) were normalized by the theoretical values calculated by the following equation (7)

$$I = C \cdot M \cdot P \cdot L \cdot |F|^2 \cdot A \cdot T \qquad [1]$$

where C is a constant, M the multiplicity of the planes, P the polarization factor, L the Lorentz factor, F the structure factor, A the absorption factor, and T the temperature factor. For powder samples with a platelike shape, the absorption factor is described as (7)

$$A = A_0\left\{1 - \exp\left(-\frac{2\mu t}{\sin\theta}\right)\right\} \qquad [2]$$

where A_0 is a constant, μ the linear absorption coefficient, t the thickness, and θ the x-ray diffraction angle. A is almost equal to A_0 if the thickness, t, of indium phosphide is more than 20 μm. The equations used to calculate other factors are those found in Guinier's book (7).

Results and Discussions

Transport of indium.—A source temperature of 750°C was adopted in this experiment because a transport efficiency defined below was reported to saturate and approach an equilibrium value at temperatures higher than 700°C (8). First, the amount of indium consumed during the reaction was measured as a function of the reaction time at a linear flow rate of 0.75 cm/sec, calculated at 750°C. The amount was found to increase in proportion to the reaction time at PCl_3 partial pressures of 2.3 $\times$ 10^{-3}-1.2 $\times$ 10^{-2} atm. As for the effect of the PCl_3 partial pressures in the feed gas, the transport rate of indium increased in proportion to the PCl_3 partial pressure as indicated in Fig. 1.

The transport efficiency, defined by the ratio of the number of moles of indium transported to the number of moles of chlorine fed during the growth time, was 95%. This is in good agreement with the 99% obtained by thermodynamic calculation and an observed value reported for the same reaction in a vertical reactor (4). The result shows that the transport reaction around the source occurs under equilibrium conditions.

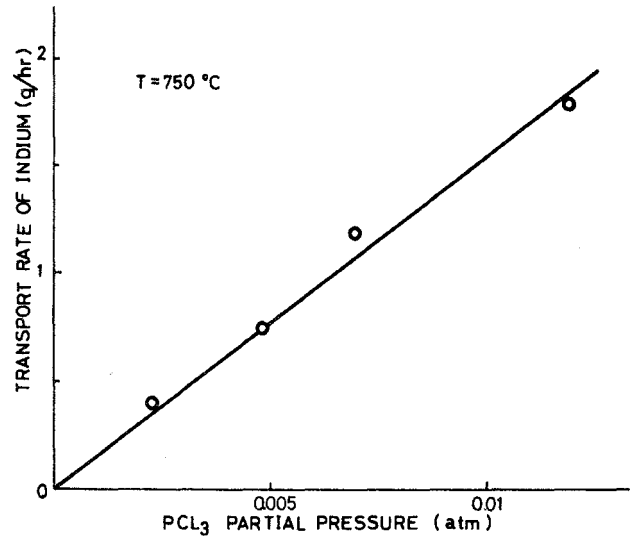

Fig. 1. Transport rate of indium as a function of PCl_3 partial pressure. The temperature of the indium source is 750°C.

Deposition of indium phosphide.—The deposition of polycrystalline indium phosphide was carried out at temperatures lower than 650°C which had been used previously for epitaxial growth on single crystal substrates (2-4). In a film deposited at 650°C, there existed small holes where molybdenum surfaces could be seen, although the grain size was larger than that in a film prepared at lower temperatures. Temperatures lower than 600°C were found to be useful to obtain homogeneous films without pinholes. This suggests that sufficient supersaturation is necessary for uniform polycrystalline growth.

The thicknesses of the polycrystalline deposits were found to increase in proportion to the deposition time except in the initial stage of the deposition. From an Arrhenius plot of the deposition rates shown in Fig. 2, the activation energy was determined to be 15 kcal/mole. This agrees approximately with the activation energies of epitaxial growth on low-index planes (4).

Mass spectroscopic analysis (8) of gases in the deposition zone has shown that indium monochloride reacts with phosphorus compounds according to the reaction

$$InCl(g) + P^*(g) + \frac{1}{2}H_2(g) = InP(s) + HCl(g) \qquad [3]$$

where P* represents P_2 and P_4. Assuming that the

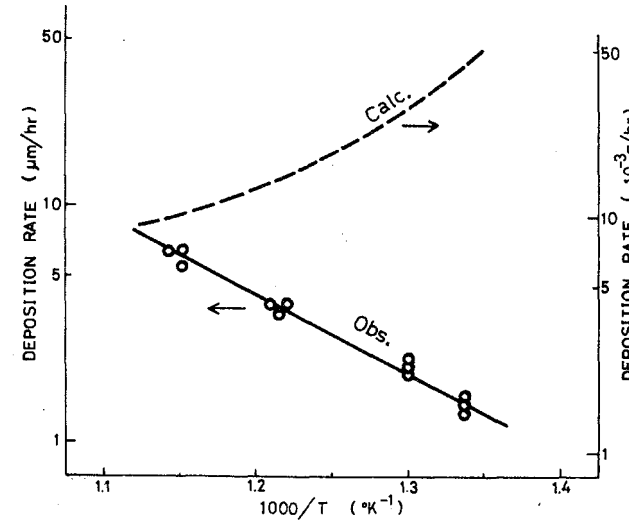

Fig. 2. Arrhenius plot of deposition rate for polycrystalline indium phosphide. The dashed line is calculated under thermodynamic equilibrium. The PCl_3 partial pressure is 7.2 $\times$ 10^{-3} atm.

phosphorus compound in the gas phase is the tetramer, deposition rates were calculated using the above equation. As indicated by the dashed line in Fig. 2, differences were observed on the Arrhenius plots between calculated and observed values. This result shows that the deposition reaction cannot be described as being carried out under thermodynamic equilibrium.

The deposition rate was examined as a function of the PCl_3 partial pressure which corresponds to one-third of the InCl partial pressure appearing in Eq. [3]. The rate increases only slightly with increasing PCl_3 partial pressure as shown in Fig. 3.

The weak dependence of the deposition rate on the partial pressure suggests that the deposition process is not limited by mass transfer of reactants in a gas phase but by surface processes such as surface reaction, surface diffusion, adsorption and desorption processes.

Grain size.—The grain size of the polycrystalline indium phosphide layers tends to increase both with increasing deposition temperature and thickness; moreover, the grain size is not always homogeneous. In the case of a layer deposited at 600°C, the mean value of the grain size measured by the Fullman method (9) was about 7 μm (about 1 μm in a film deposited at 500°C). Roughness of the surface was about 2 μm for a 12 μm thick film deposited at 600°C.

The mean grain size increased and saturated with increasing film thickness as shown in Fig. 4. This tendency is related to the observation that small nuclei on a molybdenum surface grow in size and finally coalesce with each other.

A columnar structure in a cross section of the film shown in Fig. 5 suggests the saturation of the grain size. The columnar structure indicates that each grain grows mostly perpendicular to the substrate. The columns were found to develop with increasing growth temperature and thickness, which relates to the development of preferred orientation as mentioned below. However, the columns were found not to grow immediately from the substrate and not to exist in layers deposited at temperatures lower than about 500°C.

Preferred orientation.—X-ray diffraction spectra of InP films consisted primarily of diffraction peaks of low-index faces such as {111}, {110}, {311}, and {331}. Also, relative intensities of the diffracted peaks were found to vary with the growth temperature and the thickness of the film. For a film deposited at 600°C, {110} and {331} faces developed, whereas {111} and {311} planes diminished with the thicknesses for films thicker than 5 μm as shown in Fig. 6. On the other hand, layers thinner than 5 μm were random in orientation. As for a film deposited at 500°C, the diffracted intensities decreased in the order of {111} > {220} > {311} > {331} ≧ {200} and the tendency held for films varying in thickness. However, the degree of preferred orientation was not found strong.

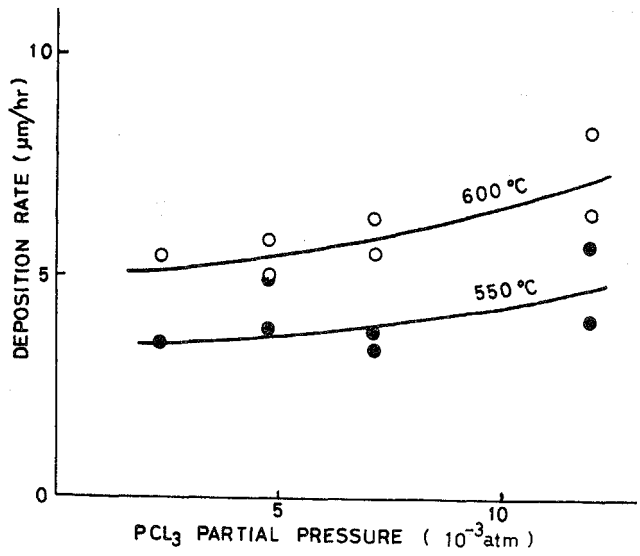

Fig. 3. The effect of PCl_3 partial pressure in the feed gas on the deposition rate of polycrystalline layers.

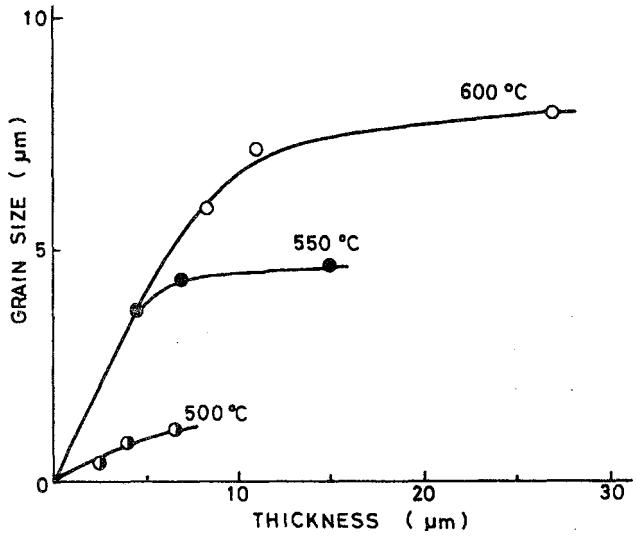

Fig. 4. The variation of grain size with thickness at various substrate temperatures.

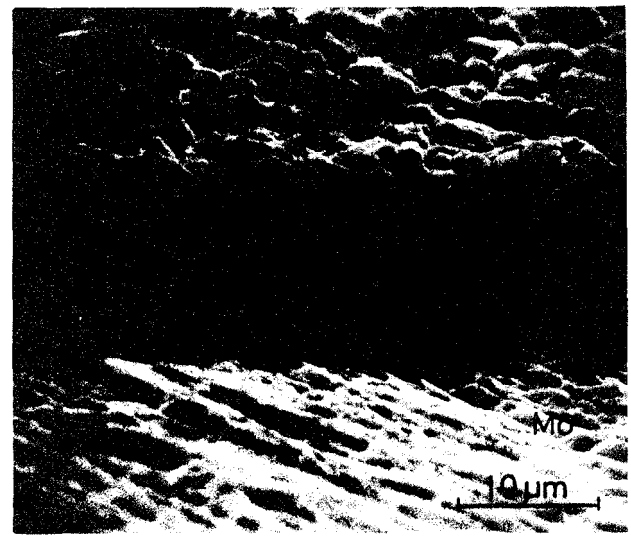

Fig. 5. Scanning electron micrograph of InP polycrystalline deposit on molybdenum.

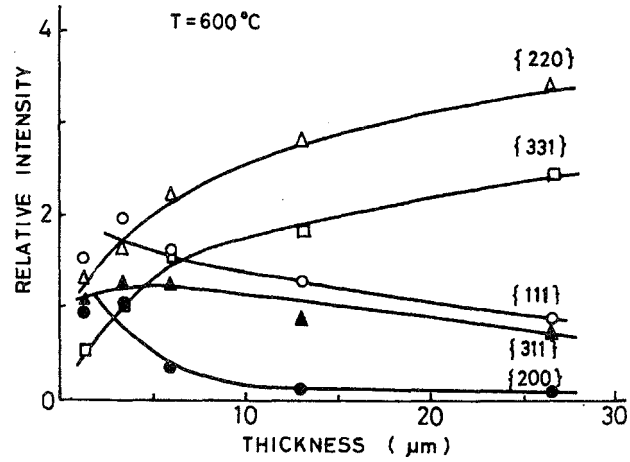

Fig. 6. The variation of relative intensity of x-ray diffraction with thickness for various crystal planes in the films deposited at 600°C.

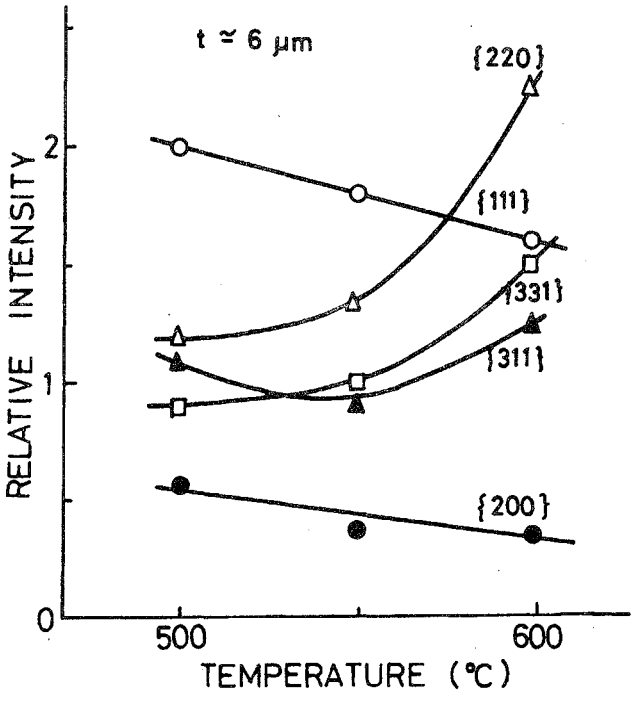

Fig. 7. The variation of relative diffracted intensity with deposition temperature for various crystal planes in the films with thickness of about 6 μm.

Next, we examined the effect of growth temperature on the orientation of the films. In the case of thin films (about 1 μm), relatively random orientation was obtained irrespective of various growth temperatures, although {111} orientation developed to some extent. For the thicker film (6 μm) shown in Fig. 7, {110} and {331} planes developed, {111} and {100} planes diminished, and the {311} plane did not change with increasing growth temperatures. The inverse tendency between the {110} and {111} orientations for increasing temperature is also similar to the result obtained for polycrystalline silicon films prepared by pyrolysis of silane on an oxidized silicon surface (10).

In order to examine the effect of the partial pressure of reactants on the orientation, the partial pressure of PCl_3 was varied from 2×10^{-3} to 1×10^{-2} atm. However, no effect in preferred orientation was observed.

In the x-ray method, the information is obtained over an x-ray penetration depth of tens of microns, while reflection electron microscopy provides information on the degree of preferred orientation with less than a micron of the crystal surface. The reflection electron micrographs of the film deposited at 600°C showed random spots. This indicates that the surface consists of relatively large grains with random orientation. As the {220} intensity was dominant in the x-ray diffraction, the crystallites are oriented in the <110> growth direction, but have randomly oriented surfaces.

On the other hand, for films grown at temperatures less than 550°C, the electron micrographs consisted of Debye rings. And the micrographs showed that among the various planes, the {111} plane was relatively parallel to the substrate surface, but the {110} face was inclined or random in the orientation. Especially, the orientation of the {111} face is consistent with that obtained by x-ray diffraction. This indicates that the orientation near the surface is equal to that in the film.

The <110> preferred orientation of InP films prepared at 600°C is in agreement with that of polycrystalline silicon films (10). The {110} face was reported to be the plane with the fastest growth rate among low index planes for InP (4) and Si (11). In addition, for an epitaxial growth of indium phosphide, the growth rate was in the order of {110} > {111}B > {100} surfaces (4), corresponding to the order of the orientation. Therefore, in the polycrystalline growth of InP, the planes with higher growth rates grow preferentially and, thus, other planes cannot grow in the direction parallel to the substrate surface. As a result, the preferred orientation is formed for the planes with higher growth rates.

Conclusions

Polycrystalline indium phosphide was deposited on molybdenum substrates by vapor-phase growth to investigate the growth mechanism and the structure of the film. The conclusions obtained are as follows:

1. The indium transport reaction with phosphorus trichloride occurs under thermodynamic equilibrium.
2. Homogeneous polycrystalline films are obtained at temperatures lower than 600°C. The activation energy of 15 kcal/mole and the dependence of the deposition rate on the partial pressure of the reactant suggests that surface processes determine the deposition rate.
3. The grain size depends on the deposition temperature but is independent of the partial pressure of PCl_3 in the feed gas.
4. The crystal grains are oriented in the direction of {111} at low temperatures, but the {110} orientation and orientations near the <110> directions developed at higher temperatures and with increasing the thickness.

Acknowledgments

The authors wish to thank R. Takahashi for his advice on the vapor deposition and K. Ohbuchi for performing the x-ray diffraction experiments. The authors are also grateful to Dr. E. Maruyama for his critical reading of this manuscript and Drs. Y. Otomo and T. Tokuyama for their encouragement.

Manuscript submitted Sept. 22, 1975; revised manuscript received Nov. 4, 1975.

Any discussion of this paper will appear in a Discussion Section to be published in the December 1976 JOURNAL. All discussions for the December 1976 Discussion Section should be submitted by Aug. 1, 1976.

Publication costs of this article were partially assisted by Hitachi, Limited.

REFERENCES

1. J. J. Wysocki and P. Rappaport, *J. Appl. Phys.*, **31**, 571 (1960).
2. H. Seki and M. Kinoshita, *Japan. J. Appl. Phys.*, **8**, 1142 (1968).
3. M. C. Hales, J. R. Knight, and C. W. Wilkins, Proc. 3rd Int. Symp. on Gallium Arsenide, p. 50 (1970).
4. O. Mizuno, *Japan. J. Appl. Phys.*, **14**, 451 (1975).
5. F. A. Shirland, *Advanced Energy Conversion*, **6**, 201 (1966).
6. P. H. Fang and L. Ephrath, *Appl. Phys. Letters*, **25**, 523 (1974).
7. A. Guinier, "X-ray Crystallographic Technology," Hilger and Watts Ltd., London (1952).
8. V. S. Ban and M. Ettenberg, *J. Phys. Chem. Solids*, **34**, 1119 (1973).
9. R. L. Fullman, *J. Metals*, March, 447 (1953).
10. T. I. Kamins and T. R. Cass, *Thin Solid Films*, **16**, 147 (1973).
11. S. K. Tung, *This Journal*, **112**, 436 (1965).

Proceedings of the 8th Conference (1976 International) on Solid State Devices, Tokyo, 1976;
Japanese Journal of Applied Physics, Volume 16 (1977) Supplement 16-1, pp. 413–416

Dendritic Growth of Silicon Thin Films on Alumina Ceramic and Their Application to Solar Cells

Tadashi SAITOH, Terunori WARABISAKO, Haruo ITOH,
Nobuo NAKAMURA, Hiroshi TAMURA, Shigekazu MINAGAWA
and Takashi TOKUYAMA

Central Research Laboratory, Hitachi Ltd.,
Kokubunji-shi, Tokyo 185, Japan

Polycrystalline silicon films on alumina ceramic are recrystallized under normal freezing conditions. A multi-layered structure containing borosilicate glass and titanium layers is successfully used to prevent molten silicon films from agglomeration. The films obtained are dendritic and of mm size. Chemical etching reveals tilt boundaries, linear and dot-like defects in addition to grain boundaries.

The thin film solar cells fabricated on the recrystallized silicon by successive deposition of p and n^+ layers show photovoltaic conversion efficiencies of up to 2.6% at a fill factor of 0.67 under an AM1 simulator. From the spectral response curves of the cells, the electron diffusion length of the p-type active layers is calculated to be 1 μm and causes a low short circuit current density of 9.8 mA/cm^2.

§1. Introduction

Polycrystalline silicon films deposited on inexpensive substrates have been attempted to fabricate low-cost solar cells.[1,2] Our approach concerns a fabrication of silicon thin film solar cells on alumina ceramic substrates having generally compatible physical properties with silicon and being inexpensive for wide application in thick-film electron devices.

The grain size of polycrystalline silicon on alumina, prepared by a conventional chemical vapor deposition technique, was usually less than 10 μm. Several efforts to enlarge the grain size of thin films through recrystallization or sintering of the deposited films have been reported.[3,4] Doo reported that a recrystallized silicon film of mm grain size has been obtained on alumina ceramic by employing a melting and rapid solidification technique.[5]

In this paper, a new melt-regrowth technique is described which is designed to prevent molten silicon film agglomeration, as well as to obtain a grain size around 1 mm. The structural and electrical properties of the recrystallized films are also investigated. In addition, the characteristics of thin film solar cells fabricated on the silicon films are discussed.

§2. Experimental

The substrate used was 96% pure alumina ceramic, $25 \times 25 \times 1$ mm^3 in size. A titanium film (about 0.2 μm thick) was evaporated on the alumina substrates in a vacuum. For the deposition of silicon films with a thickness of 20 to 30 μm, trichlorosilane was used as a source and diborane was added as a p-type dopant. and then, a borosilicate glass film (1 to 2 μm thick) was chemically deposited on the silicon film.

The polycrystalline silicon film thus prepared was melted and recrystallized in air ambient under normal freezing conditions. The structural properties of the recrystallized film were investigated using X-ray diffraction and Sirtl etching. To fabricate a p-n junction on the recrystallized layer, a p- and an n^+-type layer were chemically deposited, successively. The electrical contact on the n^+-type layer was attached by evaporating titanium and silver successively through a metal mask. The aluminum contact was evaporated on the p^+-type region revealed by mesa-etching. The solar cell characteristics were measured under illumination by an AM1 solar simulator. Spectral response curves were obtained using a constant energy spectrometer. Furthermore, local variations of photocurrents were examined using a scanning He–Ne laser beam with a resolution of about 5 μm.

§3. Results and Discussion

3.1 *Recrystallization*

To suppress the agglomeration of the molten silicon film during melt and regrowth, a thin film of appropriate material was placed on silicon. For various oxide and nitride films deposited chemically on the silicon films, a borosilicate glass film was found to be most suitable. It is suitable because the film with a 10 mole% of B_2O_3 melts at 1390°C and works as a liquid encapsulant on the silicon film at the regrowth temperatures. However, only the use of borosilicate glass film was not sufficient to prevent agglomeration. A titanium layer inserted between the silicon and alumina was found to be very effective. This is probably due to the decrease of the melt-substrate interfacial energy or the improvement of the wettability of the molten silicon to the substrate.

The effect of ambient gases in the recrystallization was also examined. In the case of nitrogen or argon gases, the oxide film was vaporized and the molten silicon film agglomerated. On the other hand, the oxide film did not vaporize in either oxygen or air ambients, in which the oxygen partial pressure was higher than the equilibrium dissociation pressure of the silicon oxide.

A typical surface pattern of a recrystallized film (20 μm thick) is shown in Fig. 1. Dendritic growth of about 0.3 mm wide and a few centimeter long can be seen over the entire surface. The X-ray diffraction for the dendritic films showed the [111] orientation to be more predominant than the [110]. The latter orientation is typical for the as-deposited films. This result could be explained by the fact that the surface energy of the [111] face is lower than that of the [110][6] and the surface index with the lower surface energy determines the preferred orientation.

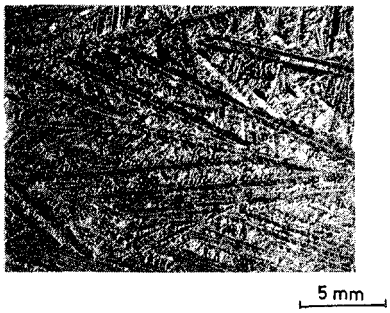

Fig. 1. Dendritic silicon film, 20 μm thick, on alumina ceramic, recrystallized by a normal freezing technique.

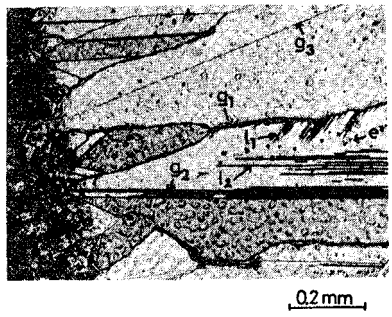

Fig. 2. Chemically etched surface of a recrystallized silicon film using a diluted Sirtl etchant.

Figure 2 shows the enlarged areas of the recrystallized and unmelted regions. The unmelted region is indicated at the left-hand side of the figure. The regrowth begins from the periphery of the unmelted regions and proceeds to the right in the figure during cooling down of the furnace. Also shown in Fig. 2 are various types of defects revealed by Sirtl etching. Among them were grain boundaries with irregular shapes g_1, tilt boundaries g_2 or g_3, triangular etch pits e and linear defects l_1 or l_2. Tilt boundaries were determined by the observation that the boundaries extend straight from grain boundary to grain boundary in the direction of [211] and are parallel to the bases of the triangular etch pits. The linear defects originating from the irregular grain boundaries and terminating in the grains are probably due to stacking faults and slip lines.

Hall measurement indicated that the resistivity of the recrystallized films was 1×10^{-3} $\Omega \cdot$cm, being half of that for the as-deposited films. However, the mobility was 40 $cm^2V^{-1}s^{-1}$ being twice as large as the value of as-deposited films.

3.2 *Dark current-voltage characteristics*

The "n" value in the ln I vs. V relation is calculated to be 1.6 from the forward current-voltage characteristics for an efficient solar cell as shown in Fig. 3. Generally, the "n" value tended to be less than two for efficient solar cells and more than two for less efficient cells. The reverse characteristics also shown in Fig. 3 were plotted in a log-log relationship. As a

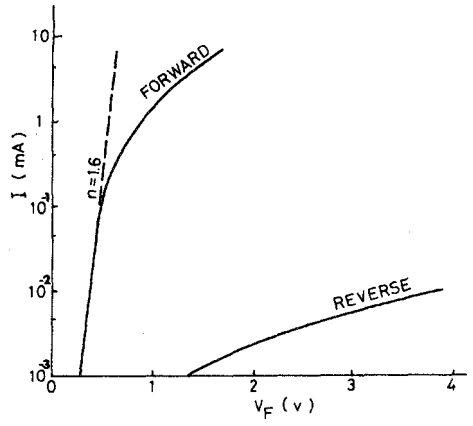

Fig. 3. Dark current-voltage characteristics of a thin film solar cell fabricated on alumina ceramic. The cell area is 3.08 mm².

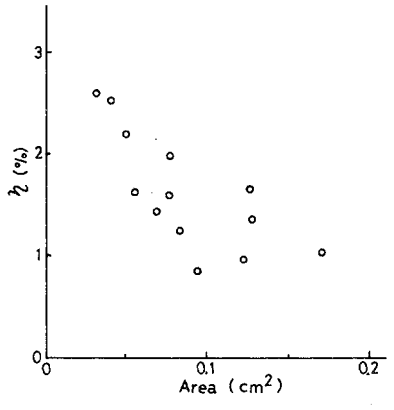

Fig. 5. Variations in photovoltaic conversion efficiency with cell area for thin film solar cells on alumina.

result, it was found that the current increased quadraticly with the voltage and indicated that the space-charge-limited current is dominant.[7] On the other hand, the current-voltage characteristics of less efficient cells were almost all ohmic, corresponding to a shunt resistance of several kΩ.

3.3 *Solar cell characteristics*

The current-voltage characteristics for an efficient cell under illumination are shown in Fig. 4. The optimum short-circuit current density, open-circuit voltage, fill factor and conversion efficiency were 9.8 mA/cm², 0.40 V, 0.67 and 2.6%, respectively.

To examine local distribution of the conversion efficiencies, mesa-etched diodes of various sizes were fabricated on the same substrate and cell characteristics were compared. The conversion efficiencies tended to decrease as cell area increased as shown in Fig. 5. Among the factors influencing efficiency, the fill factor was found to decrease with increasing cell area due to a decrease of the shunt resistance.

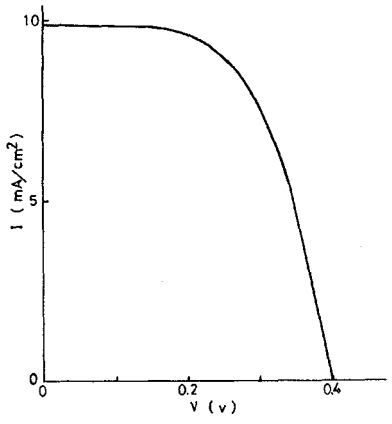

Fig. 4. Current-voltage characteristics of a thin film solar cell on alumina ceramic under an AMI simulated solar irradiation.

In order to determine the reason for low short-circuit current, the spectral response curve was measured. The photocurrent at longer wavelengths for the thin film cell was found to be lower than that of a single crystal cell. This suggests that the diffusion length of minority carriers is short. The diffusion length was determined using the following equation:[8]

$$I \propto \frac{\alpha \cdot L_n}{1+\alpha \cdot L_n} \exp(-\alpha \cdot d),$$

where I is the short-circuit current, α the absorption coefficient, L_n the electron diffusion length and d the n^+-type layer thickness. The electron diffusion length of the p-type layers was calculated to be about 1 μm.

The low value for the diffusion length is considered attributable to the presence of defects and/or deep level impurities. The local variation of the photocurrent was examined by measuring a laser beam induced current. Shown in Fig. 6(a) and (b) are a reflection laser image and a laser beam induced current image. Typical defects in Fig. 6(a) are irregular boundaries A and linear boundaries B_1 and B_2 corresponding to g_1 and g_2 in Fig. 2, respectively. From Fig. 6(b), the photocurrent at the linear boundary B_1 is found to be slightly

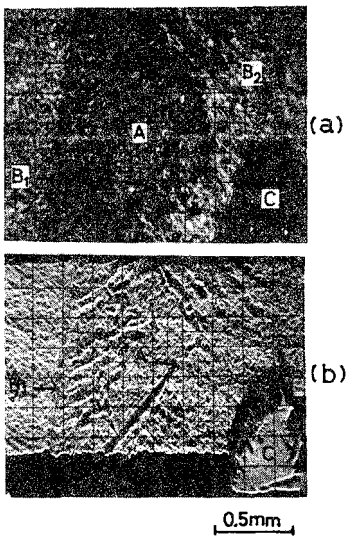

Fig. 6. Scanning laser images of a thin film solar cell fabricated on an alumina ceramic substrate.
(a) A reflection laser image. "A" indicates irregular boundaries, "B" linear boundaries and "C" the metal electrode.
(b) A y-modulated image of laser beam induced photocurrent.

higher than that at surfaces without any specific defects. However, the linear boundary B_2 does not effect the photocurrent at all. On the other hand, the photocurrent around irregular boundaries varies as much as 10%. These results suggest that the low diffusion length value is not determined by the presence of defects but presumably by deep-level impurities.

§4. Conclusion

Recrystallized silicon films having the mm grain size can be prepared on alumina ceramic using a multilayered structure consisting of borosilicate glass, polycrystalline silicon and titanium films. Thin film solar cells fabricated on the recrystallized films by chemical vapor deposition showed efficiencies of up to 2.6% and fill factor of up to 0.67.

Acknowledgments

The authors wish to thank Dr. Takao Miyazaki for preparing the oxide films on silicon, Dr. Eiichi Maruyama and Dr. Yoshiro Otomo for their technical discussions and encouragement throughout this work. This work was financed in part by the Agency of Industrial Science and Technology, Ministry of International Trade and Industry.

References

1) P. H. Fang and L. Ephrath: Appl. Phys. Letters **25** (1974) 583.
2) T. L. Chu, H. C. Mollenkopf and S. C. Chu: J. Electrochem. Soc. **123** (1974) 106.
3) C. Daey Ouwens and H. Heijligers: Appl. Phys. Letters **26** (1975) 569.
4) J. C. C. Fan and H. J. Zeiger: Appl. Phys. Letters **27** (1975) 224.
5) V. Y. Doo: J. Electrochem. Soc. **111** (1964) 1196.
6) R. J. Jaccodine: J. Electrochem. Soc. **110** (1963) 524.
7) A. M. Barnett: *Semiconductors and Semimetals* (Academic Press, New York, 1970) p. 141.
8) L. M. Terman: Solid-State Electronics **2** (1961) 1.

JAPANESE JOURNAL OF APPLIED PHYSICS
VOL. 16, NO. 5, MAY, 1977 pp. 807–812

Polycrystalline Indium Phosphide Solar Cells Fabricated on Molybdenum Substrates

Tadashi SAITOH, Sunao MATSUBARA and Shigekazu MINAGAWA

Central Research Laboratory, Hitachi Ltd., Kokubunji, Tokyo

(Received November 22, 1976)

Heterojunctions on polycrystalline indium phosphide films are fabricated and characterized. The InP films are chemically deposited on molybdenum substrates. Cuprous selenide films, being cubic in crystal structure and degenerate in conduction, are prepared on *n*-type InP films. Cu_xSe/InP thin film solar cells have efficiencies of up to 1.7% with a short circuit current density of 11 mA/cm² under AM 1 simulated irradiation.

Furthermore, CdS/InP heterojunction solar cells are fabricated by evaporating indium-doped CdS films on zinc-doped InP surfaces. The efficiency directly increases with the annealing temperature of the cells up to 2.0% with a short-circuit current density of 18 mA/cm². A collection efficiency of 70% is obtained at a wavelength of 0.65 μm from a spectral response curve. In addition, the electron diffusion length is calculated to be 0.2 μm, which determines the lower collection efficiency at longer wavelengths.

§1. Introduction

Thin film solar cells of polycrystalline semiconductors on inexpensive substrates have been studied as feasible candidates for obtaining low-cost solar cells for terrestrial use.[1-3] Indium phosphide is selected because of its high theoretical conversion efficiency, thin solar energy absorption layer and low energy consumption for fabricating solar cells compared with conventional silicon solar cells.[4] Consequently, the growth, structure and electrical properties of polycrystalline indium phosphide films on molybdenum have been investigated.[5-7]

In general, photovoltaic conversion can be realized by preparing potential barriers on the films, i.e. homojunctions, heterojunctions and Schottky barriers. As for the polycrystalline indium phosphide, zinc diffusion was first attempted to form *p-n* junctions. However, the rectification was poor, probably due to rapid diffusion of the zinc along the grain boundaries and excessive junction leakage. Therefore, heterojunctions on both *n*-type and *p*-type polycrystalline indium phosphide were fabricated.

Using *n*-type films, Cu_xSe/InP heterojunction solar cells were fabricated and the photovoltaic properties were characterized. It was recently reported that CdS/InP heterojunction solar cells had relatively high efficiencies for both monocrystalline and polycrystalline InP layers.[8,9] In this paper, the preparation and properties of CdS/InP polycrystalline cells on molybdenum substrates were investigated.

§2. Experimental

2.1 *Film preparation*

Polycrystalline InP films were chemically deposited on 50 μm thick Mo sheets using an In–PCl_3–H_2 reaction system.[5] The Mo sheets were selected because of the small thermal expansion coefficient mismatch between InP and Mo and chemical durability in a growth ambient. After cleaning in organic solvents, the Mo surface was etched in a $1H_2SO_4$–$1HNO_3$–$3H_2O$ solution.

Deposition was carried out in a horizontal reactor at an indium source temperature of 750°C and substrate temperatures between 550°C to 650°C. Typical deposition rate at 600°C was about 6 μm/hr and the deposition activation energy was 15 kcal/mol. Zinc phosphide was used as a *p*-type dopant. The InP films were attached to a glass plate and the Mo substrates were etched off. Then, the electrical properties of both *n*-type and *p*-type films were measured by the van der Pauw method.[10]

2.2 *Solar cell fabrication*

Prior to heterojunction formation, *p*-type cuprous selenide and *n*-type cadmium sulphide evaporated on glass plates were characterized

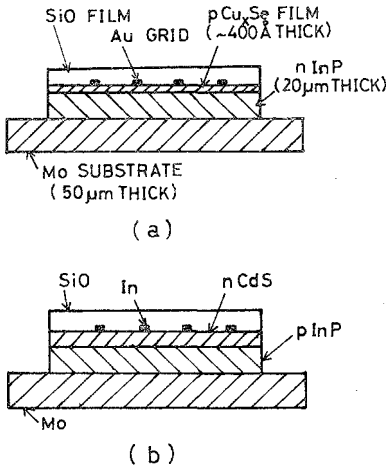

Fig. 1. Schematic representation of two-type heterojunction solar cells fabricated on Mo substrates. (a) *p*-type Cu_xSe on *n*-type InP cell, (b) *n*-type CdS on *p*-type InP cell.

by reflection electron microscopy, X-ray diffraction, optical absorption and Hall measurements.

In the case of Cu_xSe/InP heterojunction solar cells, cuprous selenide films with a thickness of around 400 Å were prepared in a vacuum on undoped, 20 μm thick, *n*-type InP films. Gold grid patterns with a 50 μm line width and a 1 mm spacing were formed in a vacuum on the Cu_xSe films. Then, InP deposits on the Mo back surface and periphery of the cells were etched off to reduce the series resistance and the leakage current, respectively. Finally, a lead wire was attached to the gold grid with a silver-epoxy resin and a SiO antireflecting film was applied. The resulting configuration of Cu_xSe/InP cells is schematically shown in Fig. 1 with that of CdS/InP thin film solar cells.

Zinc-doped, 18 μm thick, *p*-type InP films were chemically deposited on Mo sheets at around 600 °C as the first step in the fabrication of CdS/InP cells. Then, *n*-type (In-doped) CdS films were prepared on the *p*-type InP films at 200 °C by an ordinary vacuum evaporation technique using sintered CdS sources. The CdS films used were 2 μm thick. Indium metal grids, the same size as mentioned above, were formed on the CdS films. Other fabrication conditions were similar to those of Cu_xSe/InP solar cells. Finally, the electrical and optical properties of the heterojunction solar cells were measured.

§3. Results and Discussion

3.1 *Properties of indium phosphide films*

3.1.1 *Structural properties*

The structure varied mainly with deposition temperature and growth time and not with reaction gas concentration in the case of *n*-type InP films. A film deposited at 600 °C was relatively columnar as shown in Fig. 2(a). The grains with columnar structures were found to be oriented predominantly in the ⟨110⟩ direction using X-ray diffraction measurement.[5] However, the films deposited at temperatures less than 550 °C or being thinner than 5 μm tended to be random in orientation.

(a) (b)

Fig. 2. Photomicrographs of polycrystalline InP films on Mo substrates. (a) Scanning electron micrograph, (b) Replica electron micrograph.

As-deposited surfaces of the films were examined using replica electron micrography and are shown in Fig. 2(b). The micrograph shows that the surfaces consisted of various sized grains with lineages and flat facets. The lineages presumably correspond to the twin boundaries obserbed previously.[6]

However, *p*-type films were found to be random in orientation irrespective of deposition conditions. Especially, InP whiskers tended to appear with increasing zinc concentration in the growth ambient. This tendency prevented *p*-type films from having low resistivities.

3.1.2 *Electrical properties*

For undoped films, the electron concentration of a 20 μm thick film was 10^{15} to 10^{17} cm^{-3} and increased with increase in deposition temperature.[7] The electron mobility and resistivity were on the order of 10 $cm^2/V \cdot s$ and 10 to 100 $\Omega \cdot cm$, respectively. The barrier heights were 0.2 to 0.3 eV as obtained from the relationship between the resistivity and reciprocal temperature.[7] However, the electrical properties of sulphur-doped films were found to be strong functions of the deposition conditions and doping levels.

The Hall measurement of *p*-type InP films was performed using a Au/Zn/Au contact.[11] The resistivity, mobility and hole concentration of a 70 μm thick film were 18 $\Omega \cdot cm$, 7.5 $cm^2/V \cdot s$ and 4.6×10^{16} cm^{-3}, respectively.

3.2 Cu_xSe/InP *solar cells*

3.2.1 *Properties of cuprous selenide films*

The structures of Cu_xSe films prepared on glass plates were examined by reflection electron diffraction. It was found that the films evaporated at room temperature were amorphous whereas those evaporated at more than 150°C were polycrystalline. Furthermore, the diffraction patterns observed consisted of three Debye rings closely relating to cubic $Cu_{2-x}Se$ crystals.

Film resistivity was on the order of 10^{-4} $\Omega \cdot cm$. Mobility prepared at 160 and 300°C was 3 to 4 $cm^2/V \cdot s$, being one order of magnitude lower than that of single crystal Cu_2Se.[12] Thus, the hole concentration was calculated 2×10^{22} cm^{-3}, which means that the films are non-stoichiometric and is consistent with the diffraction data.

The variation of electrical properties with substrate temperature also affected the optical properties of the films. Figure 3 shows the optical transmission spectra of Cu_xSe films prepared on glass plates. The transmission spectrum of films prepared at room temperature is quite different from those of films at higher temperatures. This difference corresponds to the structural variation with substrate temperature as mentioned above.

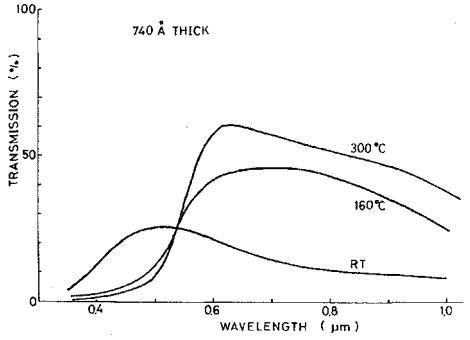

Fig. 3. The effect of substrate temperature on the transmission of Cu_xSe evaporated films. Glass plates were used as substrates and the evaporated film was 740 Å thick.

The decrease in transmission at longer wavelengths is considered related to the free carrier absorption. Transmission around 0.55 μm is believed due to a band-edge absorption, which is consistent with the results for a flash-evaporated film.[2] However, the absorption edge is different from the 1.2 eV value for single crystal cuprous selenide.[12] The difference is considered to be due to the absorption edge shifts to the higher energy side by the "Quantum Size Effect" as reported for InSb thin films.[13]

3.2.2 *Dark current-voltage characteristics*

Relationships between ln I and V for the Cu_xSe/InP heterojunctions are indicated in Fig. 4. The forward cnaracteristics are linear and rectification is realized at currents of more than 0.1 mA. The n value in the ln I vs. V relation was 1.9 for sample No. 121-6. The value is lower than that of sample No. 121-7, which has a lower conversion efficiency than the former. The 1.9 value indicates that the recombination of injected carriers in the space charge layer is controlled. As the Cu_xSe film is degenerate, the space charge layer in the InP side plays an important role in current injection.

3.2.3 *Conversion efficiency*

The substrate temperatures during the Cu_xSe film preparation and both the back and periph-

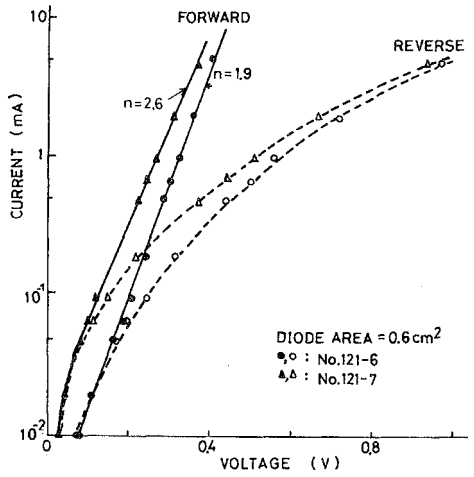

Fig. 4. Dark current-voltage characteristics of polycrystalline Cu_xSe/InP solar cells. Cell area is about 0.6 cm^2.

eral etching of Cu_xSe/InP cells were found to profoundly affect the conversion efficiency. For Cu_xSe films prepared at room temperature, the cells responded to light appreciably, whereas no photoresponse was observed for cells prepared at more than 400°C.

The etching-off of the InP deposit on the back and periphery greatly improved efficiency, especially short-circuit current density and fill factor. As a result, a Cu_xSe/InP solar cell with an efficiency of 1.7% was obtained. As shown in Fig. 5, the fill factor, short-circuit current density and open-circuit voltage were 0.47, 11 mA/cm^2 and 0.34 V, respectively. Another cell is depicted with an efficiency of 1.1% and a fill factor of 0.40.

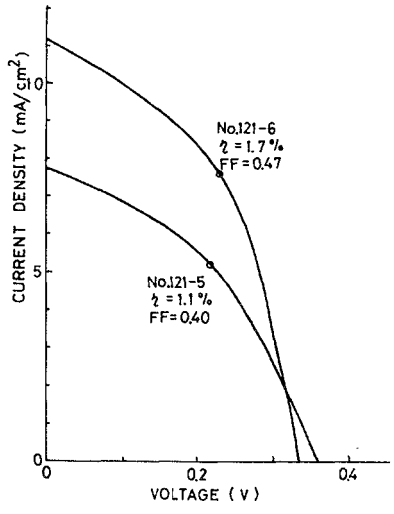

Fig. 5. Current-voltage characteristics of polycrystalline Cu_xSe/InP solar cells measured under AM 1 simulated solar irradiation (100 mW/cm^2).

3.2.4 *Collection efficiency*

In order to examine the reason for the low short-circuit current, the photoresponse curve was measured and the collection efficiency calculated. The highest collection efficiency was 40%, obtained at the 0.65 μm wavelength and the efficiency decreased with the increase in wavelength as shown in Fig. 6. This decrease is considered due to absorption variations in the depletion and/or bulk layers with wavelength.

Provided the effect of recombination in the depletion region can be neglected, the light-induced current generated in the depletion region is given by:[14]

$$J_{DL} = q\Phi[1 - \exp(-\alpha \cdot W)] \qquad (2)$$

where Φ is the incident photon flux, α the absorption coefficient and W the depletion layer width.

The depletion layer width for a one-sided step junction is described as:[15]

$$W = \sqrt{\frac{2K_s\varepsilon_0}{qN_d}(\phi_B + V)} \qquad (3)$$

where K_s is the dielectric constant, ε_0 the permittivity, N_d the electron concentration, ϕ_B the built-in potential and V the applied voltage. It is assumed that the built-in field increases proportionally to the energy gap. Using a depletion-layer width of 0.3 μm for a silicon p^+/n junction with an electron concentration of 10^{16} cm^{-3},[15] the depletion-layer width for InP was calculated to be 0.36 μm.

Inserting the depletion-layer width and the absorption coefficient[16] into eq. (2), the

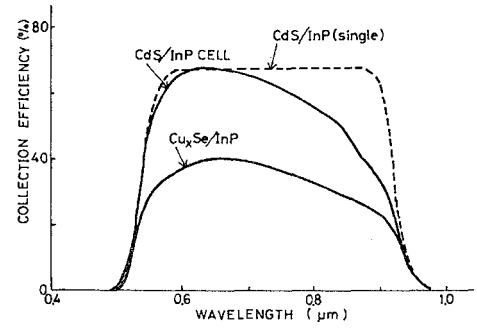

Fig. 6. Variation in collection efficiency with wavelength for single and polycrystalline CdS/InP cells and a polycrystalline Cu_xSe/InP cell.

quantum efficiencies in the depletion-layer were calculated to be 34% at 0.8 μm and 21% at 0.9 μm. These values nearly equal those shown in Fig. 6. This indicates that the diffusion length of *n*-type InP layer is so low that the contribution to the short-circuit current can be neglected.

3.3 CdS/InP *solar cells*

3.3.1 *Properties of cadmium sulphide films*

Cadmium sulphide films prepared on glass plates were examined by X-ray diffraction. The films were found to be cubic and oriented in the (111) face irrespective of temperature and thickness. Electrical properties were also measured by the van der Pauw method using In metal electrode. Undoped films were semi-insulating whereas low resistive CdS films were obtained when using In_2S_3-doped sources. Using an evaporation source including 50 mg In_2S_3/1 g CdS, the resistivity, mobility and electron concentration were found to be 2.9×10^{-3} $\Omega\cdot$cm, 3.1 cm^2/V$\cdot$s and 6.9×10^{20} cm^{-3}, respectively.

The transmission curve of In-doped CdS films was found to shift to the shorter wavelength side of undoped ones. This shift may result from the nonstoichiometry or the decrease of the Cd/S atomic ratio.

3.3.2 *Conversion efficiency*

For CdS/InP cells, the substrate temperature and etching-off of both the back and the periphery were also found to be important factors as mentioned above. Furthermore, cell efficiency increased with the increase in annealing temperature as shown in Fig. 7. The improvement is attributable to the increase in both the short-circuit current density and open-circuit voltage except for the fill factor. The best quality cell was obtained by evaporating the CdS film on the *p*-type InP layer at 200°C and subsequently being annealed at 500°C for 10 min in air. This cell showed a short-circuit current density of 18 mA/cm^2, an open-circuit voltage of 0.37 V, a fill factor of 0.30 and thus had an efficiency of 2.0%.

In addition, it is noticeable that a "kink" exists in the *I-V* curves near the maximum-power point. The kink was also reported by Bachmann *et al.* for a polycrystalline InP/CdS cell on a carbon substrate.[9] They pointed out that the kink is evidence of a rectifying contact between the *p*-type InP film and the carbon substrate. In the case of CdS/InP cells on Mo substrates, a rectifying contact is considered to be formed, which is one of the reasons for lower efficiencies compared with single crystal CdS/InP cells.

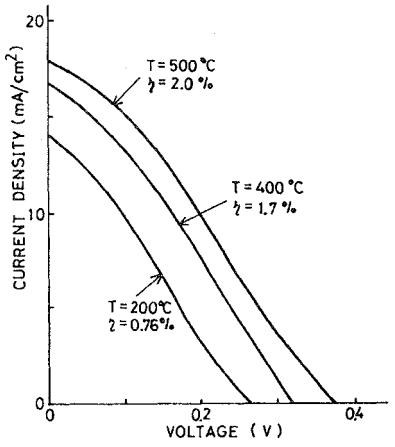

Fig. 7. The effect of annealing temperature on light current-voltage characteristics of polycrystalline CdS/InP solar cells with a cell area of 0.41 cm^2. The characteristics were measured under AM 1 simulated conditions.

3.3.3 *Spectral response*

The collection efficiency of polycrystalline CdS/InP cells at wavelengths of 0.6 to 0.7 μm is almost the same as that reported for the single crystal CdS/InP cell as shown in Fig. 6. However, the efficiency tends to decrease at longer wavelength. This decrease may be due to a low diffusion length in the *p*-type InP layer.

The diffusion current, generated outside the depletion layer in the bulk region and diffusing into the junction, is described as followed:[14]

$$J_{DIFF}=q\Phi\frac{\alpha\cdot L}{1+\alpha\cdot L}\exp(-\alpha\cdot W), \qquad (4)$$

where L is the diffusion length of minority carriers. Therefore, the total light-induced current, J_T, can be described as the following equation.

$$J_T=J_{DL}+J_{DIFF}=q\Phi\left[1-\frac{1}{1+\alpha\cdot L}\exp(-\alpha\cdot W)\right]. \qquad (5)$$

Here, Q and A are designated as follows:

$$Q=J_T/q\Phi, \qquad (6)$$

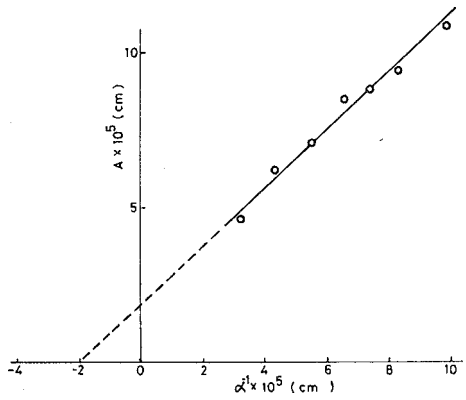

Fig. 8. Factor A vs. reciprocal absorption coefficient α^{-1} for a CdS/InP polycrystalline cell with an efficiency of 2.0%. Factor A is shown in eq. (7).

$$A=\frac{\exp(-\alpha\cdot W)}{(1-Q)\times\alpha}. \tag{7}$$

From eqs. (5) and (7),

$$A=\alpha^{-1}+L. \tag{8}$$

Figure 8 shows the relationship between A and α^{-1} for a polycrystalline CdS/InP cell using the data indicated in Fig. 6. An electron diffusion length of 0.2 μm was obtained, being considerably lower than 1.8 μm of single crystal InP.[17] Therefore, the low diffusion length value determines the decrease in collection efficiency at longer wavelengths in the spectral response curve.

§4. Conclusion

Heterojunctions on the polycrystalline InP films have been successfully fabricated with p-type Cu_xSe or n-type CdS films. The Cu_xSe/InP solar cells showed efficiencies of up to 1.7% with a short-circuit current density of 11 mA/cm^2. The spectral response curve indicated that only the photons, being absorbed in the depletion layer, contribute the light-generated current and thus the diffusion contribution to the current can be neglected.

By annealing the CdS/InP heterojunction cells at 500°C, efficiency was improved up to 2.0% with a short-circuit current density of 18 mA/cm^2. The collection efficiency obtained from the spectral response was close to 70% at wavelengths of 0.6 to 0.7 μm. An electron diffusion length of p-type InP films was realized of 0.2 μm, which determines the decrease in collection efficiency at longer wavelengths.

Acknowledgments

The authors are indebted to Dr. Takashi Tokuyama for his technical discussions and Dr. Yoshiro Otomo for his moral support. Part of this work was financially supported by the Agency of Industrial Science and Technology, Ministry of International Trade and Industry.

References

1) D. C. Reynolds, G. Leies, L. L. Antes and R. E. Marburger: Phys. Rev. **96** (1954) 533.
2) P. Vohl, D. M. Perkins, S. G. Ellis, R. R. Addiss, W. Hui and G. Noel: IEEE Trans. on Electron Devices **ED-14** (1967) 26.
3) T. L. Chu, H. C. Mollenkopf and S. S. C. Chu, J. Electrochem. Soc. **123** (1976) 106.
4) J. J. Wysocki and P. Rappaport: J. appl. Phys. **31** (1960) 571.
5) T. Saitoh, S. Matsubara and S. Minagawa: J. Electrochem. Soc. **123** (1976) 403.
6) T. Saitoh, S. Matsubara and S. Minagawa: Japan. J. appl. Phys. **15** (1976) 893.
7) T. Saitoh and S. Matsubara: J. Electrochem. Soc. (to be published).
8) J. L. Shay, S. Wagner, K. J. Bachmann and E. Buehler: J. appl. Phys. **47** (1976) 614.
9) K. J. Bachmann, E. Buehler, J. L. Shay and S. Wagner: Appl. Phys. Letters **29** (1976) 121.
10) L. J. van der Pauw: Philips Res. Rep. **13** (1958) 1.
11) L. M. Schiavone and A. A. Pritchard: J. appl. Phys. **46** (1975) 452.
12) G. B. Abdullaev, Z. A. Aliyarova and G. A. Asadov: Phys. Status solidi **21** (1967) 461.
13) O. N. Filatov and I. A. Karpovich: Fizika Tverdogo Tela **11** (1969) 1637.
14) W. W. Gärtner: Phys. Rev. **116** (1959) 84.
15) A. S. Grove: *Physics and Technology of Semiconductor Devices*, (John Wiley and Sons, Inc. New York, 1967) p. 163.
16) *Electronic Properties of Solids* (Academic Press, New York, 1973) p. 21.
17) S. S. Li: Appl. Phys. Letters **29** (1976) 126.

Fabrication and Characterization of Thin-Film Silicon Solar Cells on Alumina Ceramic

TERUNORI WARABISAKO AND TADASHI SAITOH

Abstract—**Dendritic silicon layers are prepared on alumina ceramic by melting and regrowing a CVD Si layer with a BSG encapsulation. Thin-film solar cells fabricated by successive deposition of p- and n^+-Si layers on this dendritic silicon exhibit a conversion efficiency of 2.6 percent under AM1 illumination.**

I. INTRODUCTION

THE THIN-FILM approach is known to have an essential advantage in realizing low-cost solar cells for large-scale terrestrial application. Several attempts have been made to fabricate solar cells on various materials such as steel [1] or graphite [2].

Another possible choice for the substrate is ceramic material. Recently, polycrystalline silicon thin films with a comparably large area have been obtained on alumina ceramic by CVD [3] and/or by dipping a substrate into molten silicon [4].

A large-area dendritic silicon film has also been obtained by melting and regrowing a chemically deposited silicon layer with glass film encapsulation, in conjunction with the use of a titanium layer to improve the wettability between the silicon and the alumina ceramic [5]. This correspondence describes the feasibility of fabricating solar cells on such a dendritic silicon film.

Manuscript received. This work was supported in part by the Agency of Industrial Science and Technology, MITI, Japan, as a part of the National Research and Development Program "Sunshine."

The authors are with the Central Research Laboratory, Hitachi Ltd., Kokubunji, Tokyo, Japan.

 Annals No. 704ED023

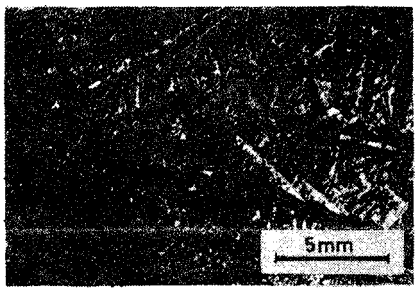

Fig. 1. Surface of a dendritic silicon film on an alumina ceramic substrate.

II. Experimental Details

The substrate material consisted of $1 \times 1 \times 1/32$ in 96-percent Al_2O_3 alumina ceramic slides. These slides were nonporous and their grain size was several microns in diameter.

A Ti layer, about 1000 Å thick, was formed by vacuum evaporation on the alumina ceramic slides. A polycrystalline Si layer, about 20 μm thick, was chemically vapor deposited (CVD) onto the Ti layer by hydrogen reduction of trichlorosilane ($SiHCl_3$) at 1100°C. At the same time, diborane (B_2H_6) was heavily doped into the silicon film.

In addition, a borosilicate glass (BSG) film, 1–2 μm thick, was chemically deposited on the silicon layer followed by the deposition of CVD-SiO_2 film to a thickness of about 0.2 μm. This CVD-BSG film contained about 10 mol% of B_2O_3 and liquified completely at around 1400°C.

The substrate was heated to 1417°C in an air ambient, and was held at this temperature until the silicon layer melted completely. Then, it was cooled to room temperature at the rate of about 80°C/min. A flat dendritic silicon thin film was thus obtained. The surface of the film is shown in Fig. 1. The resistivity of the resulting dendritic films was around $1 \times 10^{-3}\ \Omega \cdot$ cm.

After removing the oxide layers on the silicon film, a p-type and an n^+-type silicon layer were grown successively by hydrogen reduction of $SiHCl_3$ on the revealed silicon layer to a thickness of about 17 μm and 0.6 μm with doping levels of 10^{16} cm^{-3} and 10^{19} cm^{-3}, respectively. Dopants used were B_2H_6 and PH_3, and the deposition temperature was 1100°C.

Then, the multilayered film was masked and mesa-etched to complete a number of diodes. Point contacts were provided for the measurement of the electric characteristics by placing small dots of In–Ga alloy on the top of the n^+-layer of the diodes and on the revealed surface of the p^+-layer. An example of these mesa diodes is shown in Fig. 2 along with a schematic diagram of its structure.

III. Results and Discussion

Photovoltaic characteristics were measured under illumination of an AM1 (100 mW/cm^2) solar simulator (USHIO Electric). Open-circuit voltage V_{oc}, short-circuit current density J_{sc}, and fill factor FF were in the ranges

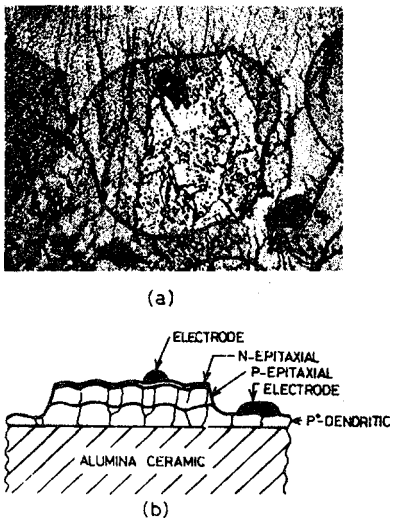

Fig. 2. (a) Top view of a mesa diode. (b) Schematic cross section of (a).

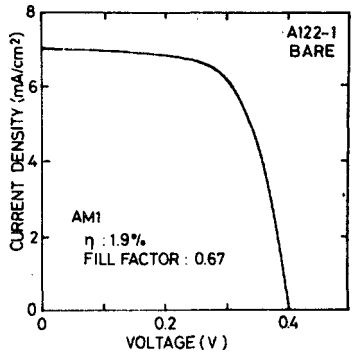

Fig. 3. Current–voltage characteristics of a thin-film silicon solar cell on an alumina ceramic substrate measured under AM1 illumination at room temperature.

of 0.34–0.40 V, 5.8–7.5 mA/cm^2, and 0.35–0.67, respectively. The average conversion efficiency was 1.26 percent without antireflection coatings.

The current–voltage characteristics of the cell (A122-1), which showed the highest conversion efficiency, are shown in Fig. 3. The values for V_{oc}, J_{sc}, and FF were 0.40 V, 7.0 mA/cm^2, and 0.67, respectively, corresponding to a conversion efficiency of 1.9 percent. The conversion efficiency of the same cell was improved to 2.6 percent after evaporation of SiO to about 750 Å.

Spectral response curves were obtained under illumination of a constant energy light with a power density of 30.4 μW/cm^2 and a bandwidth of 70 Å. An example of the spectral response of a solar cell is shown in Fig. 4. The photoresponse showed a maximum at a wavelength of 540 nm. The quantum efficiency at this wavelength was about 20 percent. The diffusion length of the electron in the p-layer estimated from the photoresponse curve was 1.0 μm.

Local variation in photocurrent was measured by scanning a He–Ne laser spot across the surface of a cell with a resolution of better than 5 μm. An example of the

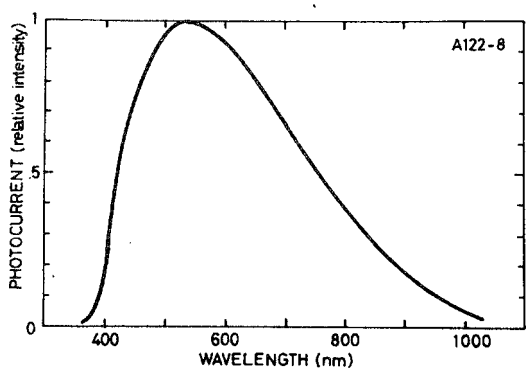

Fig. 4. Spectral response of a thin-film silicon solar cell on an alumina ceramic substrate, measured under constant energy of 30.4 μW/cm^2 with a bandwidth of 70 Å.

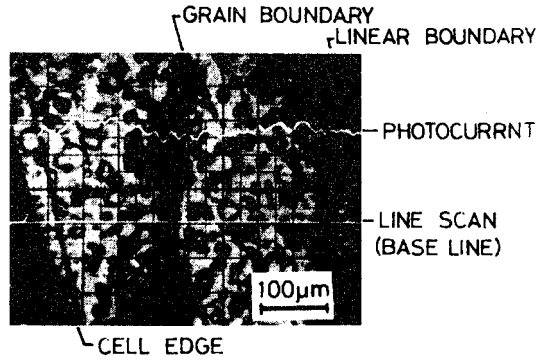

Fig. 5. A line scan mode of the photocurrent in the cell shown in Fig. 2 with corresponding surface reflection image measured by a scanning laser microscope.

photocurrent distribution in the cell shown in Fig. 2 is shown in Fig. 5 with a corresponding surface reflection image. A line scan covered the edge of the cell and several grain boundaries.

A little degradation in photocurrent is observed in the vicinity of irregularly shaped grain boundaries and micro defects. However, many of the observable defects such as tilt or twin boundaries were found to give little effect on the degradation in photocurrent.

Typical forward and reverse characteristics of a solar cell measured in the dark are shown in Fig. 6. No saturation region is observed in the reverse bias relation. An ohmic current is predominant in the low bias range, and the shunt resistivity of the cell can be estimated to be 1.2×10^4 $\Omega \cdot \text{cm}^2$.

In the small bias region, the forward J–V relation excluding the leakage component is fairly expressed by the following equation:

$$J = J_0 \exp [qV/(nkT)] \quad (1)$$

where J and V are the forward current density and the forward bias, respectively, and the other parameters indicate ordinary meanings. The characteristic values are 2.0 and 9.1×10^{-7} A/cm^2 for n and J_0 in (1), respectively, showing that the recombination current is predominant in the forward current.

The series resistivity of the cell can readily be estimated from the deviation of the J–V curve without the leakage

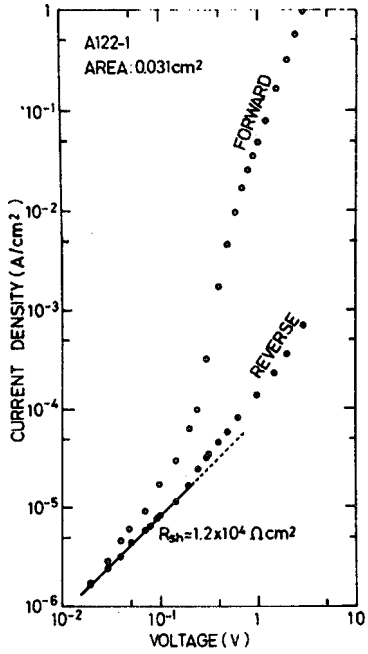

Fig. 6. Current–voltage characteristics of a thin-film silicon solar cell on an alumina ceramic substrate measured in the dark.

component from the relation (1). The resulting series resistivity obtained was 11 $\Omega \cdot \text{cm}^2$, being somewhat high compared to conventional single crystalline solar cells.

In the short-circuit condition, the light generated current J_L can be expressed by

$$J_L = \frac{R_d R_s + R_s R_{sh} + R_{sh} R_d}{R_d R_{sh}} J_{sc}. \quad (2)$$

Using n and J_0, the dynamic impedance R_d of the equivalent diode under short-circuit condition is calculated to be 5.7×10^4 $\Omega \cdot \text{cm}^2$. This and the values for R_{sh} and R_s give $J_L = 1.00_1 J_{sc}$.

The thickness of the optically active silicon layer was 17 μm. More than 80 percent of impinged solar light energy can be absorbed in this layer. So the low J_{sc}, or low J_L, can be attributed to the low correction efficiency of this layer. It is plausible that the short diffusion length of a light generated carrier might be the direct reason for the low J_{sc}.

The open-circuit voltage can be expressed simply as

$$V_{oc} = \frac{nkT}{q} \ln \left(\frac{J_L}{J_0} - \frac{V_{oc}}{J_0 R_{sh}} \right). \quad (3)$$

In the case of A122-1, $J_L \simeq J_{sc} = 7.0$ mA/cm^2, and $V_{oc}/R_{sh} = 3.3 \times 10^{-2}$ mA/cm^2, only 0.5 percent of the photocurrent flows through the shunt resistance even in the open-circuit condition.

Consequently, the low V_{oc} can be mainly attributed to the high value of J_0, or to the short recombination lifetime of the carrier in the depletion region.

IV. Conclusion

A new approach to low-cost solar cells was attempted by fabricating thin-film cells on a polycrystalline silicon film

dendritically grown on alumina ceramic substrates.

Although the experimental work was on a preliminary stage, a conversion efficiency of 2.6 percent was obtained under AM1 illumination with the open-circuit voltage of 0.4 V and the short-circuit current density of 9.8 mA/cm^2 being encouraging to this approach.

ACKNOWLEDGMENT

The authors are indebted to H. Itoh, N. Nakamura, and H. Tamura for their technical assistance in the experimental work, and to Dr. T. Tokuyama, and Dr. S. Minagawa for helpful discussions.

REFERENCES

[1] T. L. Chu *et al.*, "Polycrystalline silicon solar cells on low cost foreign substrates," *Solar Energy*, vol. 17, pp. 229–235, Sept. 1975.
[2] T. L. Chu, H. C. Mollenlopf, and Shirley S. C. Chu, "Deposition and properties of silicon on graphite substrates," *J. Electrochem. Soc.*, vol. 123, pp. 106–110, Jan. 1976.
[3] R. P. Ruth *et al.*, "Chemical vapor deposition growth," ERDA/JPL 954372-76/2, Quarterly Report No. 2, July 1976.
[4] J. D. Heaps and P. W. Chapman, "Silicon sheet dip coating process," presented at National Workshop on Low Cost Polycrystalline Silicon Solar Cells, I-8, Dallas, TX, May 18–19 1976.
[5] T. Saitoh *et al.*, "Dendritic growth of silicon thin films on alumina ceramic and their application to solar cells," in *Proc. 8th Conf. Solid State Devices* (Tokyo, 1976), to be published.

FABRICATION AND CHARACTERIZATION OF SOLAR CELLS USING DENDRITIC SILICON THIN FILMS GROWN ON ALUMINA CERAMIC

S. Minagawa, T. Saitoh, T. Warabisako, N. Nakamura, H. Itoh and T. Tokuyama

Central Research Laboratory, Hitachi Ltd.
1-280 Higashi-Koigakubo
Kokubunji, Tokyo 185, Japan

SUMMARY

Thin-film silicon solar cells were fabricated on dendritic recrystallized silicon layers of mm grain size. A novel technique utilizing a multilayer structure, SiO_2/BSG/Si/Ti/Al_2O_3, was effective in obtaining a flat dendritic silicon film by the melt-regrowth process of a chemically deposited silicon film.

A $n^+/\pi/p^+$ type cell, prepared by successively depositing undoped and phosphorus doped silicon layers on the dendrite film, exhibited the conversion efficiency as high as 3.2% (AM1) with the open circuit voltage of 0.32V and the short circuit current density of 16.7 mA/cm^2.

INTRODUCTION

The thin-film approach has been applied to the fabrication of silicon solar cells in order to explore the way to reduce the cell cost drastically[1)2)3)4)]. In this approach, principal efforts are directed to finding low cost substrates compatible with the silicon film and to obtain large crystallite grain size.

Steel, graphite and metallurgical silicon were used as substrate materials and grain growth by recrystallization or sintering was tried.[5)6)]

Results obtained, however, still need further improvement.

This paper deals with a new technique of preparing thin-film silicon solar cells with large crystal grains on alumina ceramic substrates and their characterizations in photovoltaic properties.

The key technique is in depositing a multilayer of SiO_2/BSG (borosilicate glass)/Si/Ti on an alumina ceramic substrate and in successively recrystallizing the silicon film into dendrites after raising temperature to the melting point of silicon.[7)]

A thin-film solar cell with grains of mm size was once fabricated on an alumina ceramic, a moderlately low cost substrate, by a melting and rapid cooling technique.[5)]

However, preparation of thin films with uniform thickness has been unsuccessful until the multilayer structure mentioned above is devised.[7)] The most difficult problem to be overcome was the poor wettability of molten silicon to alumina.

Molten silicon easily agglomerates on the surface of alumina preventing the formation of thin uniform recrystallized layer.

The Ti layer improves the wettability of silicon to alumina and the SiO_2/BSG layers work as a liquid encapsulation layer suppressing the balling phenomenon of molten silicon.

Unidirectional recrystallization by pulling out a substrate from inside of a furnace was also tried insted of nomal freezing in a furnace. Thin-films with parallel texture of dendrites were obtained.

Once a uniform silicon film with large crystallites (dendrites) is fabricated, active layers of a solar cell can easily be made by depositing p- and n^+-Si layers on it. Besides this $n^+/p/p^+$ type cells, cells with $n^+/\pi/p^+$ structure were also fabricated by depositing an undoped layer instead of the p-layer.

Although works included in the category of the ordinary recrystallization and $n^+/p/p^+$ type are centered in this paper, results on the unidirectional recrystallization and the $n^+/\pi/p^+$ structure are also described.

Characterization of the recrystallized layers and the photovoltaic characteristics of the thin-film solar cells were performed. A laser-beam scanning apparatus to measure photoresponse distribution was a useful tool for the characterization of the thin-film cells.

EXPERIMENTAL

Substrate Fabrication

Alumina ceramic plates, 96% pure and 25 mm x 25 mm x 1 mm in size, were coated with 0.1 μm thick titanium film by vacuum evaporation.

A polycrystalline p^+-silicon layer, about 20 μm thick, was deposited on the titamum layer by chemical vapor deposition using trichlorosilane and diborane.

Finally a 1-2 μm thick borosilicate glass layer (10 mol. % in B_2O_3 content) and a 0.1 μm thick silicon dioxide layer were successively formed by chemical vapor deposition.

This multilayer structure (Fig. 1) was heated to 1417°C in an air ambient.

The electric power supply of the furnace was turned off when the silicon layer completely melted and the substrate was cooled in the furnace at a rate of 10 deg/min.

An attempt to develop dendrites in one direction was achieved by pulling out a substrate from the center of a horizontal furnace at a rate of 1.4 cm/min.

Solar Cell Fabrication

A p-type and n-type silicon layers were successively grown epitaxially on the dendrite layer after dissolving off the surface oxide layer by hydrofluoric acid.

Hydrogen reduction of trichlorosilane at 1100°C with diborane and phosphine as doping gases was employed for depositing the silicon layer.

The p- and n-layers were 17 μm and 0.6 μm thick and their carrier concentrations were 10^{16} - 10^{17} cm^{-3} and 10^{19} cm^{-3}.

Beside this $n^+/p/p^+$ type solar cell, the $n^+/\pi/p^+$ type cells were fabricated by replacing the boron-doped layer with an undoped layer, in order to investigate the effects of the dopant concentration in the active layer.

A large area solar cell was completed by attaching a titanium/silver electrode to the n^+-layer by successive evaporation through a metal mask and a aluminum contact to the p^+-layer revealed by mesa etching.

An indium/gallium contact was employed for the n^+-layer when a solar cell was divided into a number of small mesa diodes to investigate the local variaion in photovoltaic properties.

Antireflection film was a 750Å thick silicon monoxide deposided by vacuum evaporation.

The structure of the thin-film solar cell is shown in Fig. 2.

Measurements

Photovoltaic characteristics of the thin-film solar cell were measured under simulated AM1 (100 mW/cm^2) light.

A constant energy spectrometer was used to measure the spectral response of solar cells. The energy density was 30.4 $\mu W/cm^2$ and the band width was 70Å.

Photoresponse distribution maps were made by measuring photocurrent by scanning a He-Ne laser beam. Resolution achieved was better than 5 μm.

RESULTS AND DISCUSSION

Recrystallization

An attempt to enlarge the crystallite size of a silicon thin-film by the melt-regrowth scheme has been impeded by the agglomeration of molten silicon on alumina. This phenomenon is due to the high surface tension of molten silicon and the poor wettability of molten silicon to alumina.

Titanium film inserted between silicon and alumina was found to be effective for increasing the wettability of molten silicon to alumina and even more it was effective for preventing the recrystallized film from peeling off.

As the surface of the recrystallized film thus obtained was not smooth enough to fabricate solar cells, additional films were deposited on the top of the silicon layer. A combination of SiO_2/BSG films revealed useful for this purpose. The BSG film (10 mol.% in B_2O_3 content) becomes very soft and fluid at about 1390°C helping to make smooth silicon surface. However, back up of this liquid encapsulant by a SiO_2 layer was necessary to maintain stiffness of the overlayer.

The ambient gas during recrystallization was important to obtain a flat surface. The oxide films tend to be lost in nitrogen or argon ambient but not in oxigen or air, suggesting slower reduction rate of oxides by molten silicon into high vapor pressure suboxides.

A typical surface of an ordinary recrystallized film and a unidirectionally recrystallized film were shown in Figs. 3 and 4.

X-ray diffraction indicated the predominance of [111] orientation in the recrystallized film in contrast to the [110] predominance in the chemially deposited film.

The resistivity of the recrystallized film was 1×10^{-3} Ω·cm, about one half of the as-deposited film. Chemical analysis showed boron and aluminum were enriched probably due to the dissolution of borosilicate glass and alumina.

Hall mobility on the other hand was 40 cm^2/Vs, twice as large as the value of the as-deposited film, reflecting the better crystal perfection in the recrystallized film.

Photovoltaic Characteristics

Conversion efficiencies of the $n^+/p/p^+$ type and the $n^+/\pi/p^+$ type cells are plotted against the open circut voltages and the short circuit current densities in Fig. 5. These cells are made by etching a number of mesas on a solar cell of each type.

There exists a marked difference in the open circuit voltage and the short circuit current. The higher short circuit current densities or the higher conversion efficiencies of the $n^+/\pi/p^+$ cells may be ascribed to the wider depletion layer spreading in the π layers. A high collection efficiency in the π layer is understandable from the increased photocurrents in the longer wavelengths of the spectral response curves. (Fig. 6) (Table I.)

The hole concentration of the π layer was estimated in the level of 10^{14} cm^{-3} by capacitance-voltage measurement.

The origin of lower open circuit voltages of the $n^+/\pi/p^+$ cells was due to a larger saturation current which comes from the wider depletion layer.

An example of the photocurrent distribution map measured by scanning a laser spot across a thin-film cell is shown in Fig. 7 together with a corresponding surface optical micrograph. A small

dip in photocurrent is observed when the laser spot crosses an irregular grain boundary. Many of the observable defects as tilt or twin boundaries, however, were found to be harmless.

Therefore, investigation to increase the lifetime of minority carriers rather than to eliminate recombination at grain boundaries must be emphasized to get higher photocurrent output. The lifetime killer in the thin-film solar cell has not been identified, although titanium in the substrate may be associated with.

Another factor which governs the conversion efficiency is the fill factor.

Larger $\left.\frac{dV}{dI}\right|_{V=o}$ and smaller $\left.\frac{dV}{dI}\right|_{I=o}$ are considered to correspond to a larger fill factor.

The two terms can be approximated to

$$\left.\frac{dV}{dI}\right|_{I=o} \approx R_s + K(n, I_o, R_{sh}) \quad (1)$$

$$\left.\frac{dV}{dI}\right|_{V=o} \approx R_{sh} \quad (2)$$

R_s: series resistance
I_o: saturution current
R_{sh}: shunt resistance
n: factor in I-V relation for a diode.

Here, we proceed by using the simpler equation (2).

The fill factors and the graphically obtained $\left.\frac{dV}{dI}\right|_{V=o}$ values, i.e. shunt resistances are shown to have a close relationship to each other for $n^+/\pi/p^+$ type cells. (Fig. 8) This indicates that the increase in shunt resistivity and the minimization of the local variation of shunt resistivity are necessary in order to realize a high efficiency thin-film solar cell with a large area.

CONCLUSION

A new technique of fabricating a flat film of silicon dendrites on an alumina ceramic was attempted in order to develop a low cost solar cell. Uilization of the multilayer structure, SiO_2/BSG/Si/Ti/Al_2O_3, in recrystallizing process of silicon was a key to obtain a flat film of dendrites with mm size.

A thin-film solar cell prepared by successive deposition of an undoped and phosphorus-doped silicon layers on the dendrite substrate exhibited a photovoltaic conversion efficiency of 3.2% with Voc = 0.32V and Isc = 16.7 mA/cm^2 under AM1 simulated light.

Characterization of the thin-film cells indicated that the increase of minority carrier lifetime and the increase of shunt resistance were most important in attaining high conversion efficiency.

ACKNOWLEDGEMENTS

This work was partially supported by the Agency of Industrial Science and Technology, Ministry of International Trade and Industry, Japan

REFERENCES

1) P.H. Fang, L. Ephrath and W.B. Nowak, Appl. Phys. Letters 25 583 (1974)
2) T.L. Chu, H.C. Mollenkopf and S.S. C. Chu, J. Electrochem. Soc., 123, 106 (1975)
3) T.L. Chu, J.C. Lien, H.C. Mollenkopf, S.C. Chu, K.W. Heizer, F.W. Voltmer and G.W. Wakefield, Solar Energy, 17, 229 (1975)
4) T.L. Chu, H.C. Mollenkopf, K.N. Singh, S.S. Chu and I.C. Wu, IEEE 11th Photovoltaic Specialists Conference, paper No. 4, 10 (1975)
5) V.Y. Doo, J. Electrochem. Soc., 111, 1196 (1964)
6) C.D. Ouwens and H. Heijlingers, Appl. Phys. Letters, 26, 569 (1975)
7) T. Saitoh, T. Warabisako, H. Itoh, N. Nakamura, H. Tamura, S. Minagawa and T. Tokuyama, The 8th Conference (1976 International) on "Solid State Devices", Paper A-6-(3), (1976)

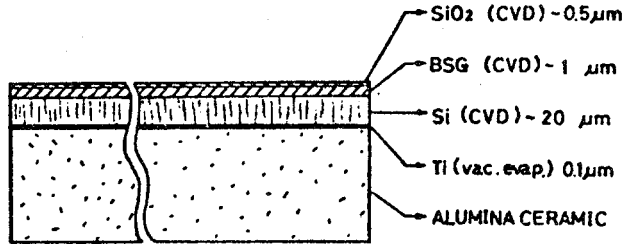

Fig.1 A multilayer structure used for recrystallization of silicon

Fig.2 Schematic diagram of thin-film silicon solar cell

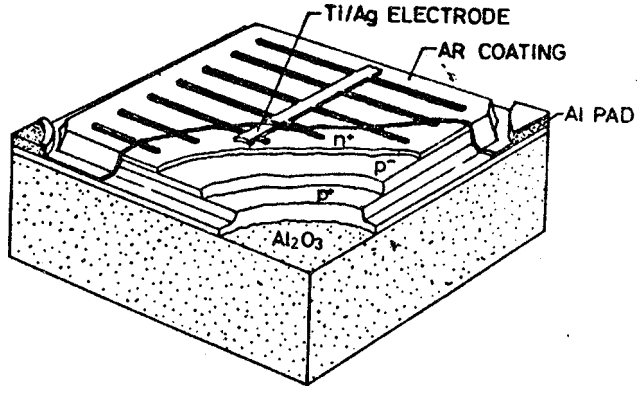

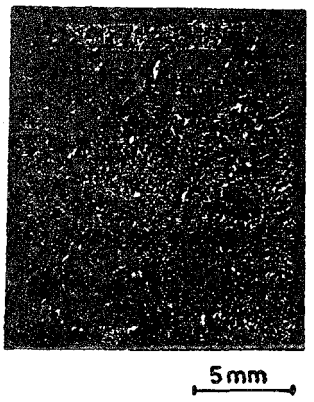

Fig.3 Normally recrystallized silicon film

Fig.4 Unidirectionally recrystallized silicon film

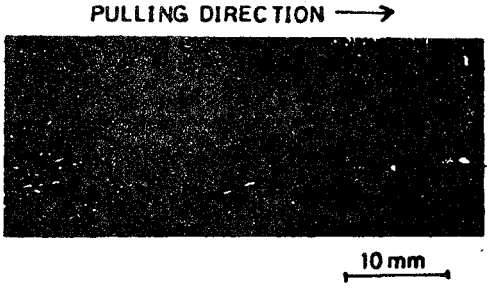

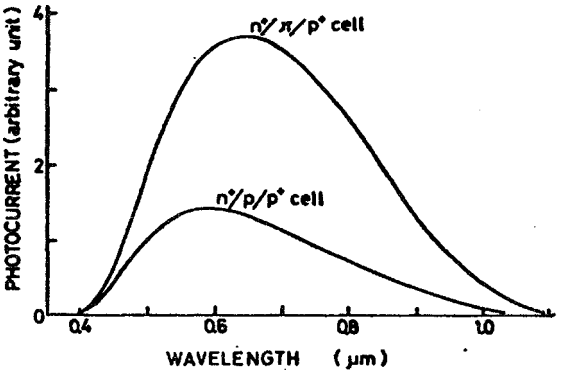

Fig.6 Spectral response of thin-film solar cells

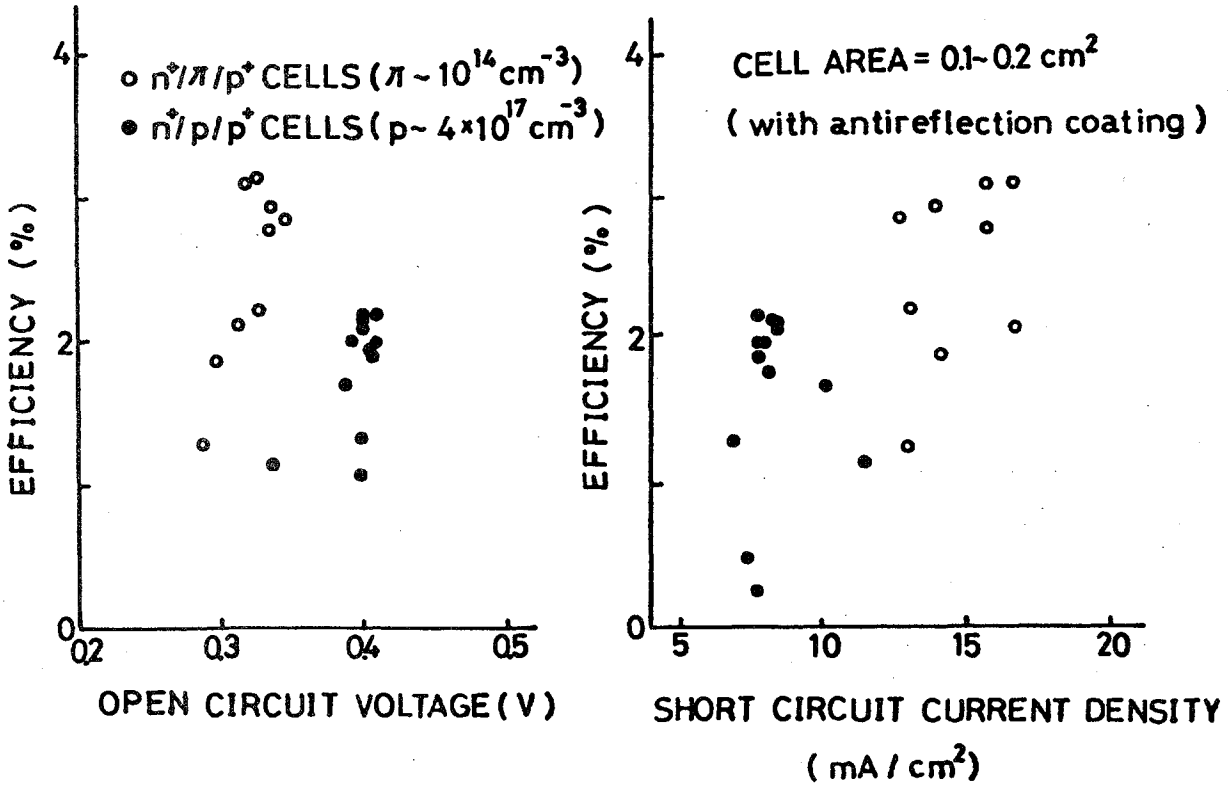

Fig.5 Conversion efficiency vs. open circuit voltage (a) or short circuit current density (b)

Table I. Photovoltaic characteristics of the $n^+/p/p^+$ and the $n^+/\pi/p^+$ thin-film cells.

	SHORT CIRCUIT CURRENT DENSITY	OPEN CIRCUIT VOLTAGE	FILL FACTOR	EFFICIENCY	AREA
	(mA/cm^2)	(V)	(%)	(%)	(cm^2)
$n^+/p/p^+$	7.8	0.41	69	2.2	0.14
$n^+/\pi/p^+$	16.7	0.32	59	3.1	0.16

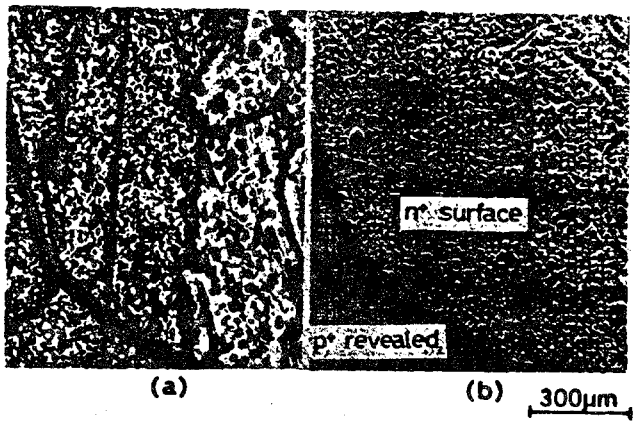

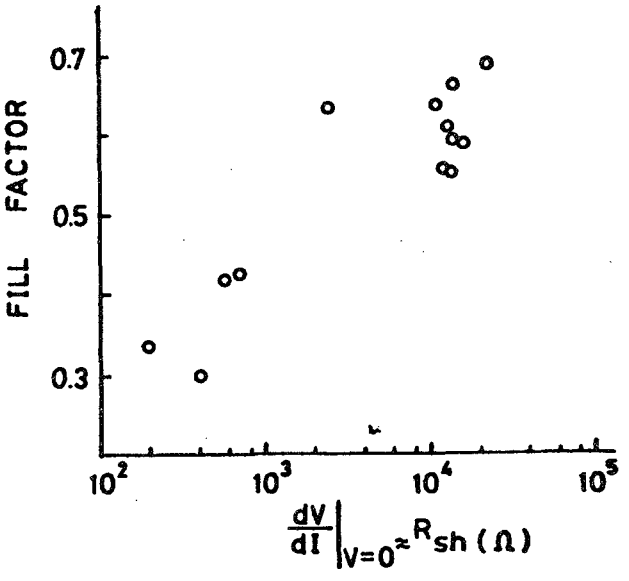

Fig.7 Photocurrent distribution (a) and corresponding optical image (b)

PROBLEMS IN PHOTORESPONSE DISTRIBUTION MEASUREMENT

Shigekazu Minagawa and Terunori Warabisako

Central Research Laboratory, Hitachi Ltd.
1-280 Higashi-koigakubo
Kokubunji, Tokyo 185
Japan

Photoresponse distribution measurement by scanning a light spot across a surface of a semiconductor device is often used in a variety of sections of device characterization.[1)2)3)4)]

This technique is very useful for solar cell characterization because the measured quantity is the direct expression of the distribution of the desired performance of the device.

Researchers of the thin-film solar cell must be implemented with this kind of apparatus, because the thin-film cell includes many defects, grain boundaries and precipitates in some cases which cause nonuniform and poor performance. Characterization of these defects and techniques for eliminating these maleffects must be explored before the thin-film solar cells can supply low cost electric energy.

The authors set up an apparatus for measuring the photoresponse distribution and use it in the development of polysilicon thin-film solar cells.

A schematic diagram of the apparatus and an example of measurement are shown in Figs. 1 and 2.

In using this apparatus, however, there exist several conditions to be satisfied if one wants to guarantee that the measured photocurrent expresses correctly the local photovoltaic property of the spot irradiated.

ELECTRIC PROPERTY OF CELL

Schematic diagrams of a polysilicon thin-film solar cell made on a ceramic substrate irradiated by a spot of light together with an equivalent circuit corresponding to it are shown in Fig. 3.

The equivalent circuit corresponding to the irradiated part i can be expressed by a parallel combination of a current source I_{Li}, an ideal diode and a shunt resistance R_{SHi} connected to a series resistance R_{Si}. The remaining dark part is similarly expressed with a shunt resistance R_{SH}, a series resistance Rs and a leak current I_D. The total equivalent circuit is a parallel combination of these two circuit via a series resistance R_B which depends on the mutual positions of the light spot and the electric contacts.

The measured short circuit current I_L for this system is given by

$$I_L = I_{Li} - I_D$$

$$= \frac{R_{SHi}}{R_{SHi} + R_{Si} + R_B} \left(I_o' + \frac{Vi}{R_{SHi}}\right) - I_D \qquad (1)$$

where

$$I_o' = I_{oi} \{\exp \beta(V_i - R_{si}I_{Li}) - 1\} \qquad (2)$$

$$I_D = \frac{R_{SH}}{R_{SH} + R_s} I_o \{\exp \beta(V - R_sI_D) - 1\} + \frac{V}{R_{SH} + R_S} \qquad (3)$$

The sympols β, Vi and V have usual meanings.

These equations show that the measured current I_L agrees with the photocurrent of the irradiated part i if the leak current I_D and the series resistance R_B, which often tend to be large particularly in thin-film cells, are small enough.

Absence of a systematic variation in photocurrent distribution with regards to the positions of the light spot and the electrodes guarantees this condition holds.

SCANNING SPEED

A limit is imposed on the scanning speed due to a large junction capacitance of a solar cell. When the surface of a solar cell with dimensions of ℓ_1 by ℓ_2 is scanned by a light spot of diameter ϕ at line frequency ω_1 and frame frequency ω_2, the transit time of the light spot τ_ϕ must be smaller than the charging time constant of the junction capacitance $\tau_c = RC$, i.e.

$$RC = \tau_c < \tau_\phi = \frac{\phi}{\ell_1\omega_1} . \qquad (4)$$

Where, R is the equivalent series resistance of a solar cell and C is the junction capacitance given by

$$C = \left(\frac{qK_S\varepsilon_o C_B}{2\phi_B} \right)^{1/2} \ell_1 \ell_2 \qquad (5)$$

Ks : permittivity of silicon, ε_o : permittivity of free space

C_B : free carrier concentration of the lower impurity concentratio side of a step junction, ϕ_B : built in potential.

Equations (4) and (5) are combined to give the limiting condition for line frequency,

$$\omega_1 < \phi/\{R\ell_1^2\ell_2(qK_S\varepsilon_o C_B/2\phi_B)^{1/2}\}. \qquad (6)$$

The frame frequence, $\omega_2 = \phi\omega_1/\ell_2$ is also governed by the same condition. Numeric calculation using the values shown in Table I indicates that the upper limit of the line frequency is 90.4 H_z and the time required for measuring one frame is 138 seconds.

RESOLUTION AND DENSITY OF SCANNING LINES

There exists a trade-off between the spot size and the density of the scanning lines with regards to the resolution and the frame frequency.

The spot size of light should be determined according to the object of the measurement: whether the whole photoresponse image across a cell or the fine structure of a specific area is required. In the former case, the minimum time necessary for measurement is restricted to $\ell_2 / \phi\omega_1$ as described above. A standard condition for measuring the whole image of a solar cell with dimensions of 10 cm by 10 cm is ω_1 = 1 kH_z, ω_2 = 30 H_z and ϕ = 1.5 mm. In the latter, resolution is limitted to about 0.8 μm even if the best available optics is employed for He - Ne laser light. On the other hand, the spot size need not be focused smaller than the diffusion length of the minority carriers.

OTHER FACTORS

The absorption coefficient of silicon and the diffusion length of the minority carrier should be taken into consideration when a light for

scanning is selected. Use of light sources with different wavelengths provides us with informations on the photorespose distribution in depth direction.

For example, He - Ne laser light (6328Å) and Ar laser lights (4880Å and 5145Å) in silicon correspond to the penetration depth of 2.7 μm, 0.75 μm and 1.0 μm, respectively, which are comparable to the magnitude of the diffusion length of the minority carrier often encountered in the thin-film solar cell.

Roughness of the surface of a thin-film solar cell may complicate quantitative understanding of the result of the distribution measurement because the condition of normal incidence does not hold and the effect of multireflection on the uneven surface may occur if the spot size becomes comparable to the roughness of surface.

Acknowledgements

This work was partially supported by the Agency of Industrial Science and Technology, Ministry of International Trade and Industry, Japan.

References

1) C.N. Potter and D.E. Sawyer, Rev. Sci. Instr., 39 180 (1968)
2) S.T. Soclof and P.A. Iles, Record of the 11th IEEE Photovoltaic Specialists Conference (1975)
3) D.L. Lile and N.M. Danis, Solid-State Electronics, 18 699 (1975)
4) L.A. Kasprzak, Rev. Sci. Instr., 46 257 (1975)

Table I. Values used for frequency limit calculation

diameter of light spot	$\phi = 2\ \mu m$
cell dimensions	$\ell_1 = \ell_2 = 25$ mm
equivalent series resistance of cell	$R = 1\Omega$
permittivity of silicon	$K_S = 11.7$
permittivity of free space	$\epsilon_O = 8.86 \times 10^{-14}$ F cm^{-1}
impurity concentration	$C_B = 10^{17}$ cm^{-3}
built-in potential	$\phi_B = 0.414$ V
electron charge	$q = 1.602 \times 10^{-19}$C

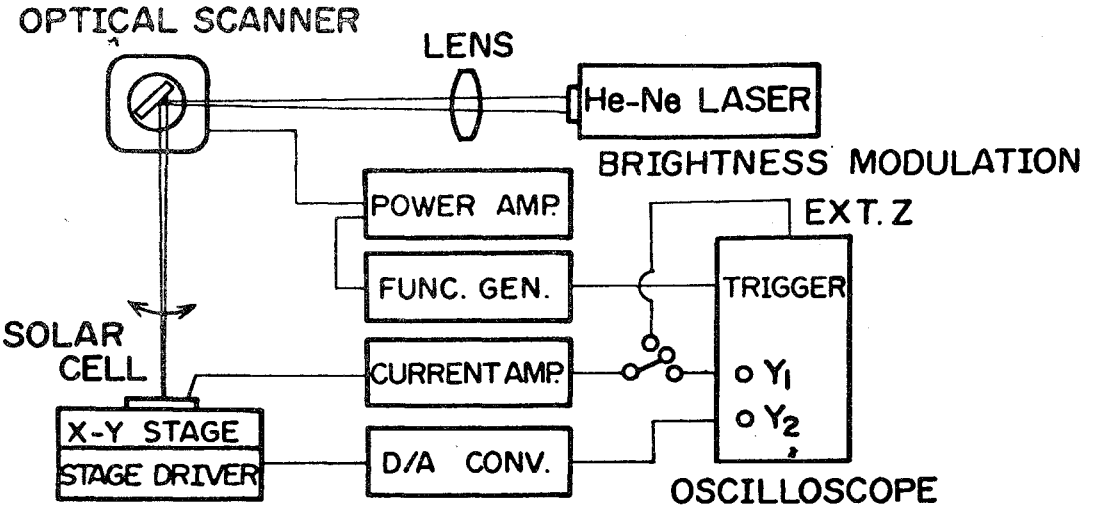

Fig. 1 Apparatus for photocurrent distribution measurement.

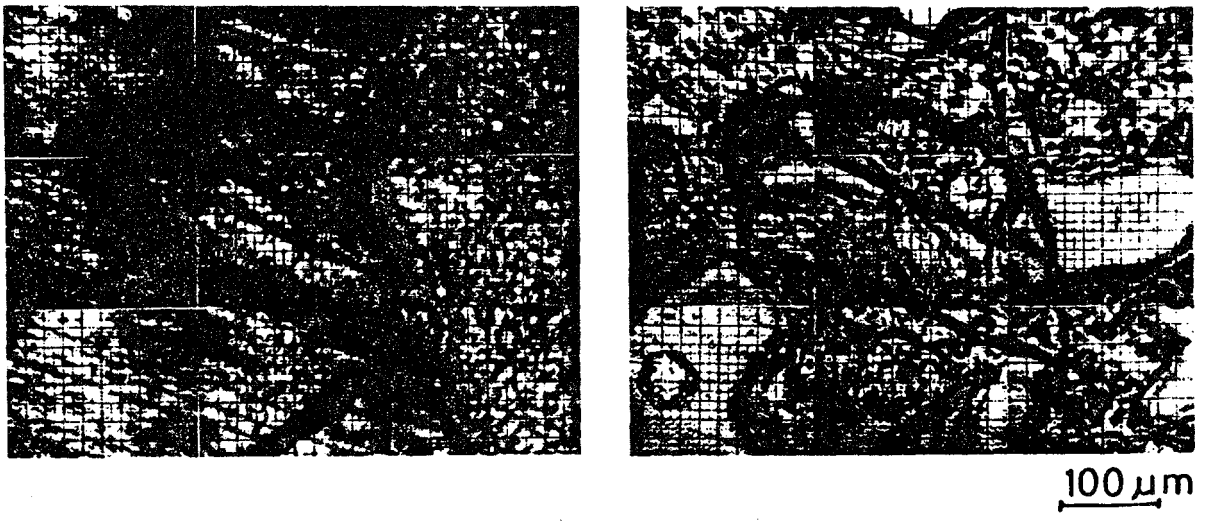

(a) photocurrent map

(b) surface optical micrograph

Fig. 2 A photocurrent distribution map of a thin-film silicon solar cell.

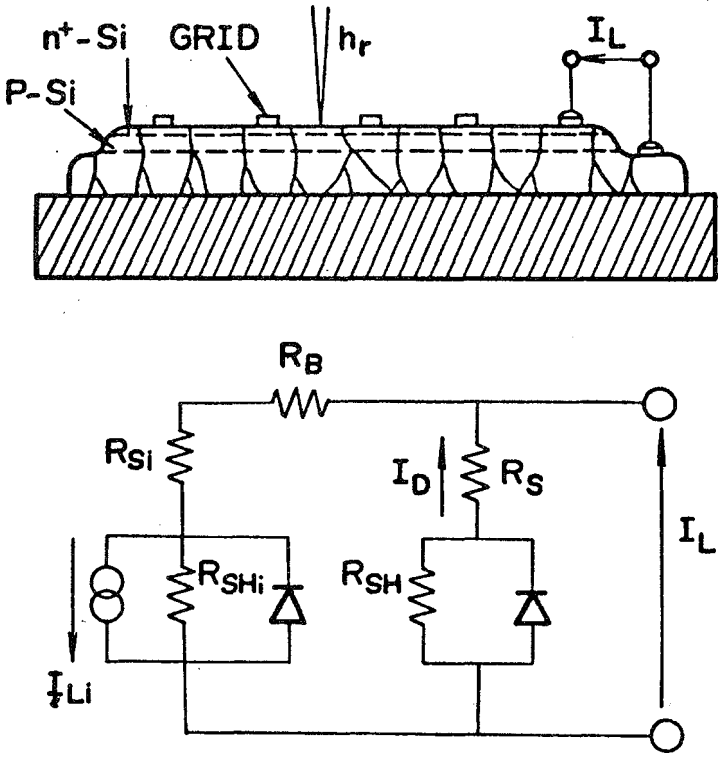

Fig.3 Photocurrent measurement by scanning a laser spot.

Reprinted from JOURNAL OF THE ELECTROCHEMICAL SOCIETY
Vol. 124, No. 7, July 1977
Printed in U.S.A.

Electrical Properties of n-Type Polycrystalline Indium Phosphide Films

Tadashi Saitoh and Sunao Matsubara

Hitachi Limited, Central Research Laboratory, Kokubunji, Tokyo, Japan

ABSTRACT

Electrical properties of n-type polycrystalline indium phosphide deposited on molydenum substrates are investigated as a function of deposition conditions. For undoped films, the electron concentration is found to be 10^{15}-10^{17} cm^{-3} and tends to increase with the increase in deposition temperature. The electron mobility and resistivity are almost constant irrespective of varying deposition conditions. On the other hand, the electrical properties of sulfur-doped films are found to be strong functions of deposition conditions and doping level. A grain boundary carrier trapping model is applied to explain the electronic transport properties of the polycrystalline films. The barrier height and the density of trapping states at grain boundaries are calculated.

Polycrystalline films of various semiconductors have been used in fabricating low cost solar cells (1-3). Consequently, the growth and structure of polycrystalline indium phosphide films have been investigated by the authors (4, 5). Understanding of the electronic transport properties of polycrystalline films are considered critical to the realization of solar cells with high conversion efficiencies.

In our present study, Hall measurement was performed to gain this clear understanding of the electrical properties of n-type polycrystalline indium phosphide as a function of deposition conditions. A model including carrier trapping centers at grain boundaries (6) was utilized to obtain the barrier height and the density of trapping states at grain boundaries.

Experimental

Polycrystalline films were prepared on 50 μm thick molybdenum sheets by chemical vapor deposition (4). The molybdenum sheets were cleaned in organic solvents and subsequently etched in a $1H_2SO_4$-$1HNO_3$-$3H_2O$ solution prior to indium phosphide deposition. This etchant makes molybdenum surfaces rough and acted effectively to secure a homogeneous nucleation in the initial stage of the deposition as well as to get pinhole-free films. The deposition was carried out at substrate temperatures between 450° and 650°C. Hydrogen sulfide was used as an n-type doping gas.

Electrical properties of both undoped and sulfur-doped films were measured by the van der Pauw method (7). Specimens for the measurement were prepared as follows: First, a polycrystalline film was attached upside down to a glass plate using an epoxy adhesive. Then, the molybdenum substrate was chemically etched off except four corners. The interface between the n-type polycrystalline indium phosphide and the molybdenum was found to have an ohmic contact. Consequently, the four molybdenum corners were used as electrodes.

Key words: Hall measurement, grain boundary, crystallite, barrier height, trapping density.

The Hall voltage was measured in both current polarities and averaged to calculate the electrical properties. The observed values of electron mobility, resistivity, and electron concentration were denoted as $\bar{\mu}$, $\bar{\rho}$, and $\bar{n}$, since the values relate to both crystallites and grain boundaries.

Resistivity vertical to the film surface was measured as follows: A eutectic AuGe alloy was evaporated on the film surface, annealed at 200°C in a hydrogen gas, and mesa-etched. Then, resistivity was calculated from the linear current-voltage relationship between the AuGe electrode and the Mo substrate.

Results

Undoped films.—The grain size of the polycrystalline films depended mainly on deposition temperature and growth time and not on PCl_3 concentration in a feed gas (4). So, the electrical properties were examined with respect to the former two conditions. The electrical properties of undoped films were compared to those of undoped epitaxial layers on Cr-doped single crystal substrates. The carrier concentration of polycrystalline films was appreciably lower than that of the epitaxial ones; whereas the electron mobility was lower and hence the resistivity higher by two orders of magnitude.

Resistivity of the polycrystalline films is almost constant irrespective of varying deposition temperature, as shown in Fig. 1. Also shown in the figure is the resistivity measured in a direction vertical to the film surface. The value is in the range of 1-10 $\Omega \cdot$ cm, being one order of magnitude lower than that measured parallel to the surface. The difference in the resistivities is considered to come from the difference in the orientation of the films (4).

On the other hand, electron concentration tends to increase with increasing deposition temperature and electron mobility decreases at around 600°C, as shown in Fig. 2 and 3, respectively. Since grain sizes increase at higher deposition temperatures, the grain boundary

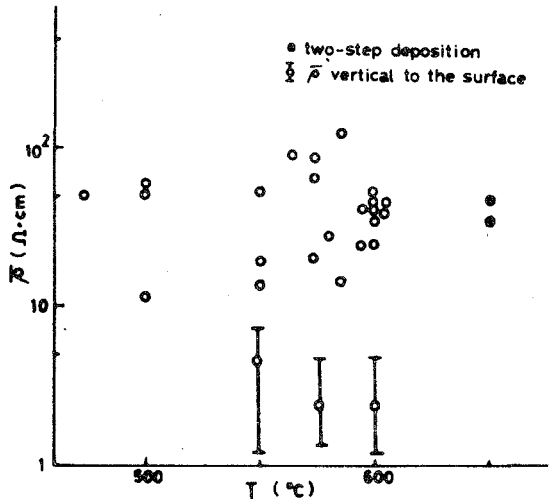

Fig. 1. Resistivity parallel and vertical to the surface vs. deposition temperature for undoped films.

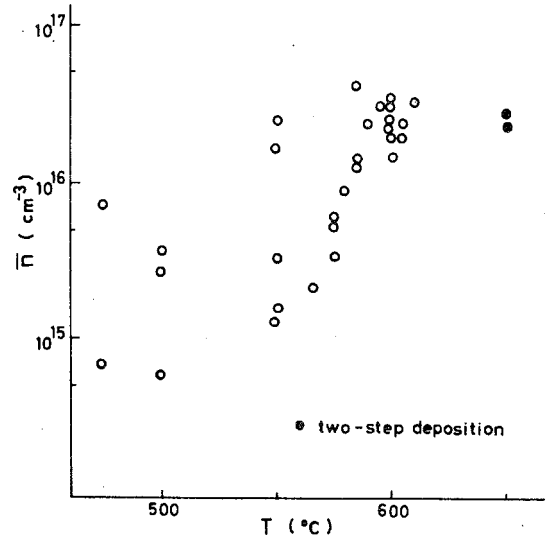

Fig. 2. Electron concentration vs. deposition temperature for undoped polycrystalline films.

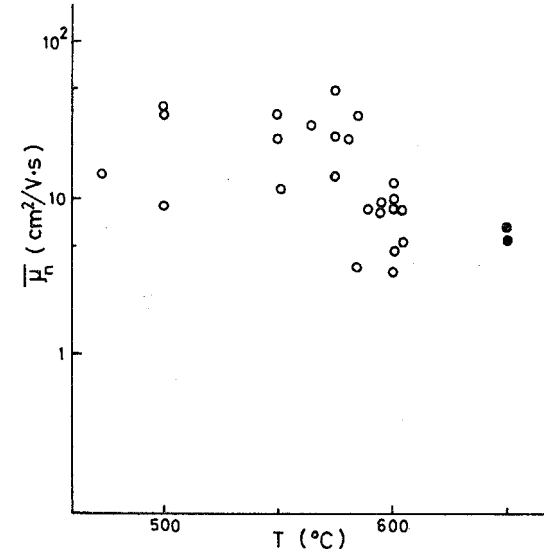

Fig. 3. Hall mobility vs. deposition temperature for undoped polycrystalline films.

area should decrease. It is assumed that a density of traps per grain boundary area remains constant. Thus, the higher the deposition temperature, the smaller the number of free carriers trapped at the grain boundary becomes causing an increase in the carrier concentration. When the deposition was carried out at more than 600°C, the deposited surface tended to become rough and have pinholes. This caused a decrease in the electron mobility of the films deposited at 600°C; probably due to the scattering of the carriers on the surfaces.

In the above figures data are also shown for two-step deposition in which a first layer was deposited at 600°C and then a second layer was deposited on it at 650°C. The observed values for the two-step deposition were similar to those of the films deposited at 600°C. This result suggests that the electrical properties of the second layers are determined mainly by those of the first layers. In other words, it indicates that each grain grows epitaxially on each of the substrates.

Furthermore, the variation of resistivity with thickness was examined. The observed values were found to be almost constant irrespective of thickness. Resistivity variation for an 18 μm thick film deposited at 575°C was also measured. It ranges from 1.2 to 4.9 $\Omega \cdot$ cm with the average value of 2.4 $\Omega \cdot$ cm.

Sulfur-doped films.—In the case of H_2S partial pressure of 6×10^{-7} atm, the carrier concentration increased with increasing deposition temperature; whereas the electron mobility increased and the resistivity decreased with the increase of deposition temperature, except around 600°C. The mobility decrease at around 600°C can be explained as the effect of free carrier scattering on the surfaces, as mentioned above.

A carrier concentration at a higher partial pressure of 3×10^{-6} atm was obtained to be about 1×10^{19} cm^{-3}, as shown in Fig. 4. It increased appreciably with deposition temperature. This suggests that saturation of the number of the carriers trapped at grain boundaries occurs. Resistivity decreased with deposition temperature, which is consistent with the increase in the grain size. In addition, electron mobility increases with deposition temperature as the value is calculated using the relationship $\bar{n}\bar{\rho}\bar{\mu} = q^{-1}$.

The variation of resistivity and electron concentration with H_2S partial pressure in the feed gas is shown in Fig. 5. It is notable that the resistivity drops rapidly at a partial pressure of 10^{-6} atm. On the other hand, the carrier concentration increased inversely. This tendency closely resembles that of polycrystalline silicon, in which the resistivity dropped drastically, about

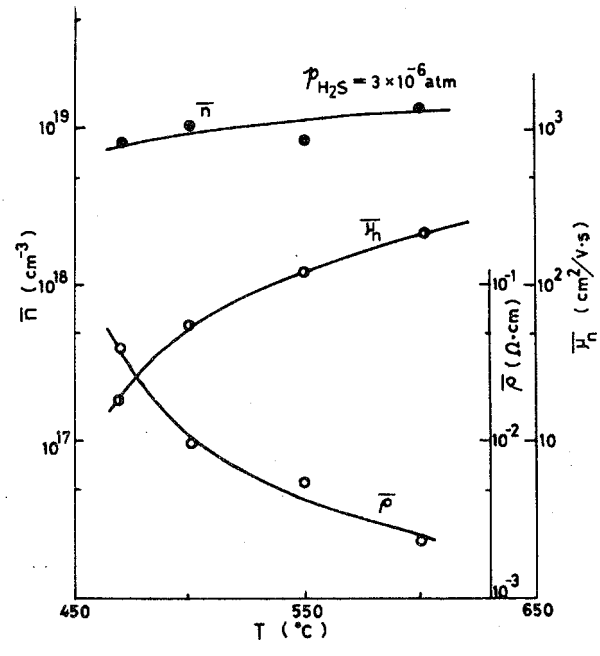

Fig. 4. Electron concentration, resistivity, and Hall mobility vs. deposition temperature for sulfur-doped films deposited at a hydrogen sulfide partial pressure of 3×10^{-6} atm.

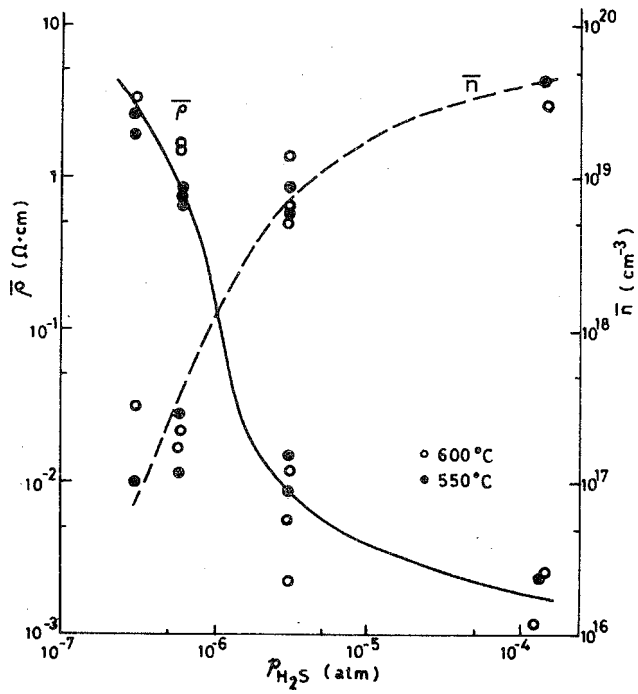

Fig. 5. Variation of resistivity and electron concentration with H_2S partial pressure in the gas phase for polycrystalline films.

five orders of magnitude (8, 9). This phenomenon can be understood as follows: As the carrier concentration decreased, the depletion-layer width around the grain boundary increased. When the depletion-layer width approached the grain size, the resistivity increased rapidly due to the trapping of almost all the carriers at the grain boundary. The smaller variation of resistivity for polycrystalline indium phosphide as compared to that of silicon is ascribed to the relatively high concentrations of residual impurities and to larger grain sizes.

The relationship between electron mobility and electron concentration for sulfur-doped films deposited at 550° and 600°C are shown as broken lines in Fig. 6. The electron mobility of polycrystalline films has a different tendency from that of the n-type single crystals shown as a solid line (10). The maximum value of the mobility is 200 cm^2/V · sec at a carrier concentration of 3×10^{19} cm^{-3}, about one-fifth that of single crystals. The lower values of the polycrystalline films deposited at 600°C than that of the films deposited at 550°C can be attributed to the scattering of the carriers at the nonuniform surfaces as already mentioned in Fig. 2.

Furthermore, the variation of the electrical properties for sulfur-doped films with thickness was measured and is shown in Fig. 7. Since the sample was attached upside down to the glass plate and etched gradually from the molybdenum side, the data at thinner thicknesses correspond to those near the as-deposited surface. As the grain size tends to increase when films become thick, the electrical properties nearer the front surface are less affected by the grain boundary. This tendency is compatible with the results shown in Fig. 7.

Barrier height at grain boundary.—In general, the electrical properties of polycrystalline films are discussed by dividing them into two regions, *i.e.*, a low resistivity region in crystallites and a high resistivity region around grain boundaries. In the case that doping level is relatively high and thus resistivity in the crystallites is sufficiently lower than that of the grain boundaries, the observed resistivity $\bar{\rho}$ is described by the following equation (6, 9, 11)

$$\bar{\rho} \propto \exp\left(\frac{\phi}{kT}\right) \qquad [1]$$

where ϕ is the barrier height.

A logarithmic plot of the resistivity *vs.* reciprocal temperature for undoped films is shown in Fig. 8. A linear relationship is obtained for samples deposited at various temperatures. Moreover, a logarithmic plot of electron mobility *vs.* reciprocal temperature was also found to vary linearly in an inverse manner. The barrier heights calculated from the figure are indicated in Table I. For films deposited at 600°C, barrier heights range from 0.2 to 0.3 eV. One barrier height for two-step deposition is almost equal to the above value. On the other hand, a smaller value of 0.081 eV is obtained for a film deposited at 500°C due to a relatively high concentration compared to other samples.

In the case of sulfur-doped polycrystalline films, a linear dependence is also obtained for a logarithmic plot of resistivity or electron mobility *vs.* reciprocal temperature. The barrier height calculated using the above equation is shown in Table I, indicating that the barrier height decreases inversely with the increase in electron concentration.

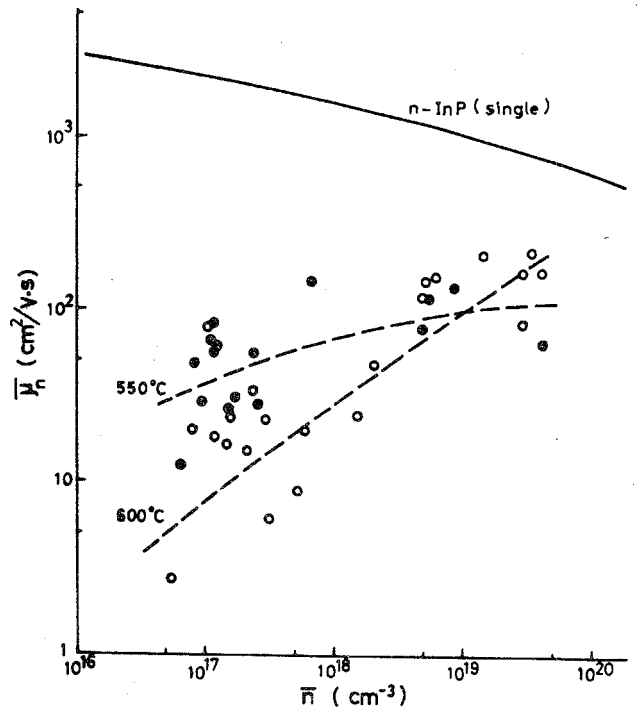

Fig. 6. Hall mobility *vs.* electron concentration for sulfur-doped polycrystalline films.

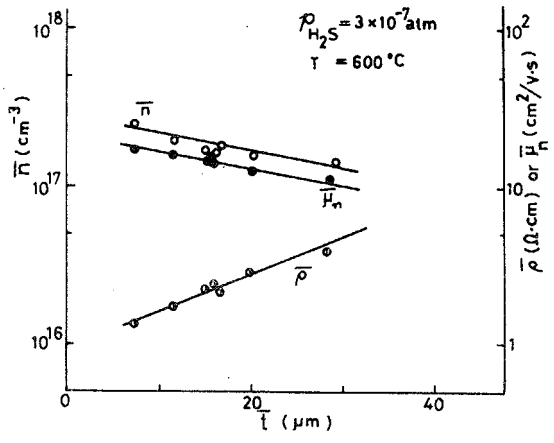

Fig. 7. Electron concentration, Hall mobility, and resistivity measured from the film surface.

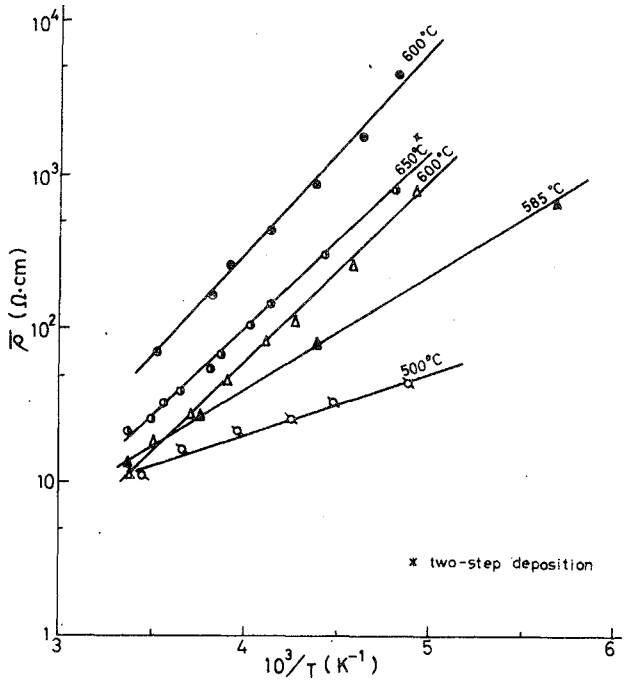

Fig. 8. Resistivity vs. reciprocal temperature for undoped polycrystalline films deposited at various temperatures.

Discussion

In general, polycrystalline films have been considered to consist of single crystallites and grain boundaries including disordered atoms. There are some different models of electronic conduction around grain boundaries, *i.e.*, grain boundaries act as a sink for impurity atoms (12) or as a trap for free carriers (6, 9). The latter model is applied for elucidating the electronic conduction properties of polycrystalline indium phosphide.

In the model, the defects at grain boundaries are assumed to generate a density of traps Nt. Therefore, free carriers are trapped, and hence grain boundaries are surrounded by a depletion region.

From Poisson's equation, assuming that only part of crystallites is depleted, the potential variation throughout the polycrystalline films can be obtained. Since the barrier height ϕ is the difference between the potential at a center of the crystallite and that at an edge of the depletion region, it can be described as (6, 9)

$$\phi = \frac{qn_t^2}{8\epsilon n_1} \qquad [2]$$

where n_1 (cm^{-3}) is the carrier concentration in the crystallite, and ϵ is the permittivity. The parameter n_t (cm^{-2}) is the number of carriers trapped at the grain boundary and is given as

$$n_t = n_1 l_2 \qquad [3]$$

where l_2 is the depletion layer width.

Kamins introduced the following equation for the observed carrier concentration $\bar{n}$ under the assumption that the Hall coefficient is additive (6)

$$\bar{n} = \frac{n_1}{1 + (l_2/l_1)^2 \exp(\phi/kT)} \qquad [4]$$

Here, l_1 is the length of the low resistivity region.

Inserting Eq. [2] and [3] into Eq. [4], the following equation concerning n_1 is obtained

$$n_1^2 - \bar{n}n_1 - A\bar{n} = 0 \qquad [5]$$

where A is

$$A = \frac{8\epsilon\phi}{el_1^2} \exp\left(\frac{\phi}{kT}\right) \qquad [6]$$

In the case of relatively high carrier concentrations, the length l_1 corresponds to the grain size. Then, A in Eq. [6] can be calculated using observed values of grain size and barrier height. Consequently, the carrier concentration in the crystallite n_1 can also be calculated from Eq. [5] and the number of carriers trapped at the grain boundary n_t from Eq. [2].

The electron concentration in the crystallites n_1 and the number of trapped carriers n_t for undoped films are also indicated in Table I. The concentration n_1 is higher than $\bar{n}$, indicating that the carrier trapping at the grain boundary is effective. The number of carriers trapped n_t tends to increase with the carrier concentration n_1 and to saturate at about 10^{12} cm^{-2}. In addition, the depletion-layer widths l_2 were found to be 1000-2000Å from Eq. [3], being approximately one order of magnitude smaller than the grain size.

On the other hand, n_1 of sulfur-doped films is almost equal to the $\bar{n}$ value, as shown in Table I. The depletion-layer widths were calculated to be far smaller than 1000Å and inversely proportional to the carrier concentrations. The number of trapped carriers n_t tends to saturate with the increase in carrier concentration and to peak at 3.3×10^{12} cm^{-2}. This value is close to that of polycrystalline silicon films (9) and is considered to be near the density of trapping states, Nt, at the grain boundary.

Summary

Electrical properties of n-type polycrystalline films have been examined using the Hall measurements. For undoped films, the carrier concentration increased with increasing deposition temperature. On the other hand, electron mobility, being about two orders of magnitude smaller than that of single crystals, was almost constant irrespective of deposition temperature and

Table I. Barrier height, electron concentration in the crystallite, and number of carriers trapped at grain boundaries for polycrystalline indium phosphide films

	Deposition temperature (°C)	Average grain size (μm)	Observed electron concentrations (cm^{-3})	Barrier height (eV)	Carrier concentrations in the crystallites (cm^{-3})	Number of electrons trapped at grain boundaries (cm^{-2})
Undoped films	600-650*	7	1.9×10^{16}	0.23	6.7×10^{16}	9.1×10^{11}
	600	7	2.3×10^{16}	0.26	9.0×10^{16}	1.1×10^{12}
	600	7	3.2×10^{16}	0.23	9.2×10^{16}	1.1×10^{12}
	585	6	1.3×10^{16}	0.15	1.8×10^{16}	3.8×10^{11}
	500	2	6.2×10^{16}	0.081	6.4×10^{16}	5.3×10^{11}
Sulfur-doped films	550	4	1.0×10^{17}	0.083	1.0×10^{17}	6.7×10^{11}
	475	1	1.6×10^{18}	0.029	1.6×10^{18}	1.6×10^{12}
	550	4	2.8×10^{18}	0.019	2.8×10^{18}	1.7×10^{12}
	600	7	2.2×10^{18}	0.019	2.2×10^{18}	1.5×10^{12}
	600	7	3.0×10^{19}	0.007	3.0×10^{19}	3.3×10^{12}

* Two-step deposition.

growth time. The resistivity parallel to the surface did not depend on deposition conditions and was one order of magnitude larger than that measured vertically to the film surface.

For sulfur-doped films, the carrier concentration increased and the resistivity decreased with increasing deposition temperature. Especially, noteworthy was the fact that resistivity increased two orders of magnitude at the H_2S partial pressure of 10^{-6} atm in the feed gas. These results are considered to be caused by the grain boundary. Electron mobility increased with the partial pressure of H_2S gas up to 200 $cm^2/V \cdot sec$ at an electron concentration of about 10^{19} cm^{-3}.

A model in which grain boundaries act as free carrier traps was utilized to elucidate the electronic transport behavior. The barrier heights for undoped films were 0.2-0.3 eV and decreased inversely with the increase in electron concentration. The density of trapping states was determined as 3×10^{12} cm^{-2}.

Acknowledgments

The authors are obliged to Dr. Takashi Tokuyama for his technical discussion and critical reading of this manuscript. This work was financed in part by the Agency of Industrial Science and Technology, Ministry of International Trade and Industry.

Manuscript submitted Aug. 31, 1976; revised manuscript received March 4, 1977.

Any discussion of this paper will appear in a Discussion Section to be published in the June 1978 JOURNAL. All discussions for the June 1978 Discussion Section should be submitted by Feb. 1, 1978.

Publication costs of this article were assisted by Hitachi, Limited.

REFERENCES

1. D. C. Reynolds, G. Leies, L. L. Antes, and R. E. Marburger, *Phys. Rev.*, **96**, 533 (1954).
2. P. Vohl, D. M. Perkins, S. G. Ellis, R. R. Addiss, W. Hui, and G. Noel, *IEEE Trans. Electron Devices*, **ed-14**, 26 (1967).
3. T. L. Chu, H. C. Mollenkopf, and S. S. C. Chu, *This Journal*, **123**, 106 (1976).
4. T. Saitoh, S. Matsubara, and S. Minagawa, *ibid.*, **123**, 403 (1976).
5. T. Saitoh, S. Matsubara, and S. Minagawa, *Jpn. J. Appl. Phys.*, **15**, 893 (1976).
6. T. I. Kamins, *J. Appl. Phys.*, **42**, 4357 (1971).
7. L. J. van der Pauw, *Philips Res. Rep.*, **13**, 1 (1958).
8. A. L. Fripp, *J. Appl. Phys.*, **46**, 1240 (1975).
9. J. Y. W. Seto, *ibid.*, **46**, 5247 (1975).
10. K. E. Brown, *Solid-State Electron.*, **17**, 507 (1974).
11. P. Rai-Choudhury and P. L. Hower, *ibid.*, **120**, 1761 (1973).
12. M. E. Cowher and T. O. Sedgwick, *This Journal*, **119**, 1565 (1972).

Thin Solid Films, *48* (1978) 339–344

INITIAL GROWTH BEHAVIOUR OF INDIUM PHOSPHIDE ON MOLYBDENUM SUBSTRATES

T. SAITOH, S. MATSUBARA AND S. MINAGAWA
Central Research Laboratory, Hitachi Ltd., Kokubunji, Tokyo (Japan)
(Received August 5, 1977; accepted September 7, 1977)

We describe the initial stages of indium phosphide growth on preferentially etched molybdenum using an In–PCl_3–H_2 reaction system. It is shown that the island size of a few microns increases while the island density decreases with growth temperature. The saturation island density is found to be 10^4–10^8 cm^{-2} and increases exponentially with the reciprocal of the growth temperature. The difference between the island saturation phenomenon that we observed and that described by the present nucleation theories may involve a smaller supersaturation in the vapour phase and the molecular diffusion of associated species on the molybdenum surface.

1. INTRODUCTION

Polycrystalline compound semiconductor films have been investigated in an attempt to fabricate inexpensive solar cells for terrestrial application[1–4]. In polycrystalline film growth on foreign substrates the nucleation growth process prevails. This process is fundamentally different from epitaxial growth on single-crystal substrates. The former process tends to form films with pinholes or openings on the substrates, resulting in a high leakage current or a short-circuit path when junctions are formed to fabricate solar cells.

To prepare pinhole-free films requires an understanding of the initial growth behaviour, including nucleation, in polycrystalline growth. Very few papers on nucleation studies of semiconductor films on foreign substrates have been reported so far except for various nucleation studies on thin films prepared by vacuum evaporation[5–8].

In this paper we give some interesting results derived from observations of a fairly early stage of indium phosphide growth on molybdenum substrates. The initial growth process is discussed in relation to the nucleation theories.

2. EXPERIMENTAL

Indium phosphide was formed on molybdenum surfaces by chemical vapour deposition using an In–PCl_3–H_2 gas system[9]. The indium source, held at 750 °C, was saturated with indium phosphide polycrystals. Hydrogen was passed through a PCl_3 bubbler and reactions occurred around the source zone of the furnace. The

resultant InCl and P_4 reacted to form indium phosphide in the deposition zone, which was held at 400–600 °C. The reaction time, almost equal to the deposition time, was adjusted to be less than a few minutes by controlling the time that hydrogen flowed through the bubbler.

The early stage of growth was found to be greatly influenced by substrate surface conditions. Three kinds of surface preparation were adopted: electropolishing to obtain flat and featureless surfaces; preferential etching in a solution of 1 part H_2SO_4 : 1 part HNO_3 : 3 parts H_2O for 30 s, followed by etching in HF acid for 1 min; mechanical rubbing of the surfaces with emery paper. Preferential etching made the substrate surfaces rough, enabling the formation of profuse nucleation sites which in turn produced pinhole-free films.

The initial growth was observed by using optical and scanning electron microscopes. The density of discrete islands, *i.e.* isolated crystalline clusters, and the island size were obtained as a function of the duration of each run and the deposition temperature.

3. RESULTS

3.1. Island formation

At a fairly early stage of growth, deposits were generally observed to consist of discrete islands although the island size depended on the preparation methods. In the case of preferentially etched substrates, which were observed to be much rougher than the electrolytically polished surfaces, hemispherical islands were obtained in a few tens of seconds, as shown in Fig. 1. The roughness is considered to reflect the conditions of fabrication of the molybdenum sheets. Almost all the islands were found to be a few microns in diameter and to exist on irregular steps or linear grooves of the substrates. In contrast, islands were not observed on the electrolytically polished surfaces up to a growth time of about 30 min.

In addition to the hemispherical islands, larger flat islands can be seen in Fig. 1. The flat islands developed in a direction parallel to the substrate surfaces with growth time and contributed to the homogeneous character of the film formation.

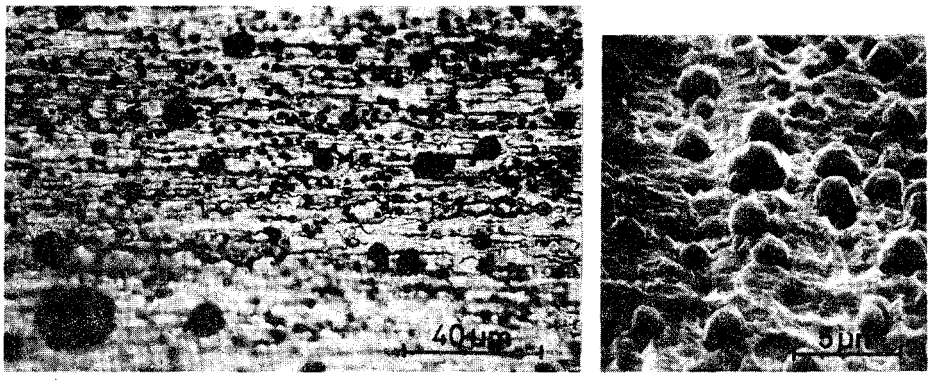

(a) (b)

Fig. 1. Island formation of indium phosphide on preferentially etched molybdenum surfaces: (a) optical micrograph; (b) scanning electron micrograph. The islands were grown at 500 °C for 30 s.

At a growth temperature of 500 °C a growth time of 10 min was sufficient to prepare homogeneous indium phosphide films on the substrates, whereas a growth time of 30 min was needed at a growth temperature of 600 °C.

Subsequently, indium phosphide growth was also carried out on the mechanically roughened surfaces. Homogeneous films were found to be formed on the substrate surfaces for growth conditions similar to those for the preferentially etched surfaces.

These results suggest that a topographical surface irregularity of the substrate is important in obtaining a high density of nucleation sites for indium phosphide.

The effect of substrate temperature on the initial growth behaviour of indium phosphide is shown in Fig. 2. Both discrete and flat islands were observed (already indicated in Fig. 1(a)). With increasing substrate temperature, the island size tended to increase and the surface density of islands decreased. The average diameters of the islands were measured and are indicated in Fig. 3 as a function of substrate temperature. The diameter increased almost exponentially with increase in substrate temperature for all growth times. This result may be associated with a decrease in the degree of supersaturation in the reacting gas with increase in substrate temperature.

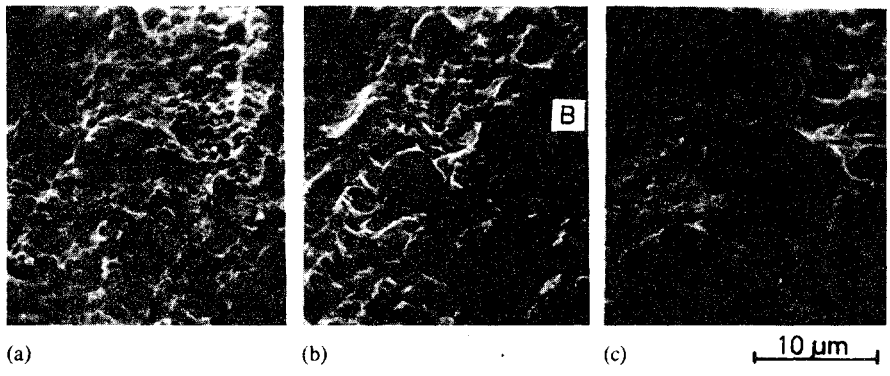

Fig. 2. Variation of island morphology with substrate temperature: (a) 500 °C; (b) 550 °C; (c) 600 °C. A and B are hemispherical and flat islands, respectively. The growth time was 60 s.

3.2. Island growth

The average island diameter was examined as a function of growth time. Islands appeared only after a short induction time (about 10 s for a substrate temperature of 500 °C and about 60 s for 600 °C) as illustrated in Fig. 4. This phenomenon may be interpreted from supersaturation theory. As the degree of supersaturation was high at lower substrate temperatures, nucleation occurred more easily than at higher growth temperatures. When nucleation began, nuclei grew rapidly and formed islands until the degree of supersaturation became close to the equilibrium value. Furthermore, after island formation the rate of growth of islands parallel to the substrate surface was almost constant irrespective of substrate temperature, as shown in Fig. 4. The growth rate was about 0.6 μm min^{-1}, which is

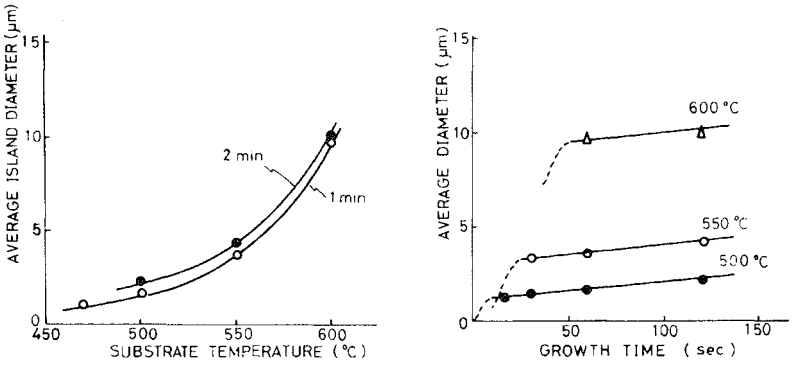

Fig. 3. Average island diameter *vs.* substrate temperature for two growth times.
Fig. 4. Variation of average island diameter with growth time.

about an order of magnitude greater than that perpendicular to the substrate surface.

Subsequently, the density of islands was counted as a function of growth time. Figure 5 indicates that the island density increased with growth time and saturated after 1 min whatever the substrate temperature. The saturation island density ranged from 10^4 to 10^8 cm^{-2}. This density is about the same order of magnitude as that for gallium arsenide nucleation on tungsten substrates[5] but is considerably lower than that for gold evaporation on vacuum-cleaved rock-salt[8].

The saturation island density was plotted (Fig. 6) as a function of reciprocal

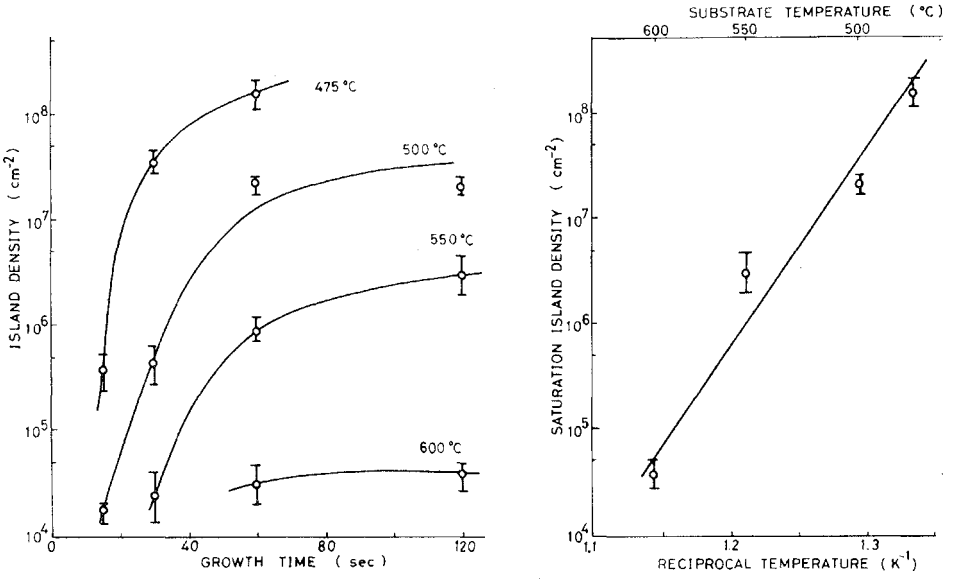

Fig. 5. Variation of island density with growth time for various substrate temperatures.
Fig. 6. The relation between saturation island density and reciprocal substrate temperature.

substrate temperature. The saturation density N_s was found to obey the relation

$$N_s = C\exp(E_A/kT) \quad (1)$$

where C is a constant, E_A is the activation energy and k the Boltzmann constant. The value obtained for E_A (3.7 eV) is considerably smaller than the value of 16.3 eV found for gallium arsenide nucleation on tungsten substrates[5].

4. DISCUSSION

As mentioned earlier, many nuclei were formed on molybdenum substrates prepared by preferential etching or mechanical rubbing with emery paper, while very few nuclei were found on the electrolytically polished surfaces. This indicates that surface roughness is significant in controlling nucleation on polycrystalline metal substrates. When an atom arrives at a nucleation site, the atom may be captured; it will reside longer at sites in rough regions than at sites in flat regions. Subsequently, other atoms will arrive at the nucleation sites from the vapour phase or from the substrate surface by diffusion, thereby forming stable nuclei and subsequently islands.

This phenomenon is similar to the nucleation of gold on the steps on cleaved rock-salt[8] or the preferential nucleation of gallium arsenide on surface scratches made on tungsten[5].

It is generally known that saturation nucleation is caused by the depletion of adatoms due to the formation of stable nuclei or to nucleus coalescence. In the case of indium phosphide, the saturation phenomenon is again found although the nuclei and subsequent islands are mostly found on preferential sites, *i.e.* etch-revealed steps, hillocks or grooves.

The saturation island density, found to be of the order of 10^4–10^8 cm^{-2}, is of the same order of magnitude as the value for gallium arsenide growth on electropolished (111) surfaces of tungsten substrates[5]. However, this is many orders of magnitude lower than the 10^9–10^{12} cm^{-2} found for vacuum-evaporated gold on the featureless surfaces of rock-salt crystals[8] (the last case was explained by the nucleation theory for incomplete condensation).

The chemical vapour deposition of indium phosphide and gallium arsenide was performed under conditions close to equilibrium. This results in a lower supersaturation than that in vacuum evaporation. A lower supersaturation is considered to lead to a lower nucleus density and a larger nucleus size. In other words, nucleation and growth on the islands play an important role in the initial growth behaviour of indium phosphide polycrystals.

It was found to be more difficult to form the nuclei and subsequent islands in the growth of indium phosphide than for gallium arsenide, presumably because of the smaller variation of free energy with deposition temperature[9]. Thus it is necessary to form preferential sites on the substrates for island formation.

From Fig. 6 it can be seen that the saturation island density increases exponentially with the reciprocal deposition temperature. The linear tendency agrees with the case of initial complete condensation in the atomistic nucleation theory[7,8]. The atomistic theory, considering such physical parameters as the rates of incidence, surface diffusion, capture and desorption, the variations in substrate

temperature and the binding energy of a critical nucleus, predicts a saturation nucleus density N_s given by

$$N_s \propto \exp\left\{\frac{2E_n}{(2n+5)kT}\right\} \tag{2}$$

where E_n is considered to be the binding energy of a cluster of n atoms[7]. This equation indicates that N_s decreases as the temperature rises, in agreement with the trend of our experimental results. The activation energy was found to be 3.7 eV from Fig. 6. The number of atoms n comprising an island should be extremely large ($> 10^9$) as the island size is as large as a few microns. As a result, the binding energy becomes extremely high—even though the binding energy is considered to be concerned with the number of atoms composing the cluster and the activation energy of surface diffusion[7]. This results from neglect of the assumption that eqn. (2) is applicable only for small clusters comparable with the atomic size. In addition, present nucleation theories, including the above theory, are based on single adatom growth (which is particularly pertinent to vacuum evaporation) without preferential nucleation sites on the substrates.

However, the high value of the activation energy may be due to the difference in growth conditions between vacuum evaporation and chemical vapour deposition in atmospheric pressure. It may also be explained if diffusion of molecular species, *i.e.* indium chloride and the phosphorus tetramer, is taken into account. The energy required for surface diffusion may be increased by a molecular diffusion mechanism.

It is also possible that some species adsorbed on the substrate surfaces hinders the surface diffusion of associated atoms or molecules. The precise nature of the associated species will be the subject of future investigation.

ACKNOWLEDGMENTS

The authors wish to thank Dr. Tokuyama for his critical reading and technical discussion of this manuscript. This work was partly supported by the Agency of Industrial Science and Technology, Ministry of International Trade and Industry.

REFERENCES

1 P. Vohl, D. M. Perkins, S. G. Ellis, R. R. Addiss, W. Hui and G. Noel, *IEEE Trans. Electron Devices*, *14* (1967) 26.
2 T. Saitoh, S. Matsubara and S. Minagawa, *Jpn. J. Appl. Phys.*, *16* (1977) 807.
3 K. J. Bachmann, E. Buehler, J. L. Shay and S. Wagner, *Appl. Phys. Lett.*, *29* (1976) 121.
4 W. D. Johnston, Jr., and W. M. Callahan, *J. Electrochem. Soc.*, *123* (1976) 1524.
5 S. J. T. Owen, G. A. Stevenson and B. Tuck, *Thin Solid Films*, *10* (1972) 31.
6 J. P. Hirth and G. M. Pound, *Condensation and Evaporation: Nucleation and Growth Kinetics*, MacMillan, New York, 1963.
7 K. J. Routledge and M. J. Stowell, *Thin Solid Films*, *6* (1970) 407.
8 B. Lewis and D. S. Campbell, *J. Vac. Sci. Technol.*, *4* (1967) 209.
9 T. Saitoh, S. Matsubara and S. Minagawa, *J. Electrochem. Soc.*, *123* (1976) 403.

Proceedings of the 9th Conference on Solid State Devices, Tokyo, 1977;
Japanese Journal of Applied Physics, Volume 17 (1978) Supplement 17-1, pp. 309–314

Polycrystalline Solar Cells on Metallurgical-Grade Silicon Substrates

Terunori WARABISAKO, Tadashi SAITOH, Haruo ITOH, Nobuo NAKAMURA and Takashi TOKUYAMA

Central Research Laboratory, Hitachi Ltd.
Kokubunji, Tokyo 185

Thin-film solar cells are fabricated by chemical vapor deposition using SiH_2Cl_2 on polycrystalline wafers pulled from metallurgical-grade silicon. An AM1 conversion efficiency of 7.3 % is obtained with a cell configuration of a 25 μm thick p-type active layer and a 0.5 μm thick n^+-type surface layer for a relatively large area of 8.3 cm^2.

Photocurrent distribution measurements reveal that the grain boundary effect is of minor importance. Higher efficiency is attainable with the same structure in cases where the photocarrier diffusion length in the active layer is improved from the obtained value, 18μm, to a level conventional in an epitaxial layer on single crystals.

§1. Introduction

A long range solution to the realization of solar cell power systems for terrestrial use is the reduction of cell costs. The basic concept of the thin-film approach is to reduce the amount of high quality, high cost semiconductor material and limit it to the active layer. Several efforts have been made to prepare silicon layers on low cost substrates.[1,2] Among the available substrates, metallurgical-grade silicon offers essential advantages over other materials. The optically active layer of a solar cell can readily be grown epitaxially on this material which is currently produced in sufficient amounts and supplied at a substantially low cost to alloy industry.

Chu[3] reported the feasibility of using metallurgical-grade silicon cast into a sheet and the resultant AM0 conversion efficiency of 3.4%. A higher conversion efficiency of 12.5%, which is comparable to conventional single crystal ones, has been demonstrated[4] in a polycrystalline solar cell using high purity silicon material. There must be an optimal combination of the simple purification of the substrate material and chemical vapor deposition (CVD) of pure silicon layers. This report deals with such processes for solar cell fabrication and problems related to the state of the art.

§2. Experimental

2.1 *Preparation of substrates*

The material used for substrates was metallurgical-grade silicon obtained in a simply purified form. The main incorporated impurities of more than 10 ppm were Al, B, C and Fe. In addition, Cu, Mg, Na and P were also included at levels of more than 1 ppm.

A rod, about 3.5 cm in diameter, was pulled by the Czochralski method, and sliced into 0.4 mm thick wafers. They were polycrystalline with millimeter grain size, and the specific resistivity was in the range between 0.0045–0.002 Ωcm. The related analytical data of the pulled polycrystal are shown in Table I. The major residual impurities were Al, B and Mn, and the rest were detectable by emission spectroscopy but found to be less than 0.005%.

Table I. Impurity levels in polycrystalline silicon wafers used for substrates of solar cells determined by emission spectroscopy.

Element	Abundance(%)
Al	0.01 −0.005
B	0.005−0.001
Cr	<0.001
Fe	<0.001
Mn	0.005−0.001
Ni	<0.005
Ti	<0.005
V	<0.001

2.2 *Cell fabrication*

The wafers were etched chemically to remove damaged surface layers prior to the following CVD process.

A p-type layer, 20–25 μm thick, and an n^+-layer, about 0.5 μm thick, were grown succesively by the hydrogen reduction of

Table II. Fabrication conditions and structural parameters of cells.

Specimen		#1	#2	#3
Growth temperature (°C)	p	1100	1100	1150
	n^+	1050	1050	1000
Film thickness (μm)	p	19.6	20.2	24.6
	n^+	0.5	0.5	0.54
Carrier concentration (cm^{-3})	p	1.3×10^{17}	1.3×10^{17}	2.9×10^{17}
	n^+	8.5×10^{19}	8.5×10^{19}	8.5×10^{19}
Cell area (cm^2)		2.91	2.60	8.29

dichrolosilane (SiH_2Cl_2) at 1100–1150°C and 1000–1050°C, respectively. Dopants used were diborane (B_2H_6) and phosphine (PH_3), and the doping levels in the layers were 1.3–$2.9\times10^{17}\,cm^{-3}$ and $8.5\times10^{19}\,cm^{-3}$, respectively. Fabrication conditions and structural parameters of each cell are summarized in Table II.

An Al alloyed contact for the back surface and a Ti/Ag grid electrode for the front surface of the wafer were applied by vacuum evaporation followed by peripheral etching to realize a mesa diode structure. In some cases, a solder coating was applied to the electrodes to reduce series resistance due to thin electrodes, and an SiO anti-reflection coating was also applied. A schematic diagram of the polycrystalline thin-film silicon solar cell is shown in Fig. 1.

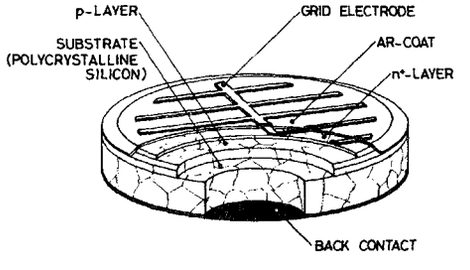

Fig. 1. Schematic diagram of a polycrystalline, thin-film silicon solar cell.

§3. Results and Discussion

3.1 *Solar cell characteristics*

a. photovoltaic characteristics

Current-voltage characteristics of solar cells were measured under illumination of an AM1 solar simulator, and the results summarized in Table III. An example of current-voltage characteristics of the cell which exhibited the highest conversion efficiency is shown in Fig. 2.

Table III. Photovoltaic parameters of cells before AR-coating measured under AM1 (100 mW/cm²) illumination.

Specimen	#1	#2	#3
V_{oc} (V)	0.508	0.516	0.582
I_{sc} (mA/cm²)	13.2	13.1	15.2
V_m (V)	0.349	0.383	0.463
I_m (mA/cm²)	11.3	11.6	12.8
Fill factor	0.59	0.66	0.67
Efficiency (%)	3.9	4.4	5.9

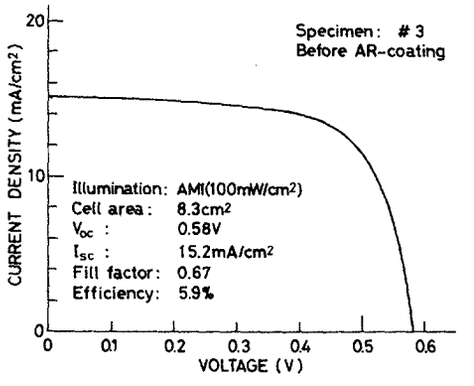

Fig. 2. Current-voltage characteristics of a polycrystalline silicon solar cell measured under AM1 (100 mW/cm²) illumination.

Without AR-coatings, open circuit voltages V_{oc} were in the range between 0.51–0.58 V, which is comparable to that of conventional single crystal cells. The short circuit current density was in the range of 13.1–15.2 mA/cm², and fill factor 0.59–0.67, which resulted in a conversion efficiency of 4.0–5.9%. The highest conversion efficiency obtained after AR-coating was 7.3% for the same cell as #3 shown in Fig. 2.

b. diode parameters

The current-voltage characteristics of a

Table IV. Diode parameters for cells best fit to eq. (1).

Specimen	#1	#2	#3
R_s (Ωcm^2)	7.53	4.60	0.24
R_{sh} (Ωcm^2)	2.76×10^3	2.66×10^3	5.61×10^2
I_{01} (A/cm^2)	2.30×10^{-11}	1.32×10^{-11}	5.21×10^{-13}
I_{02} (A/cm^2)	2.72×10^{-7}	1.94×10^{-7}	3.92×10^{-7}
n	2.00	2.00	2.20
I_L (mA/cm^2)	13.27	13.19	15.20

solar cell are often expressed by the following double exponential equation using the conventional equivalent circuit model:

$$I=-I_L+I_{01}\left\{\exp\frac{q(V-IR_s)}{kT}-1\right\}+I_{02}\left\{\exp\frac{q(V-IR_s)}{nkT}-1\right\}+\frac{V-IR_s}{R_{sh}}. \quad (1)$$

Employing the observed current-voltage characteristics, the best fit curve was generated by adjusting these parameters. The resulting values are summarized in Table IV.

The series resistance of the cell was rather high in #1 and #2. However, in #3, the improved electrode provided a lower series resistance which is quite satisfactory for a power device. Shunt resistivities were in the range between $2.7\text{–}0.56\times10^3$ Ωcm^2, which were enough for a device operated under forward bias conditions.

c. diffusion length of photocarrier

The spectral response of cells was measured under constant (15.2 $\mu W/cm^2$) light illumination, and the results for #1 and #3 are shown in Fig. 3.

The minority carrier diffusion length can readily be estimated from the spectral response curves in the wavelength range from 0.6 to 0.9 μm. A plot of $I_{sc}/\lambda\exp(-\alpha x_j)$ vs. $I_{sc}/\alpha\lambda\exp(-\alpha x_j)$ yields a linear relation within this range and the gradient of this straight line gives the diffusion length in the p-layer.[2,5] The diffusion lengths of the photocarrier thus obtained were 11 μm for #1, and 18 μm for #3.

Another method[6] was employed to estimate the photocarrier diffusion length. An electron beam was scanned across the cleaved cell surface perpendicular to the p-n junction. The electron beam induced current (EBIC) was measured as a function of the distance from the p-n junction. An example is shown in Fig. 4. The photocarrier diffusion length was estimated from the gradient of the EBIC exponential plot and the obtained value for #3 was 7.8 μm. This value, the effective diffusion length,[7] may include the effect of surface recombination at the cleaved surface, and an appropriate correction is necessary. The diffusion length varies from 7.8 to 31 μm as the surface recom-

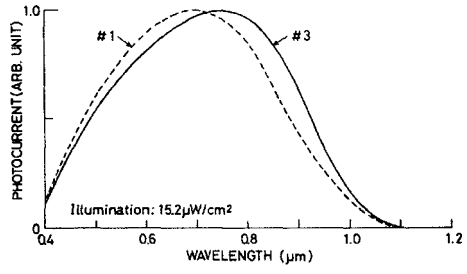

Fig. 3. Spectral response curves of solar cells measured under illumination of constant energy light at 15.2 $\mu W/cm^2$.

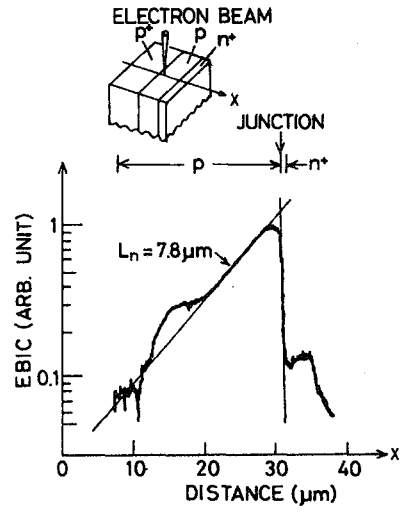

Fig. 4. Electron beam induced current in a cell (#3) measured by scanning an electron beam perpendicular to the p-n junction as indicated by the inset.

bination velocity varies between 0 and ∞ when the 25 keV electron beam penetration depth of 1.98 μm[8] is considered.

3.2 *Effect of grain boundaries*

Local distribution in the photocurrent was examined by scanning a He–Ne laser beam (.633 μm) over the surface of a solar cell with a resolution better than 20 μm. A surface photograph, the photocurrent image and a line scan are shown in Fig. 5(A), (B) and (C).

The difference in photocurrent is small between grains, and the degradation in photocurrent at grain boundaries is not very serious.

A histogram of the photocurrent was obtained by sampling the photocurrent signals followed by pulse height analysis. The resulting histogram corresponds to a 40 μm × 40 μm mesh with a 20 μm × 20 μm sampling area as shown in Fig. 6. The increase in the lower channel is due to the sampled area outside the cell and on the electrode, and the flat valley is due to the variation in photocurrent output at the cell and electrode edges.

A prime feature of this result is that there is small near-Gaussian fluctuation around the inherent photocurrent level, and there is an exponential decrease in area with decreasing photocurrent. As a consequence, the deterioration in photocurrent due to inhomogeneity and to the degradation at the grain boundaries makes minor contribution to total current output.

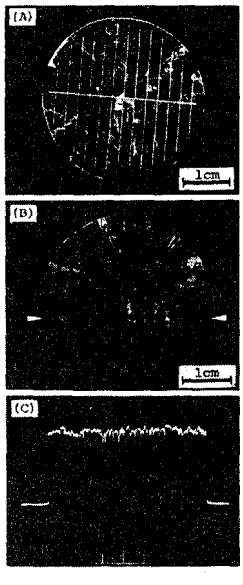

Fig. 5. (A) Surface of a polycrystalline solar cell. (B) Photocurrent image corresponding to (A), measured by scanning a He–Ne laser beam. (C) Photocurrent response of the cell corresponding to the line scan between the arrows indicated in (B).

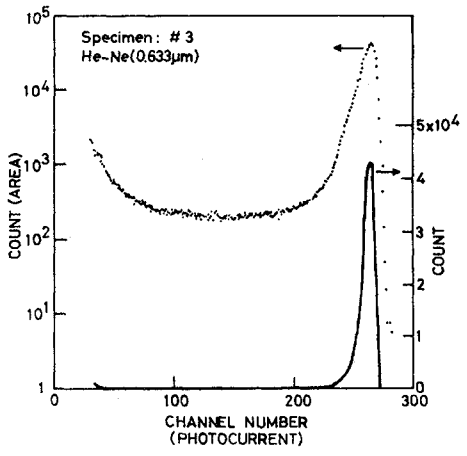

Fig. 6. Photocurrent histogram corresponding to Fig. 5(B) for 1.2×10^6 sampling points with an area of 20 μm × 20 μm in a 40 μm × 40 μm mesh.

Photocurrent degradation at grain boundaries was also observed using a scanning electron microscope. A resulting EBIC image is shown in Fig. 7 with the corresponding surface photomicrograph and a line scan.

Carrier recombination along irregular grain boundaries is large. However, there is a difference in the recombination effects within linear boundaries; one is as large as in irregular boundaries, and others are small. This may be attributed to the difference in surface recombination velocity at grain boundaries. The dependence of recombination velocity on the surface orientation at the grain boundary is of interest when considering the grain boundary effects in polycrystalline solar cells.

3.3 *Photocurrent consideration*

The cell performance is limited by lower photocurrent compared to conventional single crystal cells. In order to estimate the photocurrent in a thin-film silicon solar cell, calculations were carried out for a cell under AM1 illumination excluding the grain boundary contribution (see Appendix). The secalculations take into account the effect of the depletion layer and surface reflection. The results are shown as functions of diffusion

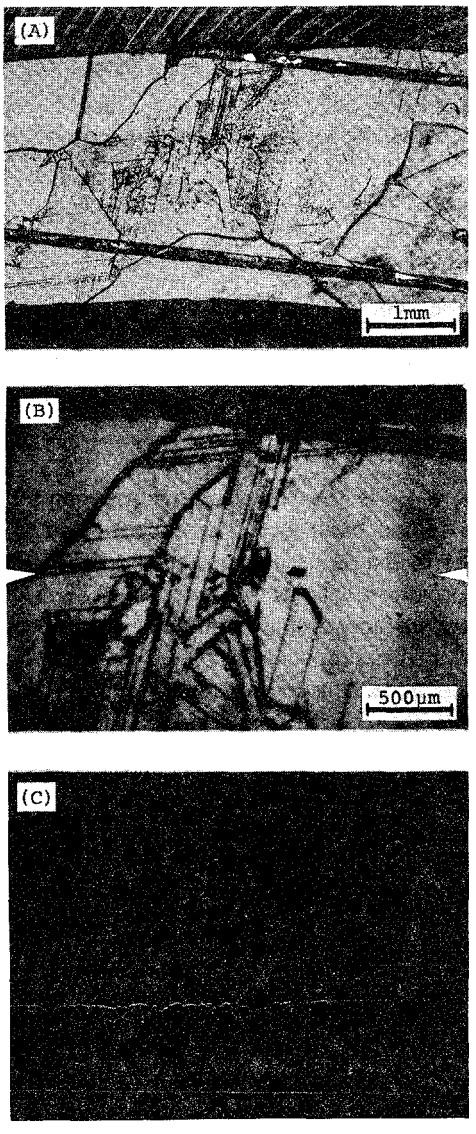

Fig. 7. (A) Surface photomicrograph of a polycrystalline solar cell. (B) Corresponding EBIC image measured with a 25 keV electron beam. (C) EBIC response corresponding to the line scan between the arrows indicated in (B).

length and carrier concentration in the active layer in Fig. 8.

The measured photocurrent, 13.2 mA/cm^2, and diffusion length, 11 μm, for the cell #1 are in good agreement with the calculation. A photocurrent of more than 25 mA/cm^2 can be projected if the photocarrier diffusion length is improved to 30 μm which is practical for conventional epitaxial layers on single crystal substrates. Under such conditions, a cell with a conversion efficiency of more than 10% is attainable even with present structures.

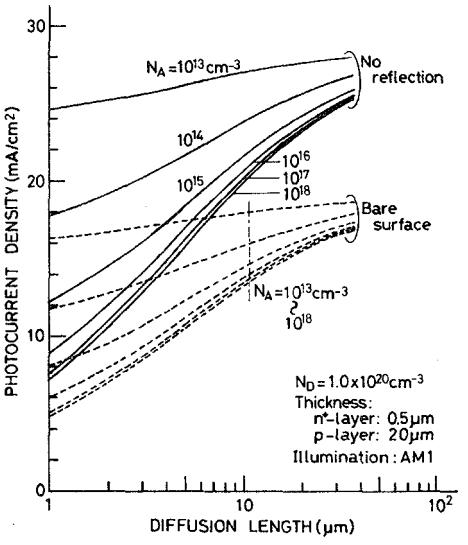

Fig. 8. Calculated photocurrent density in a thin-film solar cell as a function of photocarrier diffusion length.

§4. Conclusion

Thin-film silicon solar cells have been fabricated on polycrystalline silicon substrates prepared by pulling from metallurgical-grade material with the Czochralski method. One feature of this approach is the combination of low cost silicon substrates and high quality thin-film CVD processes.

An AM1 conversion efficiency as high as 7.3% was obtained for a cell with a 25 μm thick active layer and an 8.3 cm^2 cell size.

The photovoltaic parameter that restricts cell performance is the low short circuit current. This resulted from the unsatisfactory diffusion length of the photocarrier in the active layer. On the contrary, grain boundaries do not play a serious role in photocurrent degradation, regardless of the possible contribution to lowering the shunt resistance of the cell.

Acknowledgements

The authors are indebted to Ekyo Kuroda of our Laboratory for preparing the polycrystalline rod with the Czochralski method.

This work has been supported financially by the Agency of Industrial Science and Technology, Ministry of International Trade and Industry.

Appendix

According to the model shown in Fig. A-1, the carrier generation rate $G(\lambda, x)$ at x when illuminated by light with wavelength λ is given by:

$$G(\lambda, x)=\phi_0(\lambda)\{1-R(\lambda)\}\alpha(\lambda)\exp\{-\alpha(\lambda)x\}, \quad (A\cdot 1)$$

where $\phi_0(\lambda)$ is the photon flux of the solar radiation,[9] $R(\lambda)$ the reflectivity at cell surface,[10] $\alpha(\lambda)$ the light absorption coefficient of silicon.[11]

Assuming that the collection efficiency for the carriers generated in the depletion layer is unity, and the collection efficiency for the minority carriers in both n^+ and p regions decreases exponentially with the distance from the depletion layer edge, the quantum efficiency of each layer is given as follows:

$$\eta_d=(1-R)[\exp(-\alpha d)-\exp\{-\alpha(d+W)\}], \quad (A\cdot 2)$$

$$\eta_n=\frac{\alpha(1-R)}{\alpha-1/L_p}\left[\exp\left(-\frac{d}{L_p}\right)-\exp(-\alpha d)\right], \quad (A\cdot 3)$$

$$\eta_n=\frac{\alpha(1-R)\exp\{-\alpha(d+W)\}}{\alpha+1/L_n}\times\left[1-\exp\left\{-\left(\alpha+\frac{1}{L_n}\right)t\right\}\right], \quad (A\cdot 4)$$

where L_p and L_n are the minority carrier diffusion lengths in the n^+ and p layer, respectively. The thickness of the depletion region, x_n and x_p, in the n^+ and p layer, respectively, is given by:

$$x_n=\left\{\frac{2k_s\varepsilon_0 kTN_A}{q^2(N_A+N_D)N_D}\ln\frac{N_AN_D}{n_i^2}\right\}^{1/2}, \quad (A\cdot 5)$$

$$x_p=\left\{\frac{2k_s\varepsilon_0 kTN_D}{q^2(N_A+N_D)N_A}\ln\frac{N_AN_D}{n_i^2}\right\}^{1/2}, \quad (A\cdot 6)$$

where symbols have their ordinary meanings.

The total photocurrent J_T is then given by:

$$J_T=q\int_0^{\lambda_G}\phi_0(\lambda)\{\eta_d(\lambda)+\eta_n(\lambda)+\eta_p(\lambda)\}d\lambda, \quad (A\cdot 7)$$

where λ_G is the wavelength corresponding to the silicon band gap. The contribution of n^+-layer to the photocurrent is neglected in Fig. 8. Photocurrent from n^+-layer is 0.89 mA/cm^2 (bare surface) and 1.43 mA/cm^2 (no reflection) under the same conditions shown in Fig. 8 when L_p is an overestimated value of 0.1 μm.

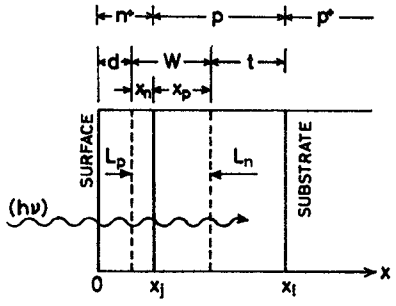

Fig. A-1. A model for the calculation of photocurrent.

References

1) T. L. Chu, S. S. Chu, K. Y. Duh and H. I. Yoo: *Proc. 12th IEEE Photovoltaic Specialists Conf., November, 1976*, p. 74.
2) T. Saitoh, T. Warabisako, H. Itoh, N. Nakamura, H. Tamura, S. Minagawa and T. Tokuyama: Japan. J. appl. Phys. **16** (1977) Suppl. 16-1, p. 413.
3) T. L. Chu and K. N. Singh: Solid-State Electronics **19** (1976) 837.
4) H. Fischer and W. Pschunder: *Proc. 12th IEEE Photovoltaic Specialists Conf., November, 1976*, p. 86.
5) L. M. Terman: Solid-State Electronics **2** (1961) 1.
6) H. Higuchi and H. Tamura: Japan. J. appl. Phys. **4** (1965) 316.
7) L. Jastrzebski, J. Lagowski and H. C. Gatos: Appl. Phys. Letters **27** (1975) 537.
8) D. B. Wittry and D. F. Kyser: J. appl. Phys. **38** (1967) 375.
9) Publication C.I.E. No. 20 (TC-2.2) (1972); and H. Brandhorst, J. Hickey, H. Curtis and E. Ralph: NASA TM X-71771 (1975).
10) H. R. Philipp and E. A. Taft: Phys. Rev. **120** (1960) 37.
11) W. C. Dash and R. Newman: Phys. Rev. **99** (1955) 1151.

208 グラファイト基板上に作成した多結晶Si薄膜太陽電池

伊藤晴夫　斉藤忠　厳迫光紀　中村信夫　徳山巍
（日立製作所　中央研究所）

1.序　グラファイトは基板材料として安定であり，熱膨張係数がSiに近く，Si膜との密着性やぬれ性もよいという特徴を有する。われわれは，このグラファイト基板上にCVD法で形成した多結晶Si膜を帯溶融法により再結晶化し，この上に太陽電池を作成する研究を行っている[1][2]が，本発表では変換効率6％を得たセルの特性について主として述べる。

2.セルの構成　まず，25×100×1㎜のグラファイト板上に，$SiHCl_3$の水素還元法により約200μm厚のBドープ多結晶Siを形成し，これに帯溶融処理を加え多結晶Si層の再結晶化を行ないp^+-Si／グラファイト基板を作成した。この時，高周波加熱炉を用い，溶融帯域幅8～12㎜とし，炉中を速度3㎜/minで移動させた。その結果，コイルの位置，グラファイト治具の大きさと形状，移動の滑らかさ等が再結晶化膜の厚さや幅などの均一性に影響を及ぼすことが明らかになった。条件を最適化することにより，幅16～19㎜，長さ60～80㎜（面積10～15cm^2）のほぼ均一な再結晶化膜を得た。再結晶化膜は，幅200μm～2㎜，長さ2㎜～数cmのデンドライト結晶からなる。この多結晶Siを基板とし成長接合法によりp-n接合（p層；20μm厚，$p \sim 10^{17} cm^{-3}$，　n^+層；0.7～0.9μm厚，$n \sim 5 \times 10^{19} cm^{-3}$）を形成し，さらに$n^+$層表面にくし状電極（Ag/Ti）を設け，反射防止膜としてSiOを蒸着して太陽電池を作成した。

3.セルの特性と考察　セル特性の評価として，AM1ソーラーシミュレーターを用い光電流-電圧特性ならびに光電変換効率を，定エネルギー分光器で分光感度特性を，レーザー光走査により光電流分布を測定した。

図1に，面積15.4cm^2の太陽電池の光電流-電圧特性を示す。特性値は，短絡電流19.4 mA/cm^2（照射光強度100mW/cm^2），開放電圧0.54 volt，曲線因子0.57，変換効率6.0％である。前回の報告[1]に比べ特性が向上している要因のひとつは；n^+層側の電極をAl電極からAg/Ti電極へ変更した点にある。このためリーク電流が減少し等価並列抵抗（Rsh）が増大し，さらに等価直列抵抗（Rs）も小さくなって，曲線因子が増大した。　また，分光感度特性の長波長側の波長依存性からp層中の少数キャリアの拡散長が数μmと求められたが，この値は，アルミナ基板セル[3]の1μmに比べ大きく，多結晶Si基板セル[4]の8～9μmにほぼ匹敵する。

図2は，レーザー光走査による光電流分布の輝度変調像と光電流分布曲線である。明るい場所が光電流出力の大きいことを示している。図中魚骨状の黒色部分は表面電極に対応し，扇状に拡がる黒い筋は結晶粒界の部分である。図2(b)によれば，光電流の平均的なばらつきは10～20％程度であるが，1箇所40％も減少している部分が見られる。これは，グラファイト基板を用いているために生じたSiC粒子が再結晶化膜中に内蔵されているためであると考えられる。

本研究は通産省工技院「サンシャイン計画」の一環として行なわれたものである。

1) 伊藤他　第37回（51年秋）応物　2a-W-7
2) 〃　〃　第24回（52年春）応物　26a-N-10
3) 斉藤他　第37回（51年秋）応物　2a-W-6
4) 〃　〃　第24回（52年春）応物　26a-N-11

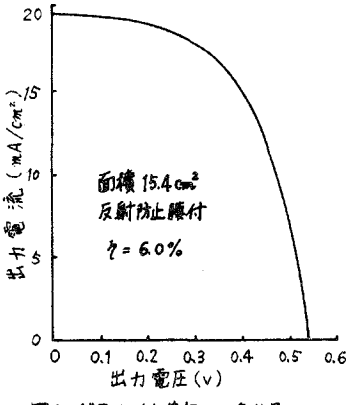

図1. グラファイト基板上の多結晶Si太陽電池の出力特性

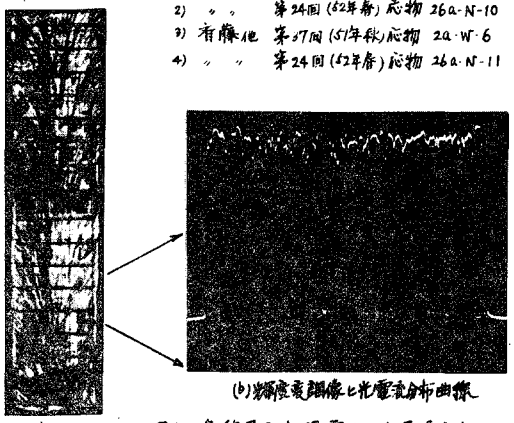

(a)輝度変調像　(b)輝度変調像と光電流分布曲線

図2. 多結晶Si太陽電池の光電流分布

Digest of Tech. Papers The 9th Conf. on Solid State Devices, Tokyo

B—5—1

Polycrystalline Solar Cells on Metallurgical-Grade Silicon Substrates

T. Warabisako, T. Saitoh, H. Itoh, N. Nakamura, and T. Tokuyama

Central Research Laboratory, Hitachi Ltd.

Kokubunji, Tokyo

The cell configuration of a thin but high quality active layer on low cost substrates is the most practical approach for cost reduction in fabricating silicon solar cells. Several efforts have been made to prepare silicon layers for epitaxial growth on various substrates.[1), 2)] Recently, the feasibility of low cost silicon substrates has been demonstrated[3)] with 3-6% efficiencies obtained for relatively large cell areas($\sim 30cm^2$). In this paper, thin film solar cells are fabricated on metallurgical-grade silicon substrates to confirm the feasibility of this approach. In addition, a method of evaluating polycrystalline solar cells is described.

The material used for substrates was metallurgical-grade silicon. A rod, about 3.5cm in diameter, was pulled by the Czochralski method, and sliced into 0.4mm thick wafers. They were polycrystalline with millimeter grain size, and were degenerated p-type wafers with a specific resistivity of 1.6×10^{-3}ohm·cm. As for included impurities, the related analytical data are shown in Table 1. The wafer surfaces were chemically etched to remove damaged layers. A 25μm thick p-type and a 0.5μm thick n-type layer with doping levels of $2.5\times10^{17}cm^{-3}$ and $5\times10^{19}cm^{-3}$ were grown successively on the wafer by decomposition of SiH_2Cl_2 at 1150°C and 1000°C, respectively. A Ti/Ag grid electrode was applied to the front surface and an Al electrode to the rear surface by vacuum evaporation followed by soldered overcoatings. Then, they were subjected to peripheral etching to realize a mesa diode structure. An SiO anti-reflection coating was applied by vacuum evaporation in some cases. An example of the surface of a cell is shown in Fig.1.

Typical current-voltage characteristics of this solar cell measured under illumination by an AM2($73mW/cm^2$) solar simulator are shown in Fig.2. A conversion efficiency of 5.7% was obtained with an open circuit voltage of 0.57V, short circuit current of $11.1mA/cm^2$ and fill factor of 0.66 for an $8.3cm^2$ cell area without anti-reflection coating. The conversion efficiency was improved to 7.3% after the application of an SiO film.

Spectral response curves for bare surface cells reached a maximum at around 0.7μm as shown in Fig.3. The diffusion length of the photocarrier in the p-layer, estimated from the spectral response curve,[4)] was around 10μm. This agreed well with the value, 7.8μm, measured by scanning an electron beam across the cleaved surface perpendicular to the junction.[5)]

Spacial distribution of the photocurrent was measured by scanning laser and/or electron beam, and an example of results is shown in Fig.4. This corresponds to the entire surface of the solar cell shown in Fig.1. A line scan along the indicated arrows is also shown. The histogram of photocurrent, shown in Fig.5, was obtained by sampling the photocurrent followed by pulse height analysis. These results indicate that photocurrent fluctuations are small around an inherent current level and the area with less photocurrent decreases exponentially with some degradation constant. Current suppression along the grain boundaries is rather drastic. However, the contribution of this effect to the total photocurrent is of minor importance. It is essential to elevate the inherent photocurrent level of the cell in order to improve cell performance.

Concerning the photocurrent, computer simulation was carried out for a simple model where the photocarrier collection efficiency decreases exponentially with the distance from the edge of the depletion layer and is unity in the depletion layer. The photocurrent for boundary conditions similar to the structural parameters of this cell was calculated to be 20mA/cm^2 under AM1 spectral irradiation. This is in good agreement with the measured values. To achieve a conversion efficiency of more than 10%, a photocurrent of more than 25mA/cm^2 is required, which corresponds to the photocarrier diffusion length of about 30μm. The value will be attainable even with the present structure.

This work is contracted with the Agency of Industrial Science and Technology, M.I.T.I., as a part of the National R&D Program "Project Sunshine".

References:

1) T. L. Chu et al., J. Electrochem. Soc., 123, 106(1076).
2) T. Saitoh et al., Japan. J. Appl. Phys., 16(suppl. 16-1), 413(1977).
3) R. U. D'Aiello, Semiconductor Silicon 1977(Proc. of the 3rd Int'l Symposium on Silicon Materials Science and Technology) pp.836(1977).
4) L. M. Terman, Solid-State Electronics, 2, 1(1961).
5) H. Higuchi et al., Japan. J. Appl. Phys., 4, 316(1965).

Table 1 Analytical data of the silicon wafers used for substrates.

Element	Al	B	Cr	Fe	Mn	Ni	Ti	V
Abundance(wt%)	0.01-0.005	0.005-0.001	<0.001	<0.001	0.005-0.001	<0.005	<0.005	<0.001

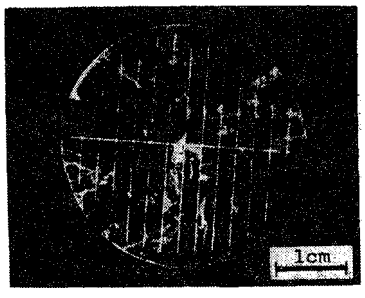

Fig.1 Surface of a polycrystalline silicon solar cell(dark image).

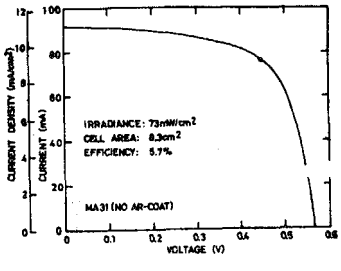

Fig.2 Current-voltage characteristics of a polycrystalline silicon solar cell.

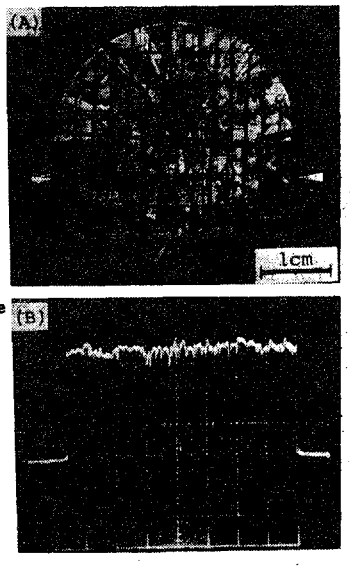

Fig.4 Photocurrent distribution of the cell shown in Fig.1 measured with (A) a scanning He-Ne laser, and (B) a line scan between arrows.

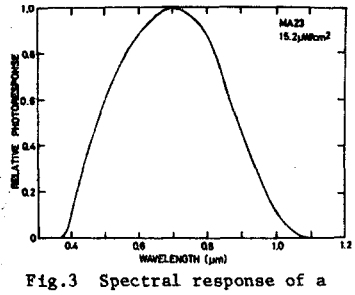

Fig.3 Spectral response of a polycrystalline silicon solar cell.

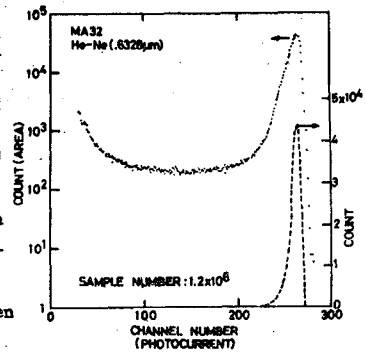

Fig.5 Photocurrent histogram corresponding to Fig.4 (A).

POLYCRYSTALLINE SOLAR CELLS FABRICATED ON METALLURGICAL SILICON SUBSTRATES*

T. WARABISAKO, T. SAITOH, H. ITOH, N. NAKAMURA, and T. TOKUYAMA

Central Research Laboratory, Hitachi Ltd.
Kokubunji, Tokyo 185, Japan

Summary

One practical approach to reducing solar cell cost is the fabrication of thin-film active layer on polycrystalline silicon substrate prepared from metallurgical-grade material. A cell of 8.3cm^2 area is found to exhibit an AM1 conversion efficiency of 7.3% when a 25μm thick p-type active layer is grown on a CZ-pulled polycrystalline silicon wafer by a CVD process using SiH_2Cl_2, followed by the formation of a grown junction with a 0.54μm thick n^+-layer.

A semiquantitative method measuring cell area as a function of photocurrent level is introduced to reveal the inhomogeneity of polycrystalline solar cells. From the measurement of photocurrent distribution, grain boundaries are found to detract slightly from cell performance in our thin-film cells whereas the short minority carrier diffusion length of 11-18μm in the active layer remains a major factor to be improved.

* Work supported by the Agency of Industrial Science and Technology, Ministry of International Trade and Industry(Japan), as a part of the national R&D program "SUNSHINE PROJECT".

1. Introduction

Fabrication of silicon thin-film solar cells by direct deposition onto foreign substrates has been attempted(1) to reduce cell cost for terrestrial application. However, obtained conversion efficiencies have been unsatisfactory because of the small grain size of the deposited silicon films.

In recent years, several efforts have been made to fabricate a thin silicon layer on various kinds of foreign substrates in order to grow a photovoltaic active silicon layer(2, 3). Among the materials lending themselves to this process, metallurgical-grade silicon offers essential advantages since it has chemical and physical compatibility with the active silicon layer for photovoltaic energy conversion. In addition, it is currently supplied to alloy industries at a substantially low cost. The possibility attaining a practical conversion efficiency of 3.4% using this material as a substrate has been demonstrated by Chu et al.(4).

This paper also describes another practical method of fabricating thin-film silicon solar cells on polycrystalline substrates which are prepared from such metallurgical grade material. It also presents a characterization and a simple method for effectively evaluating polycrystalline solar cells.

2. Fabrication of Solar Cells

2.1 Polycrystalline silicon substrates

The starting material was metallurgical-grade silicon of 99.5% purity. Major incorporated impurities were Al, B, Cu, Fe, Mg, Na and P.

A polycrystalline rod of about 3.5cm in diameter was obtained by the conventional Czochralski method with a pulling rate of several mm/min, and was sliced into 0.4mm thick wafers. An example of the sliced wafers is shown in Fig.1. They were polycrystal of millimeter grain size. Most of the grains were composed of several subgrains separated by linearly extending boundaries such as twin boundaries.

Residual impurities after crystallization were analyzed by emission spectroscopy. The results are shown in Table I. As a result of effective segregation, most of the metallic impurities were supressed substantially during the crystal growth. Because of remaining Al and B, the wafers were

p-type, and the resistivity was around 0.003Ω·cm.

Prior to the following film deposition process, the surface of the wafer was mirror-etched to remove cutting damage.

2.2 Cell fabrication

A schematic diagram of the solar cell is shown in Fig.2.

A p-type active layer and an n^+-type surface layer were chemically vapor deposited successively by hydrogen reduction of SiH_2Cl_2 with dopants at levels of 1.3-2.9x10^{17}boron/cm^3 and 8.5x10^{19}phosphorus/cm^3, respectively. Deposition conditions and related geometrical data are summarized in Table II.

Electrodes used were Al-alloyed for the back, and Ti/Ag grid for the front. The multilayered structure was then peripherally etched to realize a mesa-diode structure. In some cases, a solder over-coat was applied to the electrodes; an SiO anti-reflection coating was also applied. An example of the solar cells thus fabricated is shown in Fig.3.

3. Experimental Results and Discussion

3.1 Photovoltaic characteristics

Photovoltaic conversion characteristics were measured under AM1 illumination of a xenon-arc type solar simulator, and the results for cells before AR-coatings are summarized in Table III. The J-V relation of the cell which exhibited the maximum conversion efficiency of 7.3% after application of an anti-reflection coating is shown in Fig.4.

Using the conventional equivalent circuit model including the leakage component through shunt resistance, J-V characteristics are often expressed by the following double exponential equation;

$$J = -J_L + J_{01}\left[\exp\frac{q(V-JR_s)}{kT} - 1\right] + J_{02}\left[\exp\frac{q(V-JR_s)}{nkT} - 1\right] + \frac{V-JR_s}{R_{sh}}, \quad (1)$$

where, notations have their ordinary meanings. Employing the observed values, the best fit curves were generated by adjusting diode parameters in Eq.(1). The resulting diode parameters are summarized in Table IV.

As for the solar cell characteristics, open circuit voltage is comparable to that of a conventional single crystalline solar cell, whereas

short circuit current density is somewhat low compared with the value estimated from the thickness of the active layer. Series resistivity is in a satisfactory level, and shunt resistivities are high enough for forward operation. However, the recombination current level is rather high, which implies a short minority carrier lifetime in the active layer.

A typical spectral response curve of solar cells measured under illumination of constant energy light is shown in Fig.5. The minority carrier diffusion lengths estimated from the spectral response curves were in the range 11-18μm.

3.2 Grain boundary effect

A photocurrent image obtained by scanning a confined He-Ne laser beam (λ=0.633μm) over the lower half of the cell shown in Fig.3 is shown in Fig.6 with a line scan mode of photocurrent. The dark lines in the figure correspond to grid electrodes. Although there is remarkable brightness-difference in the photocurrent image between grains, the actual difference is less than 15% of the avarage photocurrent. The degradation in photocurrent along grain boundaries is shown to be very small.

In order to obtain some statistical information on photocurrent distribution, cell area was estimated semiquantitatively as a function of current level. The experiment was carried out by scanning a He-Ne laser spot of about 20μm in diameter over the cell surface, and by sampling photocurrent corresponding to 40μm-40μm mesh points on the cell, followed by pulse height analysis. An example of resulting current histogram for the cell shown in Fig.3 is shown in Fig.7, which corresponds to about one million sampled points. The increase in lower current level is due to the sampled points outside the cell and on the electrode, and the flat valley is caused by the rapid change in photocurrent at the cell or electrode edges.

In Fig.7, there is small Gaussian-like fluctuation arround an inherent (or maximum frequency) photocurrent level, and superimposed on this, an exponential decay in area with decreasing photocurrent. The fluctuation is probably due to the difference in crystal orientation and electronic properties in each grain. The exponential decay may be caused as a result of integrating many levels of degradation in photocurrent along grain boundaries. This decay constant β could be used as an empirical factor to describe the inhomogeneity of polycrystalline solar cell including the degradation effect along grain boundaries, and to compare polycrystalline

material prepared in different ways.

If we assume the photocurrent frequency distribution as shown in Fig.8, we can estimate the per cent degradation of the photocurrent caused by grain boudaries. The total photocurrent is obtained by integrating current multiplied by area or photocurrent frequency,

$$I = \int_0^{i_m} iS \, di = \frac{S_0}{\beta^2} + \frac{S_m}{\beta}(i_m - \frac{1}{\beta}). \tag{2}$$

For the idealized single crystal case, the total photocurrent is the inherent(or maximum frequency) current i_m multiplied by the total area,

$$I' = i_m \int_0^{i_m} S \, di = \frac{1}{\beta}(S_m - S_0). \tag{3}$$

Then, the current ratio R of the inhomogeneous case to the ideal case is given as;

$$R = \frac{I}{I'} = \frac{i_m S_m - \frac{1}{\beta}(S_m - S_0)}{i_m(S_m - S_0)}, \tag{4}$$

and when the gradient is large, the ratio is reduced to the following simple equation;

$$R = 1 - \frac{1}{i_m \beta}. \tag{5}$$

Employing the measured values, i.e. i_m= 265ch(0.229A/W) and β=0.133ch^{-1}, one can obtain R=0.97. Consequently, the deterioration in photocurrent which can be directly attributed to grain boundaries is estimated to be only 3% at the wavelength of the probe-light.

3.3 Consideration on photocurrent level

In a thin silicon film, e.g. 20μm, more than 80 per cent of the solar radiation energy is absorbed in generating hole-electron pairs(5). However, available photocurrent is a function of the cell configuration and the electrical properties of the film.

Employing a simple model of depletion layer approximation, the photocurrent of a cell with a 20μm thick active layer and a 0.5μm thick surface layer was calculated as a function of carrier density and minority carrier diffusion length in the active layer. In the calculation, the collection

efficiency of the minority carrier generated in the depletion layer is assumed to be unity. Those of bulk p- and n-type layers are assumed to decrease exponentially with the distance from the nearest depletion edge. Surface reflection with wavelength(6) are also incorporated in the calculation. The results for the AM1 condition(7) are shown in Fig.9.

An observed combination of short circuit current of 13mA/cm^2 and the minority carrier diffusion length of 11μm shows a good agreement with the calculated value. Somewhat unsatisfactory short circuit current is directly attributed to the short minority carrier diffusion length in the active layer, and probably to the lifetime-killing impurities incorporated in the film during the deposition process.

4. Conclusion

Polycrystalline silicon thin-film solar cells have been fabricated on wafers prepared from metallurgical-grade material.

An AM1 conversion efficiency as high as 7.3% was attained in a cell with a 25μm thick active layer and a 0.5μm thick surface layer, both prepared by chemical vapor deposition of SiH_2Cl_2.

An empirical decay factor was introduced to describe the deterioration effect in the photocurrent directly caused by the grain boundaries. The current degradation due to grain boundaries was estimated to be less than 3% under 0.6μm wavelength light. Considering the solar spectrum and the spectral response of solar cells, grain boundaries make only a minor contribution to the detraction of cell output current in our thin-film, polycrystalline silicon solar cell. A higher conversion efficiency can be projected by enhancing the minority carrier diffusion length in the epitaxially grown layers, probably by suppressing the level of undesired lifetime-killing impurities in the substrate.

Acknowledgement

The authors are indebted to Mr. Ekyo Kuroda for the crystal growth from metallurgical-grade silicon material.

References

(1) T.L.Chu, H.C.Mollenkopf and S.S.Chu, J. Electrochem. Soc., 123, 106 (1976); and ibid., 122, 1681(1975).

(2) T.L.Chu, S.S.Chu, K.Y.Duh and H.I.Yoo, Proc. 12th IEEE Photovoltaic Specialists Conf., Nov.(1976)pp.74.

(3) T.Saitoh, T.Warabisako, H.Itoh, N.Nakamura, H.Tamura, S.Minagawa and T.Tokuyama, Jap. J. Appl. Phys., 16, Suppl.16-1(1977)pp.413; and T.Warabisako and T.Saitoh, IEEE Trans. on Electron Devices, ED-24, 446(1977).

(4) T.L.Chu and K.N.Singh, Solid-State Electronics, 19, 837(1976).

(5) J.G.Fossum, Solid-State Electronics, 19, 269(1976).

(6) H.R.Philipp and E.A.Taft, Phys. Rev., 120, 37(1960).

(7) Publication C.I.E., No.20(TC-2.2)(1972); and H.Brandhorst, J.Hickey, H.Curtis and E.Ralph, NASA TM X-71771(1975).

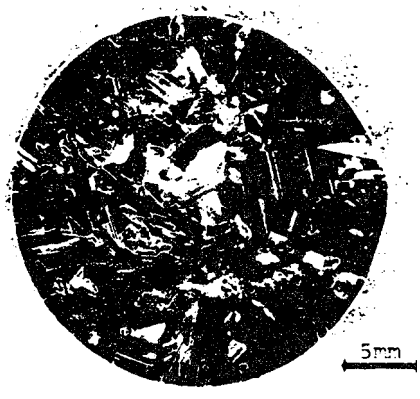

Fig. 1. Surface photograph of a polycrystalline wafer prepared from metallurgical-grade silicon.

Table I. Impurity levels in polycrystalline silicon wafers used for substrates of solar cells determined by emission spectroscopy.

Element	Abundance(ppm)
Al	50 - 100
B	10 - 50
Cr	<10
Fe	<10
Mn	10 - 50
Ni	<50
Ti	<50
V	<50

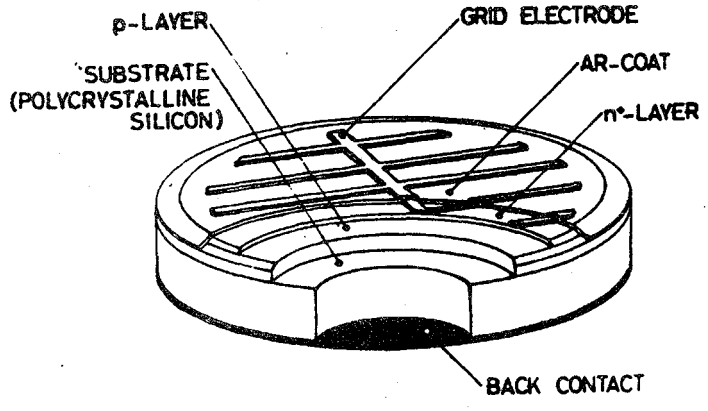

Fig. 2. Schematic diagram of a thin-film polycrystalline silicon solar cell.

Table II. Fabrication conditions and structural parameters of cells.

Specimen		#1	#2	#3
Growth temp.(°C)	p	1100	1100	1150
	n^+	1050	1050	1000
Film thickness(μm)	p	19.6	20.2	24.6
	n^+	0.50	0.50	0.54
Carrier conc.(cm^{-3})	p	1.3×10^{17}	1.3×10^{17}	2.9×10^{17}
	n^+	8.5×10^{19}	8.5×10^{19}	8.5×10^{19}
Cell area(cm^2)		2.91	2.60	8.29

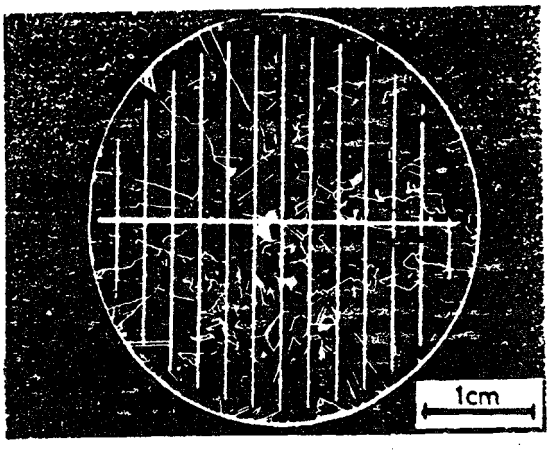

Fig. 3; Surface of a thin-film, polycrystalline silicon solar cell.

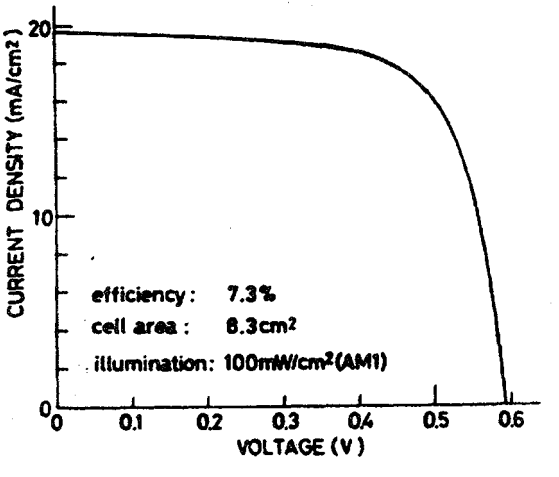

Fig. 4. Current-voltage characteristics of a polycrystalline solar cell measured under AM1 condition.

Table III. Photovoltaic characteristics of solar cells before AR-coating measured under AM1($100mW/cm^2$) illumination.

Specimen	#1	#2	#3
V_{oc}(V)	0.508	0.516	0.582
J_{sc}(mA/cm^2)	13.2	13.1	15.2
V_m (V)	0.349	0.383	0.463
J_m (mA/cm^2)	11.3	11.6	12.8
Fill factor	0:59	0.66	0.67
Efficiency(%)	3.9	4.4	5.9

Table IV. Diode parameters for solar cells best fit to Equation(1).

Specimen	#1	#2	#3
R_s (Ωcm^2)	7.53	4.60	0.24
R_{sh} (Ωcm^2)	2.76×10^{3}	2.66×10^{3}	5.61×10^{2}
J_{01} (A/cm^2)	2.30×10^{-11}	1.32×10^{-11}	5.21×10^{-13}
J_{02} (A/cm^2)	2.72×10^{-7}	1.94×10^{-7}	3.92×10^{-7}
n	2.0	2.0	2.2
J_L (mA/cm^2)	13.27	13.19	15.20

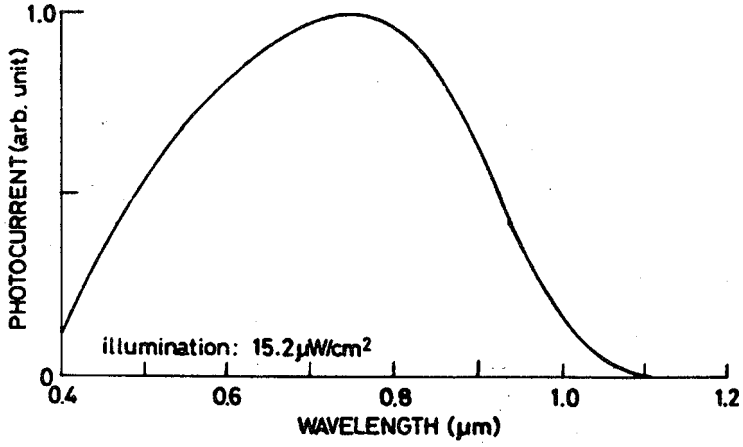

Fig. 5. Spectral response of a thin-film polycrystalline silicon solar cell.

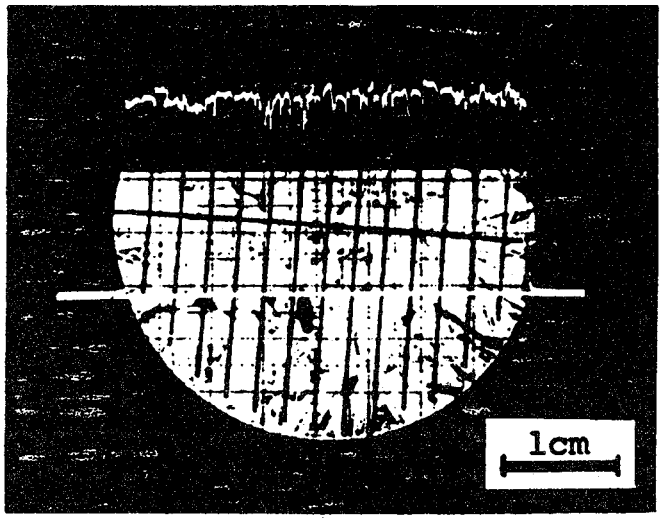

Fig. 6. Photocurrent image obtained by scanning a confined He-Ne laser beam over the lower half of the cell surface corresponding to Fig.3; also shown is a photocurrent line scan.

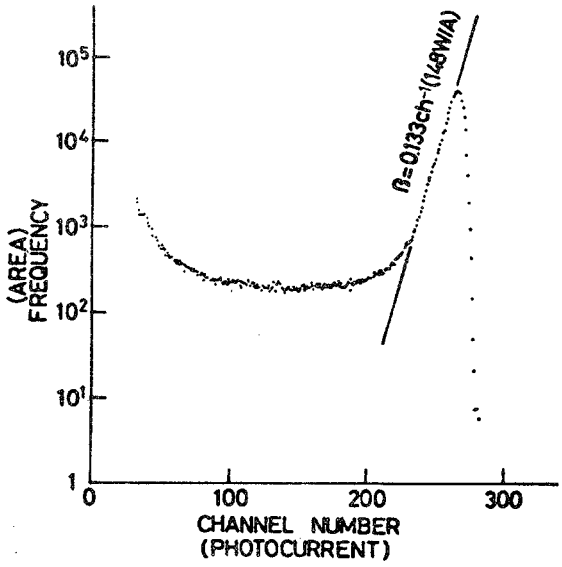

Fig. 7. A photocurrent histogram obtained by scanning a laser spot and sampling the photocurrent corresponding to 40μm mesh points.

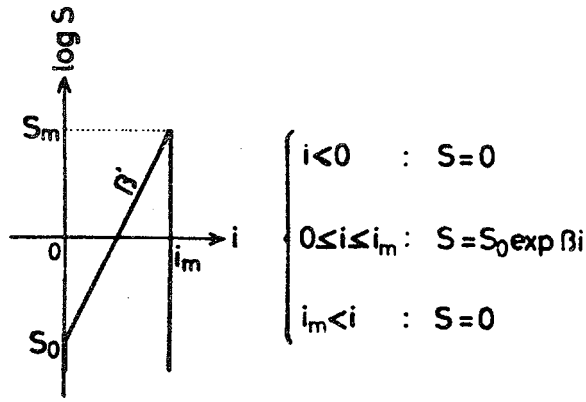

Fig. 8. A simple model for the photocurrent distribution with respect to occupying cell area.

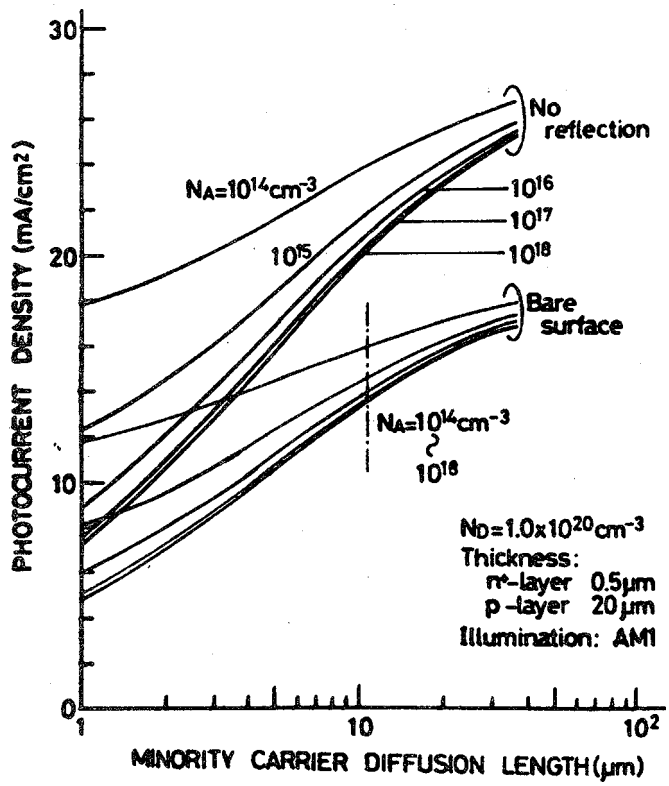

Fig. 9. Photocurrent density of a cell with a 20μm thick active layer and a 0.5μm thick surface layer calculated as a function of the minority carrier diffusion length in the active layer using depletion layer approximation and under AM1 condition.

13a-X-9　多結晶Si薄膜太陽電池(X)　EBIC像の観察

日立中研　蔵迫光紀，斉藤 忠，伊藤晴夫，中村信夫，徳山 巍

序　多結晶Siを用いた太陽電池では粒径の増大により，高純度バルクのセルで変換効率10%[1]，低品位基板上へのエピタキシャル薄膜成長構造では7%以上[2]が示され，単結晶の性能に迫りつつある。結晶粒境界面のキャリア再結合速度は一般に大きく，太陽電池の出力電流を低下させているが，不規則粒界に比べ影響の小さいと言われる線状境界でも結晶構造に起因すると思われる差違がEBIC像で見られる。

実験　試料は，低品位SiをCZ法で引上げた多結晶ロッド(粒径mm級)をスライスし，SiH_2Cl_2 の分解により p層(キャリア濃度 $3\times10^{17}cm^{-3}$)を25μm，n^+層($2.5\times10^{19}cm^{-3}$)を0.54μm 形成した n^+-p-p^+(基板)構造の太陽電池で，変換効率7%以上が得られるものである。分光感度から推定[3]したキャリアの拡散距離は約15μmである。EBIC観察は電子加速電圧25kVで行ない，電流は短絡電流モードで測定した。

結果および考察　右図(A)はセルの表面光学写真で，右上のストライプは電極である。対応するEBIC像を(B)に示し，その矢印間のラインスキャンを(C)に示す。EBIC像の特徴は，①粒界近傍でEBICに指数関数的減衰があり，それは②不規則粒界で一般に大きく，③線状境界の一部で大きい部分もある。また境界に沿ってのEBICの落ち込みは④局在していてランダムではなく，⑤一連の線状境界内ではほぼ一様であり，⑥バルクでの拡散距離，キンクで大きい。また⑦deformation twinや点状欠陥での落ち込みは小さい。これから，EBICの落ち込みは単純な不純物析出によるよりは結晶構造が関与した界面再結合速度の差に依存すると思われる。またEBICのレベルは広い領域でほぼ一定であり，バルクのキャリア拡散距離に依存していて，セルの短絡電流の大きさはこの高さで制限されている。

本研究は通産省工業技術院「サンシャイン計画」の一環として行なわれたものである。

文献　1) M. Fischer et al, IEEE Trans. on Electron Devices, ED-24, 438 (1977).
2) 斉藤 他，第24回応用物理学関係連合講演会 (1977).
3) L.M. Terman, Solid-State Electronics, 2, 1 (1961).

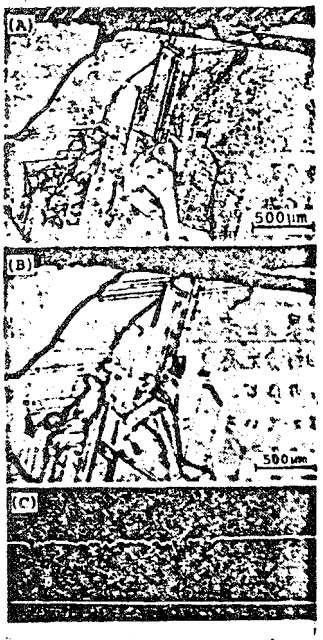

Fig.1 多結晶Si薄膜太陽電池の(A)表面写真，(B) EBIC像，(C)矢印間のEBICラインスキャン

13a-X-10　多結晶Si薄膜太陽電池(XI)　多結晶セルの光電流分布

日立中研　斉藤 忠，蔵迫光紀，伊藤晴夫，中村信夫，徳山 巍

序　多結晶太陽電池は光電流が場所的に不均一であり，微小面積毎の光電流(微分光電流)の面積積分が全出力電流を与える。この微分光電流の分布は多結晶セルのような不均一系を統一的に把握するのに重要な情報であり，試作したセルについてその分光感度のピークに近い波長のHe-Neレーザを用いてこの分布を求めた。

実験　試料は低品位シリコンをCZ法で引上げた多結晶ウェハを基板として，CVD法でp層(キャリア濃度 $3\times10^{17}cm^{-3}$，厚さ25μm)，n^+層($2.5\times10^{19}cm^{-3}$，0.54μm)を形成した太陽電池である。微分光電流の分布は約$20\mu m^{\phi}$のレーザスポットでセル全面を走査し[1]，光電流出力をサンプリングして波高分析して求めた。

結果および考察　セル全面の光電流分布(輝度変調像)をFig.1(A)に示し，矢印間のラインスキャンを(B)に示す。図の規則的な減少は格子状電極部分に相当する。これの光電流ヒストグラムをFig.2に示す。サンプル領域は約20μm×20μmで，サンプル間隔は40μm×40μm，サンプル総数は1.2×10^6点である。ピーク(265ch)は光電流0.23A/Wに相当し，200count近くのflatな部分はセル端および電極での立下り，立上りに対応し，低chの増加はセル外のサンプルに対応する。

単結晶セルではピークを中心とした鋭いガウス様分布となるが，粒径分布が狭い多結晶セルではピークからの指数関数的減少が特徴であり，この減衰定数が不均一性の目やすになる。現状の薄膜Siセルでは減衰定数が大きく(149A/A)，粒界による光電流減少の寄与は小さい。

本研究は通産省工業技術院サンシャイン計画委託研究の一環として行なわれたものである。

1) 蔵迫 他，第23回応用物理学関係連合講演会 予稿 pp.379 (1976).

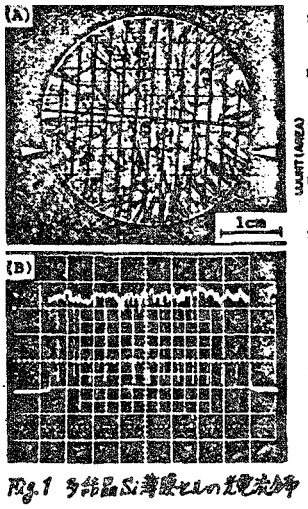

Fig.1 多結晶Si薄膜セルの光電流分布

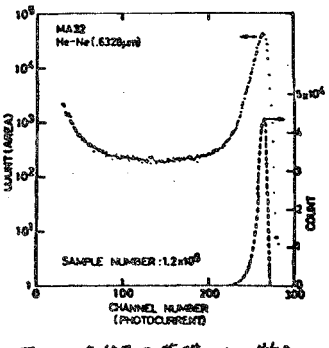

Fig.2 多結晶Si薄膜セルの微分光電流分布(光電流ヒストグラム)

29a—P—4　多結晶Si薄膜太陽電池(XII)　金属Siからの結晶引上げとその評価

日立中研　斉藤 忠，黒田慈慶，松原 直，伊藤晴夫，徳山 巍

1. 序　多結晶の利用が太陽電池低コスト化のアプローチとして注目されている。[1] 我々はすでに精製金属けい素(MG-Si)を基板とする多結晶薄膜方式で変換効率7%以上が得られることを報告した。[2] この報告ではチョクラルスキ法で市販の粗製MG-Siから直接引上げた結晶中の不純物，結晶欠陥および電気的性質について述べる。

2. 実験方法　市販のMG-Si(純度98% up)をソースとし，0.14～1.2mm/minの引上げ速度で約50mmφの結晶を作製した。結晶評価としてスパーク型イオン源質量分析計による不純物分析，Sirtlエッチによる欠陥観察およびHall測定を行なった。

3. 結果と考察　(a)結晶性：MG-Siから引上げた結晶は，図1のSirtlエッチ像に示すような多結晶である。結晶粒径は0.1～数mmで，メルト中の不純物量に主として依存する。典型的な結晶欠陥は結晶粒界の他に，傾角境界のごとき面欠陥と真状欠陥(エッチピット)である。とくにエッチピットは列状を形成しているものが多く，熱歪により生じたと考えられる。引上げ速度が約1.7mm/min以上の場合，結晶中に異質な偏析物が存在した。この偏析物は赤外光を透過せず，結晶に歪を与えることがクロスニコル下の観察で明らかになった。非分散X線エネルギ分析を行なった結果，偏析物はAl-Si合金であり，Cr，Feなどの不純物を含むこともわかった。(b)不純物：表1はCZ前後の分析値で，MG-Si中ではAl，Ni，Fe，TiとCが多量に含まれているが，CZ後ではB，Al，Cu，Feなどが数～数十ppm，その他はppm以下となっている。引上げ速度が小さい場合，不純物量は引上げ速度に依存しない結果を得ている。(c)電気的性質：引上げ結晶の比抵抗は0.08Ω·cm，正孔濃度$1\times10^{19}cm^{-3}$で，粒界と不純物により単結晶より比抵抗が高くなっている。なお，本研究は通産省工技院「サンシャイン計画」の一環として行われた。

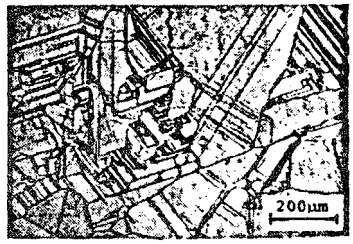

図1. 金属Siから直接引上げた結晶のSirtlエッチ像

表1. 結晶引上げ前後の含有不純物(ppm)

元素	原料Si	CZ引上結晶
B	7	0.9 - 3
Al	3700	2 -60
P	27	0.7 - 7
As	-	0.05
Cu	78	2 - 6
Ni	280	-
Mg	-	0.014- 0.04
Fe	6300	0.6 - 6.0
Cr	171	0.04 - 1.0
Mn	83	0.04 - 0.4
Ti	191	0.1 - 0.4
V	2	0.03 - 0.3
C	1560	8 -30

4. 参考文献
1) H. Fischer et al., IEEE Trans. Electron Devices, ED-24, 438 (1977); L.P. Hunt et al., Conf. Rec. 12th IEEE P.V.S.C. (1976) pp. 125.
2) T. Warabisako et al. Proc. Conf. on Solid-State Devices, (Tokyo) to be published.

29a—P—5　多結晶Si薄膜太陽電池 (XIII)　金属Si基板多結晶Si薄膜太陽電池

日立中研　中村信久，蔵迫光紀，斉藤 忠，松原 直，伊藤晴夫，徳山 巍

1. 序　市販の金属Si (純度98% up) をCZ法で0.1～1mm/minの速度で引上げ，これを基板として上にP/N⁺層の気相成長を行って太陽電池を作成し変換効率5.8%を得た。

2. 実験　CZ法で引上げた結晶はAl，Cu，Fe，Cr等の不純物を1～60ppm含み，結晶粒径0.1～数mmの多結晶で，比抵抗0.08Ω·cmのP型を示した。この結晶をスライシングした後に化学エッチングを行って基板とし，SiH_2Cl_2を用いて1100℃の温度で30～50μmのP層(キャリア濃度10^{16}～$10^{17}cm^{-3}$)，0.5μmのN⁺層(キャリア濃度$5\times10^{18}cm^{-3}$)をそれぞれ気相成長してセルを作成した。

3. 結果　セルの光電変換特性は短絡電流が16～18 mA/cm²，開放電圧が0.49～0.51V，変換効率が5.1～5.8%であり，引上げ速度による差は見られなかった。しかし，高純度多結晶セルや単結晶セルと比較するとまだ低く，特に短絡電流の減少が大きい。これは基板結晶中に含まれるCuやFe等拡散係数の大きい金属が気相成長中に成長層の中に拡散されてしまい，深い準位を形成して少数キャリアのライフタイムを減少させる原因となったり，不純物が種々の結晶欠陥あるいは結晶粒径の小型化の原因となって短絡電流，開放電圧の低下となると考えられる。不純物除去のため前処理としてゲッタリングを行ったが，不純物量がppmオーダであるためその効果はみえない。図1はP型成長層中のライフタイムを測定した結果で，0.1～0.5μsの値を示したが，不規則な結晶粒界を含んでいるため場所によるばらつきがある。図2は基板と成長層の断面をSirtlエッチングしたもので，点状のピットが見られ，層状に高密度に存在する場所やピット列が成長層の境界で止まる現象が観測された。

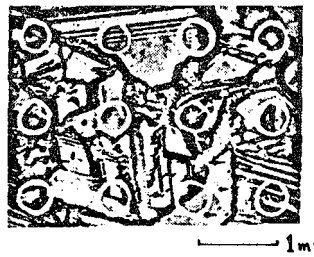

0.17	0.50	0.51	0.28
0.19	0.29	0.34	0.40
0.33	0.27	0.45	0.13

図1. ライフタイムの測定 (μs)

図2. セルの断面のSirtlエッチ像

なお，本研究は通産省工技院「サンシャイン計画」の一環として行われたものである。